

# Stimuli-Responsive Membranes for Membrane Distillation of Oily Waters

Mahdi Shahrooz

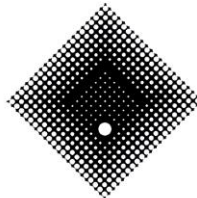
BSc, MSc

Thesis submitted for the fulfilment of the requirements for  
the degree of Doctor of Philosophy (PhD)

Institute for Sustainable Industries and Liveable Cities (ISILC)

Victoria University, Australia

May 2024



**VICTORIA  
UNIVERSITY**

**Abstract:**

Membrane distillation (MD) is a thermally-driven process for water/wastewater treatment which can produce high-quality distillates from highly-saline solutions. However, the presence of different types of oils in the wastewaters can pose serious challenges in their treatment using conventional hydrophobic membranes. These oils are abundant in emulsified or unemulsified forms in the wastewaters encountered in a wide variety of industries including municipal wastewater, food, textile, and oil and gas industries. A key challenge in the treatment oily wastewaters using MD is the tendency of the oil droplets to adhere to the membranes leading to pore blockage (fouling) and liquid intrusion (wetting), thus compromising the membrane performance. Janus membranes are among the many new membranes that have been developed previously, but these membranes face practical limitations due to the weak adhesion between membrane and modification layers. One of the approaches to address this problem is the application of surface grafting methods to form polymer brushes on the membranes but has only been considered in MD to a limited extent. Of the surface grafted brushes, polyelectrolyte brushes offer salinity-responsive anti-oil-fouling membrane properties for practical applications of MD. Grafting of polymer brushes is usually performed using atom-transfer radical polymerization (ATRP) that requires an oxygen-free reaction medium. This further limits the applicability of this method for membranes due to the need for special equipment and tedious de-oxygenation procedure.

Therefore, the main aim of the current thesis is to address the oil adhesion and wetting in MD by preparing a salinity-responsive membrane using polyelectrolyte brushes grafted on the surface of a commercial hydrophobic membrane. Further, a new approach to address the oxygen-free ATRP challenge was proposed using UV-assisted oxygen tolerant ATRP performed under open atmosphere for grafting a negatively charged polyelectrolyte (poly(acrylic acid)) (PAA) onto commercial hydrophobic PVDF membranes (mean pore size =  $0.2 \mu\text{m}$ ). The success of the grafting reaction was confirmed by attenuated total-reflection Fourier transform infrared spectroscopy (ATR-FTIR), scanning electron microscopy (SEM), and energy-dispersive X-ray spectroscopy (EDX) analyses. Surface morphology of the PVDF-PAA membrane was found to be unaffected by the PAA chains and the membrane surface became more hydrophilic as determined by water contact angle. Salinity response of the prepared membranes was evaluated using underwater oil adhesion tests in aqueous solutions with different salinities (from Milli-Q water to 3 M NaCl). It was found that the PVDF-PAA membrane became underwater superoleophobic when NaCl concentration was above 0.01 M inhibiting the oil drop adhesion; while lower salinities allowed surface adhesion of oil. In contrast, the pristine PVDF membrane was wetted by the oil droplet regardless of the salinity of the test medium. New models were proposed in an attempt to explain the surface structure of the PVDF-PAA membrane and its

underwater oleophobicity. Analyses of the proposed models showed that the underwater oleophobicity of the PVDF-PAA membrane can be attributed to the combined effect of the PAA patches on the top of the surface roughness features as well as the air-water interfaces located on the roughness features and pore entrances.

MD testing in “direct contact” (DCMD) mode over 20 hours using a 0.1 % (v/v) dodecane dispersion containing 0.1 M NaCl showed a high oil adhesion resistance (anti-fouling) for the PVDF-PAA membrane indicated by its stable permeate flux ( $\sim 17 \text{ kg}/(\text{m}^2 \cdot \text{h})$ ) and no increase in permeate conductivity. Meanwhile, the unmodified PVDF membrane rapidly lost flux, dropping by 75% within the first five hours of the test. This test gave the first two key conclusions and scientific findings of this study, the first confirming salinity responsive polyelectrolyte brushes are effective at resisting oil adhesion on MD membranes, and the second confirming the effectiveness of the newly proposed scalable oxygen tolerant ATRP as a method to graft these brushes to readily available membrane substrates.

Another part of the study aimed to explore the mechanisms of oil adhesion and resistance by the PAA brushes. The oil adhesion and wetting was also monitored for both PVDF and PVDF-PAA membranes during MD by time-resolved *in-situ* electrochemical impedance spectroscopy (EIS), which has offered great capability for understanding fouling in reverse osmosis, but limited studies so far in MD. This study uniquely adopted a wide frequency sweep between 1 Hz and 500 kHz. Our results showed, in contrast to prior EIS studies in MD, the decrease in the impedance at high frequencies might not be a direct indication of wetting, which was consistently observed for both PVDF and PVDF-PAA membranes. However, only the pristine membrane showed evidence of wetting as indicated by the traditional measurements of permeate electrical conductivity (EC) which underwent a sudden rise after 6 hours. The novel approach and analysis led to the third major scientific contribution of this study, providing a holistic analysis of the EIS results showing the largest changes in the impedance for both membranes occurred at low frequencies, and these changes were more significant for the PVDF membrane that was wetted during the process. Equivalent circuit analysis including the resistance and capacitance elements represented the membrane, and the component values changed during the first 6 hours of the MD process for the PVDF membrane until wetting occurred, but remained almost constant for the PVDF-PAA membrane that did not wet.

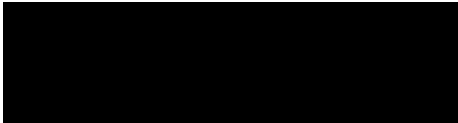
In summary, this thesis found the innovative scalable oxygen tolerant UV-ATRP method is a practical surface modification method for functional membranes. However, further investigation is needed to address its remaining limitations such as controllability and facile initiator grafting to fully realise its potential for growing different types of polymer brushes on various membranes. In addition, the novel models proposed for the surface structure of the PVDF-PAA membranes

proposed in the current study can be employed for a rational design of Janus membranes with advanced functionalities that are resistant to the adhesion of both hydrophilic and hydrophobic compounds. Finally, the results of the *in-situ* EIS analyses in the current study has created a better understanding of MD wetting phenomena, and can be extended to *in-situ* studies of other membrane systems

### **Declaration of Authenticity**

“I, Mahdi Shahrooz, declare that the PhD thesis entitled “Stimuli-Responsive Membranes for Membrane Distillation of Oily Waters” is no more than 80,000 words in length including quotes and exclusive of tables, figures, appendices, bibliography, references and footnotes. This thesis contains no material that has been submitted previously, in whole or in part, for the award of any other academic degree or diploma. Except where otherwise indicated, this thesis is my own work”.

“I have conducted my research in alignment with the Australian Code for the Responsible Conduct of Research and Victoria University’s Higher Degree by Research Policy and Procedures.”



01/05/2024

*Dedicated to my family and friends*

## **Acknowledgements:**

My journey through my PhD studies has been quite challenging, largely due to the extended COVID lockdowns in Melbourne, which significantly restricted access to our laboratories. Coping with the resulting stress and its impact on my mental health made this journey far more arduous and less enjoyable than anticipated. However, I'm grateful for the invaluable support and guidance provided by the VU counsellors, Jennifer Halat, Freda Dimitrakakis, Julie Burn, and John Coburn. Their compassionate assistance helped me navigate through the stress and regain control over my life.

I extend my heartfelt appreciation to my parents, Rasoul and Sousan, and my siblings, Faezeh, Ali, and Meysam, for their unwavering support throughout my studies. Their encouragement has been a constant source of motivation, helping me overcome the challenges encountered during my PhD journey. I am also deeply indebted to my dear friends, Maedeh Nadimi and Mona Ghorbani, whose support has been invaluable. Maedeh's presence during critical moments, both as a colleague and friend, has been invaluable, while Mona's consistent support and check-ins despite her busy schedule are truly appreciated.

I am grateful to my colleagues and friends for their wisdom and guidance in navigating the challenges of doctoral research. Special thanks to Narges Dargahi, whose insightful advice and discussions on improving academic communication have been immensely helpful. I also appreciate Jianhua Zhang and Johnson Lou for sharing their valuable insights and opinions, which significantly contributed to my project. A heartfelt acknowledgment goes to my dear friend, Milad Laghaei, whose support was indispensable in various aspects of my PhD journey, from initial program search to settling in Australia and navigating through the program.

I am also thankful to my mentor, friend, and former supervisor, Dr. Morteza Sadeghi, whose support and wisdom have been constant companions throughout my journey. Engaging discussions with friends like Derrick D'Souza, Tohid Hajizadeh, Ramtin Etemadi, Malavika Arun, Travis Denmead, Paria Moarref, Sarah Khodaverdi, Davor Daniloski, Elaheh Ahmadi, Geetha Vemula, Laryssa Pereira, Marta Vasconcelos, Sarani Kannangara, Lavern Nyamutswa, and Charleston Bezerra have been a source of inspiration and encouragement.

I extend my gratitude to Stacey Lloyd for her kindness in providing facilities, equipment, technical assistance, and support throughout my PhD. Stacey always went above and beyond to assist with any lab-related issues. I also appreciate the support from Nishantha Illangantilaka and Larruceo (Larry) Bautista, who provided training on various instruments and assisted with technical issues. Thanks also to Noel Dow, Lee Nuang Sim, Marlene Cran, and Mary Marshall for their assistance at different project stages. Additionally, I would like to express my sincere thanks to Professor Stephen Gray for his kind support throughout my PhD, particularly for his

understanding of the challenges I faced during the COVID-19 lockdowns, and for his assistance in various stages of my research.

Finally, I express my deepest gratitude to my supervisors, Professor Mikel Duke, Professor Xing Yang, and Professor Rong Wang, for their unwavering support and guidance. Their mentorship enabled me to explore a broad spectrum of research areas and expand my knowledge. Their prompt responses, even on weekends, and commitment to meeting deadlines have been invaluable. Mikel's guidance has played a pivotal role in my growth as a researcher, fostering better critical thinking skills. Xing's early support helped me establish my research direction, and her continued guidance, even after relocating to KU Leuven, has been instrumental in refining my work. Rong's support has been invaluable from the proposal stage to manuscript proofreading. Her insights have consistently enhanced my work, contributing to its refinement and success.



# Contents

Chapter 1	Introduction .....	1
1.1	Membrane distillation and its application to treatment of oily solutions in industry ....	1
1.2	Membrane materials for resisting performance limiting oil contamination .....	1
1.3	Janus membrane materials and grafting for improved stability and stimuli-responsive properties .....	2
1.4	Responsive polyelectrolytes .....	2
1.5	Grafting by atom-transfer radical polymerization (ATRP) and its scalability challenges.....	3
1.6	Understanding beneficial material improvements <i>in-situ</i> via electrochemical impedance spectroscopy .....	4
1.7	Research Objectives .....	4
1.8	Thesis Layout: .....	5
Chapter 2	Literature Review .....	7
2.1	Introduction .....	7
2.2	Interfaces involved in colloidal adhesion .....	8
2.3	Surface interactions between a smooth nonporous flat surface with homogeneous chemical composition and a spherical colloidal particle (Case 1): .....	11
2.3.1	Theory of surface interactions .....	11
2.3.2	Effect of <i>IS</i> and ion valance .....	14
2.3.3	Non-DLVO interactions .....	15
2.3.4	Effect of hydrodynamics .....	16
2.4	Effect of surface roughness on the interactions between MD membranes and foulants (Case 2).....	16
2.4.1	Cases where the size of the particles is larger than that of the asperities .....	17
2.4.2	Cases where the size of the particles is smaller than that of the asperities.....	20
2.4.3	Surfaces with random or hierarchical roughness features .....	23
2.4.4	Interactions leading to colloidal deposition on rough surfaces .....	23
2.4.5	Particle detachment from rough surfaces .....	27
2.4.6	Summary of particles interacting with rough surfaces .....	28
2.5	Surface interactions between a chemically heterogeneous smooth flat surface and spherical colloidal particles (Case 3) .....	29
2.5.1	Chemical heterogeneities on MD membrane surfaces .....	29
2.5.2	Definition and theory of heterogeneous surfaces .....	30
2.5.3	Importance of ZOI in understanding heterogeneous surface interactions .....	31
2.5.4	Hydrodynamic considerations in particle deposition on chemically heterogeneous surfaces	33

2.5.5	Effect of frictional forces on attachment and detachment of particles on surfaces	37
2.5.6	Summary of surface interactions on chemically heterogeneous surfaces and relevance to MD membranes.....	38
2.6	Combined effect of topography and chemistry on the surface interactions between MD membranes and colloidal particles (Case 4).....	39
2.7	Manifestation of surface interactions in MD membranes and rational design of adhesion-resistant membranes .....	40
2.7.1	Asperities in MD membranes.....	40
2.7.2	Chemical patches in MD membranes.....	41
2.7.3	Importance of underwater oil wetting resistance of MD membranes .....	42
2.7.4	Polyelectrolytes and their stimuli-responsive behaviour in the design of oil resistant MD membranes.....	43
2.7.5	Grafting of polyelectrolytes using atom-transfer radical polymerization (ATRP)	43
2.8	Application of electrochemical impedance spectroscopy (EIS) for <i>in-situ</i> fouling and wetting detection in MD .....	44
2.8.1	Single-frequency <i>in-situ</i> EIS measurements in wetting detection in MD .....	44
2.8.2	Wide-frequency sweep <i>in-situ</i> EIS measurements in wetting detection in MD..	45
2.5.	Conclusions and future directions: .....	46
Chapter 3	Materials and Methods .....	48
3.1	Materials.....	48
3.2	Characterizations.....	48
3.2.1	Attenuated total reflectance Fourier transform infrared spectroscopy (ATR-FTIR)	48
3.2.2	Contact-angle experiments.....	48
3.2.3	Scanning electron microscopy (SEM) and energy dispersive X-ray (EDX) spectroscopy .....	48
3.2.4	Streaming potential analysis.....	49
3.3	Method Development for Surface Modifications.....	49
3.4	<b>Approach 1:</b> Grafting of PAA on the entire membrane .....	49
3.4.1	Alkaline treatment (OH-grafting).....	50
3.4.2	APTES-grafting.....	50
3.4.3	Initiator-grafting .....	50
3.4.4	Oxygen tolerant UV-assisted ATRP for PAA grafting using <b>Approach 1</b> .....	51
3.5	<b>Approach 2:</b> Grafting of PAA on top of the roughness features of the MD membranes	51
3.5.1	Alkaline treatment .....	52
3.5.2	APTES grafting .....	52
3.5.3	Initiator grafting .....	52

3.5.4	Oxygen tolerant UV-assisted ATRP for PAA grafting employing <b>Approach 2</b>	52
3.6	Membrane distillation experiments	53
3.7	Preparation of the saline oil dispersions	54
3.8	EIS experiments	54
Chapter 4	Proof of concept for oxygen-tolerant UV-assisted atom-transfer radical polymerization (ATRP) of Poly(acrylic acid) (PAA) onto PVDF Membranes	56
4.1	Introduction	56
4.2	Validation of the initiator grafting reactions	56
4.2.1	ATR-FTIR Results on the treated and untreated membranes	56
4.2.2	Water contact-angle measurements	57
4.3	Discussions and conclusions on <b>Approach 1</b>	58
Chapter 5	Salinity-responsive poly(acrylic-acid)-grafted PVDF membranes by oxygen tolerant atom-transfer radical polymerization (ATRP) for oil-resistant membrane distillation	60
5.1	Introduction	60
5.2	Surface chemistry and morphology of the PVDF-PAA membranes	60
5.3	Salinity-responsive behaviour and underwater oleophobicity of the PVDF-PAA membranes	65
5.4	Effect of membrane surface modifications on oil fouling resistance of the MD membranes	68
5.5	Conclusions	71
Chapter 6	Proposed models for the surface chemistry of the as-prepared PVDF-PAA membrane and their wetting properties	72
6.1	Introduction	72
6.2	Models for the surface chemistry of PVDF-PAA membrane	72
6.3	In-air-water contact angle of the proposed models:	74
6.4	Underwater oil contact angle of the proposed model surfaces	76
6.5	Conclusions	82
Chapter 7	Analysing the wetting behaviour in membrane distillation of oily waters in real-time by <i>in-situ</i> electrochemical impedance spectroscopy (EIS)	84
7.1	Introduction	84
7.2	Visual observation of the real-time <i>in-situ</i> EIS measurements	84
7.3	Analysis of static EIS measurements and development of equivalent circuits	91
7.4	Changes in the physical properties of the system during MD measured by real-time EIS.	94
7.5	Conclusions	97
Chapter 8	Conclusions and future directions	100
8.1	Summary of the current research	100
8.2	Future directions:	102
Appendices		106

Appendix A: Sample derivation of underwater oleophobicity of the models proposed in Chapter 6.....	106
Appendix B: Supplementary information on real-time in-situ EIS studies of oil wetting in MD (Chapter 7).....	107
B1: Dynamic EIS results on the three studied systems (PVDF-salt, PVDF-salt-oil, and PVDF-PAA-salt-oil).....	107
B2: Details on the fitting procedures for the development of the equivalent circuits employed in the in-situ EIS analyses .....	108
References .....	112

## List of Figures

<b>Figure 2.1:</b> Schematic illustration of the interfaces involved in surface interactions between different types of MD membranes and colloidal particles. The hydrophobic and superhydrophobic surfaces have roughness features with converging, straight, or randomly rough cavities, while the roughness features of the omniphobic membranes usually have re-entrant (converging-diverging) cavities. The Janus membranes can have either of the hydrophobic, superhydrophobic, or omniphobic surfaces as its substrate. The shown schematics are only examples of these membranes for illustrating the positions of the solid-water and air-water interfaces. ....	10
<b>Figure 2.2:</b> DLVO interaction energy between a flat plate and a spherical particle, (with permission from [83]). ....	14
<b>Figure 2.3:</b> a) Schematic of the model used to calculate the interaction energy between a spherical particle and a rough plate, b) Changes of the energy barrier height of the shown model system with asperity radius for a particle with $D = 5 \mu m$ under unfavorable attachment conditions. The dotted and the solid lines in the graph represent the energy barrier of the rough and smooth surface (in the absence of the asperity), respectively (with permission from [123]). ....	18
<b>Figure 2.4:</b> Changes in the critical asperity size as a function of the particle radius and Debye length ( $\kappa - 1$ ): circles for $\kappa - 1 = 3 \text{ nm}$ , plus marks for $\kappa - 1 = 5 \text{ nm}$ , diamonds for $\kappa - 1 = 10 \text{ nm}$ , squares for $\kappa - 1 = 20 \text{ nm}$ , triangles for $\kappa - 1 = 35 \text{ nm}$ , (with permission from [123]). ....	19
<b>Figure 2.5:</b> An example of the energy maps plotted by Shen et al. [129]. The regions of the primary and secondary energy minima as well as the energy barrier can be observed in the magnified view of the map (with permission from [129]). ....	21
<b>Figure 2.6:</b> Map of the interaction energy for a particle of radius=50 nm approaching a simulated rough surface with separation distances of a) 50 nm, b) 25 nm, c)10 nm, and d) 5 nm. In the above energy maps, x and y axes are in nm, and the colour bar on the right side of each map is in the units of $kBT$ (figure with permission from [125]). ....	22
<b>Figure 2.7:</b> DLVO interaction force map normalized by the hydrodynamic drag force a), and (b) interaction energy (colour bars are in the units of $kBT$ ) for a colloidal particle with a diameter of the 66 nm interacting with an asperity with the radius of 100 nm at different ionic strengths (1: 0.2 M; 2: 0.1 M; 3: 0.01 M; 4: 0.001 M). The axes are normalized by particle diameter (with permission from [129]). ....	25
<b>Figure 2.8:</b> Dependence of particle (diameter= $0.55 \mu m$ ) deposition rate (number of particles/min. mm <sup>2</sup> ) on the roughness height under unfavourable attachment conditions in the loading rate of $3.33 \times 10^{-4} \text{ m/s}$ . A critical asperity size can be observed at the roughness height $\cong 50 \text{ nm}$ (with permission from [133]). ....	25
<b>Figure 2.9:</b> Top view of the particle deposition results on a surface roughened with spherical asperities in a) in-line and b) staggered configurations under favourable attachment conditions. The particle Peclet number is 1.4. The arrows show the direction of the flow (with permission from [134]). ....	26
<b>Figure 2.10:</b> Variation of detachment energy barrier ( $\Delta\Phi$ ) for particles of diameter=30 nm (top) and 1156 nm (bottom) with asperity radius and ionic strength: asterisk= 0.001 M, square=0.01 M, sphere=0.1 M, triangle=0.2 M. The detachment energy barriers for particle-smooth plate are shown at different ionic strengths as bolder solid line for 0.001 M, bold solid line for 0.01 M, solid line for 0.1 M and dashed line for 0.2 M. (with permission from [136]). ....	28
<b>Figure 2.11:</b> Different definitions of zone of influence (ZOI) and its radius, $R_{zi}$ . A sphere with the radius of $R_p$ is in contact with a patchy planar surface. $\kappa - 1$ is Debye length of the	

<p>solution. In the definition shown on the left, <math>R_{zi}</math> can be calculated using Pythagoras' theorem <math>R_{zi}^2 + R_p^2 = (R_p + \kappa - 1)^2</math>. Alternatively, in the definition shown in on the right, the <math>R_{zi}</math> is the radius of the zone resulting from the intersection of the plane at the distance of one Debye length from the surface, and the volume of the "particle+particle Debye length". Similar to the other definition, <math>R_{zi}</math> can be calculated for this definition using: <math>R_{zi}^2 + (R_p - \kappa - 1)^2 = (R_p + \kappa - 1)^2</math> (with permission from [138]).</p>	31
<b>Figure 2.12:</b> Trajectory of $1 \mu\text{m}$ particles over a chemically heterogeneous flat surface with different patch densities ( $\Theta$ ) (with permission from [124]).	34
<b>Figure 2.13:</b> Schematic presentation of hydrodynamic bump effect (with permission from [140]).	36
<b>Figure 2.14:</b> Deposition flux of negatively charged particles with a radius of $1 \mu\text{m}$ on positively charged stripes with a width of $20 \mu\text{m}$ (with permission from [141]).	37
<b>Figure 2.15:</b> Adhesion phase diagrams by Duffadar and Davis as a function of patch density, $\Theta$ , and Debye length ( $\kappa - 1$ ) (in $\text{nm}$ ) for negatively charged particles with a radius of $1 \mu\text{m}$ over a chemically heterogeneous surface at: a) shear rate of $25/\text{s}$ , and b) shear rate of $50/\text{s}$ (with permission from [144]).	38
<b>Figure 3.1:</b> Proposed reaction steps for grafting of the poly(acrylic acid) (PAA) sodium salt on the surface of the PVDF membrane. The selected initiators were BMPA and BiBB for <b>Approaches 1</b> and <b>2</b> , respectively.	50
<b>Figure 3.2:</b> The schematic illustration of Different methods of performing the ATRP reactions by a) submerging the membrane in the polymerization solution, b) sandwiching the membrane and the polymerization solution between the petri dish and a glass slide.	51
<b>Figure 3.3:</b> The schematic illustration of the reaction setup for performing the UV-ATRP reactions by submerging the membrane in the polymerization solution in <b>Approach 2</b> .	53
<b>Figure 3.4:</b> Schematic of the setup used to conduct MD experiments in this work. T indicates the location of the thermocouples for temperature measurement.	54
<b>Figure 3.5:</b> Exploded view of the MD cell employed in the current research, showing location of the electrodes, the flow channels, and the membrane.	55
<b>Figure 4.1:</b> ATR-FTIR results on the pristine and surface-modified PVDF membranes using <b>Approach 1</b> : a) full view of the ATR-FTIR spectra, b) magnified view of the spectra ( $1500\text{-}2000 \text{ cm}^{-1}$ ) for observing the carbonyl peaks of the surface-grafted PAA.	56
<b>Figure 4.2:</b> ATR-FTIR results on the pristine, PVDF-PAA, and PVDF-PAA-TEA membranes prepared using <b>Approach 1</b> : a) full view of the ATR-FTIR spectra, b) magnified view of the spectra ( $1500\text{-}2000 \text{ cm}^{-1}$ ) for observing the carbonyl peaks of the surface-grafted PAA.	57
<b>Figure 4.3:</b> Water contact-angle results on the surface of the pristine as well as the treated membranes. The water droplets wetted the PVDF-OH membranes upon contact.	58
<b>Figure 5.1:</b> ATR-FTIR spectra of PVDF and PVDF-PAA membranes.	61
<b>Figure 5.2:</b> SEM images of PVDF (a) and PVDF-PAA (b) membranes. Spots selected for the EDX analysis of PVDF (c), and PVDF-PAA (d) membranes. Region images for the EDX analysis on the PVDF (e) and PVDF-PAA (f) membranes. e) Atomic concentration ratio of O/C and O/F in PVDF and PVDF-PAA obtained from the EDX analysis. The scale bars correspond to $8 \mu\text{m}$ (in a and b), $3 \mu\text{m}$ (in c and d), and $15 \mu\text{m}$ (in e and f).	63
<b>Figure 5.3:</b> Surface zeta potential of PVDF and PVDF-PAA membranes as a function of pH using a $0.1 \text{ M NaCl}$ solution at room temperature. The error bars represent the standard deviation of four measurements and are smaller than the data points for $\text{pH} > 3$ .	64
Figure 5.4: Water contact angle of PVDF and PVDF-PAA membranes	65
<b>Figure 5.5:</b> Results of underwater oil adhesion tests on PVDF and PVDF-PAA membranes.	67
<b>Figure 5.6.</b> MD permeation flux and EC for a) PVDF and b) PVDF-PAA. Feed and permeate inlet temperatures were constant at $60^\circ\text{C}$ and $20^\circ\text{C}$ , and the crossflow velocity of both feed and permeate was $3.13 \text{ m/min}$ . The oily dispersion contained $0.1 \%$ (v/v) dodecane and $0.1 \text{ M NaCl}$ in water.	69

<b>Figure 6.1:</b> Schematic illustrations of a) <b>Model 1</b> , where only the top surface of the membrane is partially grafted with PAA molecules; and b) <b>Model 2</b> , where the top surface of the membrane is fully grafted by PAA molecules and the internal surface of the pores is grafted by PAA down to a certain depth (below the membrane surface facing the feed) . For both schematics, the green circles on top of the outer surface represent the nodular roughness feature of the membrane. Close-up images on bottom have ~nm dimension scale. ....	73
<b>Figure 6.2:</b> In-air water contact angle of the surfaces of PVDF-PAA membranes according to a) <b>Model 1</b> , and b) <b>Model 2</b> . The PAA-grafted region is shown as a smooth layer for simplicity (in violet colour) .....	76
<b>Figure 6.3:</b> The schematic presentation of the underwater oil contact angle of PVDF-PAA membrane and the wettability phase diagrams/plots of $\cos\theta_{o, total}$ as a function of $f_{top}$ and $f_{PAA}$ according to <b>Model 1-Scenarios 1</b> (a and b), <b>2</b> (c and d), and <b>3</b> (e and f). The region coloured in red shows the combinations of $f_{top}$ and $f_{PAA}$ with $\theta_{o, total} > 90^\circ$ , while the blue region show the combinations leading to $\theta_{o, total} \leq 90^\circ$ .....	79
<b>Figure 6.4:</b> The schematic presentation of the underwater oil contact angle of PVDF-PAA membrane and the wettability phase diagrams/plots of $\cos\theta_{o, total}$ as a function of $f_{top}$ and $f_{PAA}$ according to <b>Model 1-Scenarios 4</b> (a and b), <b>5</b> (c and d), and <b>6</b> (e and f). The region coloured in red shows the combinations of $f_{top}$ and $f_{PAA}$ with $\theta_{o, total} > 90^\circ$ , while the blue region show the combinations leading to $\theta_{o, total} \leq 90^\circ$ .....	80
<b>Figure 6.5:</b> The schematic presentation of the underwater oil contact angle of PVDF-PAA membrane according to <b>Model 2</b> (a). The plot of $\cos\theta_{o, total}$ as a function of $f_{top}$ for <b>Model 2</b> as presented in Table 6.1 (b). The surface becomes underwater oleophobic with $\theta_{o, total} \geq 90^\circ$ at $f_{top} \geq 0.5$ .....	81
<b>Figure 7.1.</b> MD results and corresponding real-time Bode plots (impedance modulus ( $ Z $ ) vs. different frequencies) at different times for the three tested systems: PVDF-salt: a) and d); PVDF-salt-oil b) and e); PVDF-PAA-salt-oil c) and f). Feed and permeate inlet temperatures were constant at 60°C and 20°C, and the crossflow velocity of both feed and permeate was 3.13 m/min. The oily dispersion contained 0.1 % (v/v) dodecane and 0.1 M NaCl in water. The saline solution contained 0.1 M NaCl in water. ....	86
<b>Figure 7.2:</b> The impedance modulus ( $ Z $ ) (top row) and the normalized impedance modulus ( $ Z / Z_1 $ ) (where $ Z_1 $ is the value of impedance at $t=0$ h (bottom row)) at different frequencies vs. time for PVDF-salt: a) and d); PVDF-salt-oil: b) and e); PVDF-PAA-salt-oil: c) and f). Feed and permeate inlet temperatures were constant at 60°C and 20°C, and the crossflow velocity of both feed and permeate was 3.13 m/min. The oily dispersion contained 0.1 % (v/v) dodecane and 0.1 M NaCl in water. The saline solution contained 0.1 M NaCl in water. ....	88
<b>Figure 7.3:</b> The positive section of the Nyquist plots at different times for PVDF-salt: a) and d); PVDF-salt-oil: b) and e); PVDF-PAA-salt-oil: and c) and e). Top row shows the plots up to $Z' = -Z'' = 106 \Omega$ , and the bottom row shows the magnified view of the plots up to $Z' = -Z'' = 105 \Omega$ . Feed and permeate inlet temperatures were constant at 60°C and 20°C, and the crossflow velocity of both feed and permeate was 3.13 m/min. The oily dispersion contained 0.1 % (v/v) dodecane and 0.1 M NaCl in water. The saline solution contained 0.1 M NaCl in water. ....	90
<b>Figure 7.4:</b> Cross comparison of the Bode (a), and Nyquist (b) plots of the studied systems over the entire course of MD (20 h) .....	91
<b>Figure 7.5:</b> Schematic presentation of the physical elements involved in the measured electrical properties of the system for EIS equivalent circuit analysis. ....	92
<b>Figure 7.6:</b> The equivalent circuit a), and curve fitting results b), on the PVDF-salt-oil system at $t=10$ h after wetting occurred. ....	95
<b>Figure 7.7:</b> Membrane resistance (a, and capacitance b); and permeate resistance (c, and capacitance d), obtained from model fitting on PVDF-salt-oil and PVDF-PAA-salt-oil systems.	

List of figures

The permeate resistance for the PVDF-salt-oil system is shown in dotted lines for  $t > 7$  h to highlight the fact that this value is obtained for the modified equivalent circuit and may include contributions from both permeate and feed solutions. The corresponding permeate capacitance was not present in the modified circuit model and the data are absent for this parameter after  $t=7$  h..... 96

**Figure B 1.** Full view of the normalized impedance modulus ( $|Z|/|Z_1|$ ) (where  $|Z_1|$  is the value of impedance at  $t=0$  h (bottom row)) at different frequencies vs. time for PVDF-salt: a) and d); PVDF-salt-oil: b) and e); PVDF-PAA-salt-oil: c) and f). Feed and permeate inlet temperatures were constant at 60°C and 20°C, and the crossflow velocity of both feed and permeate was 3.13 m/min. The oily dispersion contained 0.1 % (v/v) dodecane and 0.1 M NaCl in water. The saline solution contained 0.1 M NaCl in water. .... 107

**Figure B 2:** Full view of the Nyquist plots at different times for PVDF-salt: a) and d); PVDF-salt-oil: b) and e); PVDF-PAA-salt-oil: and c) and e). Feed and permeate inlet temperatures were constant at 60°C and 20°C, and the crossflow velocity of both feed and permeate was 3.13 m/min. The oily dispersion contained 0.1 % (v/v) dodecane and 0.1 M NaCl in water. The saline solution contained 0.1 M NaCl in water. .... 107

**Figure B 3:** The equivalent circuit and curve fitting results on the cell properties. In the Nyquist plots, the blue circles represent the raw data and the red triangles represent the fitted curve... 108

**Figure B 4:** The equivalent circuit and curve fitting results on the feed compartment properties. In the Nyquist plots, the blue circles represent the raw data and the red triangles represent the fitted curve. .... 109

**Figure B 5:** The equivalent circuit and curve fitting results on the permeate compartment properties. In the Nyquist plots, the blue circles represent the raw data and the red triangles represent the fitted curve. .... 110

**Figure B 6:** The equivalent circuit and curve fitting results on the entire system including the membrane for the wetted scenario. In the Nyquist plots, the blue circles represent the raw data and the red triangles represent the fitted curve..... 111



---

## List of Tables

<b>Table 6-1:</b> The underwater oil contact angle of the membranes according to the proposed models under different scenarios. The phases on the top surface and in the pores refer to the interfaces of the mentioned phases with oil. ....	77
<b>Table 7-1:</b> Summary of the modelled circuit components for each model element based on static testing including the proposed combined circuit. The static tests were performed at room temperature without MD. ....	93

# Chapter 1 Introduction

---

## 1.1 Membrane distillation and its application to treatment of oily solutions in industry

Membrane distillation (MD) is a well-known separation method under development, which can be utilized for treatment of the feed solutions with a high-concentration of non-volatile solutes, due its lower sensitivity to osmotic pressure, compared to other methods such as reverse osmosis (RO), and nanofiltration (NF) [1]. It is a thermally-driven process which utilizes the vapour-pressure difference, typically between the hot feed solution and the cold permeate, as a driving force for the transport of different volatile species (usually water) across a porous membrane that is commonly hydrophobic to prevent liquid water entering the membrane [2].

Oils are among the abundant low-surface-energy compounds which can exist in emulsified or dispersed forms in a wide variety of wastewaters produced by different industries including food [3] and chemical processing [4] and oil industries [3-7]. Most of the MD studies on oily wastewaters involve the use of emulsified oily solutions which usually contain oil ‘particles’ covered with emulsifiers [8], while there has been an increasing interest in dispersed (un-emulsified) oily solutions due their abundance in the industries mentioned above [6, 9-23]. Herein, the solutions containing dispersed oils are referred to as oily waters and differ from emulsified oils as the ‘particles’ in solution have hydrophobic surfaces. Treatment of oily waters using MD poses many challenges regarding the adhesion of oil droplets onto the membrane surfaces, blockage of pores, and membrane wetting (liquid intrusion). Therefore, their treatment using MD requires membranes with special wetting resistance against both low (i.e., oils)- and high (i.e., saline solutions)-surface-tension liquids. Additionally, these membranes should resist against the adhesion of oil droplets (fouling). This complexity makes the membrane development for oily-water treatment a conceptual and practical challenge.

## 1.2 Membrane materials for resisting performance limiting oil contamination

Omniphobic [24] and hydrophilic-hydrophobic Janus [25, 26] membranes are among the most recent developments in wetting- and fouling-resistant MD membranes. Omniphobic membranes are generally characterized by their re-entrant (diverging surface roughness cavities) surface geometry and low surface-energy [27]. These membranes were found to resist against wetting and fouling by many hydrophilic and hydrophobic compounds in solution [1, 27] including emulsified oils, surfactants, and humic acid. However, they suffer from oil contamination in treatment of oily waters (dispersed oils) [1, 27]. Hydrophilic-hydrophobic Janus membranes consist of a hydrophilic top layer coated on a hydrophobic substrate with the former facing the feed solution [25, 26]. These membranes have demonstrated satisfactory oil adhesion resistance in the treatment of synthetic unemulsified oily wastewaters [6, 14, 27]. These results highlight the

possible contribution of surface interactions in the adhesion of oil droplets onto the membranes in MD. However, these effects have only been considered to a limited extent in MD of solutions other than oily waters [28-31], leaving a large gap in our knowledge of these systems.

### 1.3 Janus membrane materials and grafting for improved stability and stimuli-responsive properties

Despite the favourable resistance of Janus membranes against dispersed oils, these membranes suffer from the low stability of the hydrophilic top layer due to its poor integration with the hydrophobic substrate due to hydrophobic or electrostatic interactions employed by other methods for the coating process [25, 26]. This problem would be addressed if the hydrophilic molecules (or polymers) are covalently grafted to the hydrophobic substrate [32]. The surface-tethered hydrophilic polymers have a more stable bond to the hydrophobic substrate. However, surface grafting methods have only been used in a limited extent for fabricating Janus MD membranes [32].

Different types of hydrophilic polymers can be grafted to the membrane surfaces ranging from charged polyelectrolytes to neutral polar polymers [33, 34]. Among these polymers, stimuli-responsive polymers have the advantage of on-demand fouling removal, which would be beneficial for removing the adhered compounds that tend to accumulate on hydrophilic surfaces. Depending on their chemical structure, physical properties of stimuli-responsive polymers can change in response to the changes in their environmental conditions such as pH [35-39], ionic strength [40, 41], temperature [35, 41-45], and others as reported in the literature [46]. The change in polymer properties usually results from a change in the chain conformation, which can be triggered or controlled by varying the environmental parameters. However, the term “stimuli-responsive polymers” is specifically used in the circumstances that the change in the properties of the polymers are exploited for a particular purpose such as switching or tuning of the surface wettability, polymer solubility, membrane pore-size, etc. [47, 48]. In membranes, these polymer properties have been utilized for on-demand cleaning and fouling detachment [35, 37-42, 44, 49-51], switchable oil-water separations [46, 52-54], and gating functionality [55]. On-demand fouling detachment functionality has been achieved in reverse osmosis (RO) [40, 41, 44], ultrafiltration (UF) [35, 37-39, 42, 49], and microfiltration (MF) [50, 51] membranes by incorporating stimuli-responsive polymers on the surface of these membranes. MD membranes with stimuli-responsive functionality have also attracted increasing interest in the recent years [56-62].

### 1.4 Responsive polyelectrolytes

Among different types of stimuli-responsive polymers, pH/salinity-responsive polyelectrolytes are of great practical interest due to their dual responsive behaviour toward pH and salinity, as

well as their facile operation in a large scale membrane process compared to other stimuli-responsive polymers [63]. These polymers are consisted of a hydrophobic backbone with acidic or basic side groups, which, depending on the solution pH, can partially or totally dissociate in water [63]. For instance, an acidic polyelectrolyte such as poly(acrylic acid) (PAA) becomes more deprotonated and therefore more hydrophilic at the pH values higher than its  $pK_a$  ( $\approx 4.7$ ) [46, 63]. In addition, an increase in the ionic strength of the solution leads to a decrease in the hydrophilicity of the surface-grafted pH-/ion-responsive polymers due to charge screening effects of the salt ions [46, 64, 65]. The adhesion resistance of surface-grafted pH-/ion-responsive polymers against oil droplets is hypothesized to be governed by the competition between different attractive forces such as the hydrophobic interactions between the polymer backbone and oil droplets, and repulsive forces such as hydration forces due to the hydration layer formed around the ionized polymer side-groups [18]. Additionally, electrostatic interactions can act as repulsive or attractive forces depending on whether or not the charge of the polyelectrolyte is the same as the surface charge of the oil droplets (negative) [18].

### 1.5 Grafting by atom-transfer radical polymerization (ATRP) and its scalability challenges

A major challenge in the grafting of stimuli-responsive polymers on membranes is imposed by the inherent limitations of these reactions. For instance, one of the widely-used lab-scale methods for the surface grafting of polymers is atom-transfer radical polymerization (ATRP) that allows for a high grafting density and is used for growing polymer brushes on various surfaces [33, 34]. However, similar to most other radical polymerization methods, ATRP is sensitive to the presence of oxygen in the reaction medium that can react with the catalyst and deactivate it. Therefore, most of the surface grafting reactions employing ATRP are either performed under an oxygen-free cabinet, or inside specially designed reaction vessels that allow for the medium to be deoxygenated prior to the reaction [33, 34]. This limits the size and increases the production costs of the of the surfaces grafted using this method, which would be problematic in the context of a membrane that is aimed to be used in industry. Research in ATRP chemistry has led to development of various methods to tackle the problem of oxygen sensitivity [66-68]. These methods aim at consuming the oxygen that exists in the reaction medium or at actively regenerating the catalyst during the reaction [66-68]. UV-assisted oxygen-tolerant ATRP is one of these methods that can be performed under open atmosphere [66], and carries the potential of industrial feasibility for large surfaces such as membranes. However, this method has not been employed on any membranes so far.

### 1.6 Understanding beneficial material improvements *in-situ* via electrochemical impedance spectroscopy

In addition to the above-mentioned challenges, development of an effective oil-resistant membrane depends on a successful characterization of its performance against model oily waters. Therefore, detection of wetting and fouling during MD is crucial in the development of such membranes as well as in mechanistic understanding of oil wetting and fouling in the MD of oily waters. In MD, wetting and fouling are traditionally detected by online monitoring of permeate electrical conductivity (EC) and the permeation flux during the process. However, these parameters can only provide limited macroscopic information about the process. In this regard, *in-situ* wetting and fouling monitoring methods can provide a better understanding on these phenomena. Electrochemical impedance spectroscopy (EIS) is one of the versatile *in-situ* monitoring methods that can be used for this purpose [19, 69-75]. EIS can be used to measure the electrical impedance of the system by applying an alternating current to the system at different frequencies. The measured impedance can then be analysed to observe the changes in the physical properties of the membrane as well as feed and permeate solutions. Prior studies in this field mainly utilized single-frequency measurements to track the reduction in impedance during MD, and associated these changes to the change in membrane properties and the occurrence of wetting [19, 70-75]. However, in theory, changes in other process parameters can also affect the value of impedance at any selected frequency during wetting. Nevertheless, there are limited *in-situ* EIS studies in MD that utilized a wide frequency sweep [69] and there is a lack of studies in the application of this method for studying oil wetting and fouling in MD.

### 1.7 Research Objectives

The aim of the current research is to develop a salinity responsive MD membrane by grafting a polyelectrolyte onto the surface of a hydrophobic membrane. For this purpose, a negatively charged polyelectrolyte (PAA) was found to be a suitable candidate to graft on a commercial hydrophobic polyvinylidene fluoride (PVDF) membrane to create oil-resistant membranes, namely PVDF-PAA membranes. The grafting of PAA performed using UV-assisted ATRP under open atmosphere is a first time according to state of the art. The morphology and chemistry of the surface-grafted membranes can be analysed and techniques confirmed using various methods such as attenuated total reflectance Fourier transform infrared spectroscopy (ATR-FTIR), scanning electron microscopy (SEM), and streaming potential analysis. In addition, the hypothesis of the oil-fouling/wetting resistance of the salinity-responsive PVDF-PAA membrane will be verified via underwater oil adhesion tests under Milli-Q water and aqueous saline solutions with various NaCl concentrations (i.e., 0.001 M to 3 M). The focus will be on the industrially relevant, but less studied saline unemulsified oil, by making a model solution consisting of 0.1 % (v/v) dodecane and 0.1 M NaCl tested in direct contact membrane distillation (DCMD). The

model solution employed in the current fundamental study demonstrates many of the fundamental characteristics of real oily wastewaters. However, it should be noted that real oily wastewaters are often more complex and contain various types of salts, oils, surfactants, and particles that can affect their surface adhesion properties and wetting characteristics. In addition, the model oil chosen for the current study (dodecane) is an alkane oil with simple linear structure that does not contain any polar groups or branches. This ensures that the oil under study predominantly exhibits hydrophobic properties and its adhesion to membrane surfaces is mainly driven by hydrophobic interactions. While this might not be the case for different types of oils, understanding the effects of hydrophobic interactions can provide insight on preparing effective adhesion-resistant membranes that can withstand feeds containing a broader range of oils.

Real-time *in-situ* EIS measurements were included in the plan, analysing a commercial hydrophobic PVDF membrane exposed to a synthetic oily solution in MD treatment. EIS will also be applied to analyse the performance of the grafted PVDF-PAA membrane. The novel feature of the *in-situ* EIS studies is the application of wide frequency sweep (from 1 Hz to 500 kHz).

Therefore, current study involves five major scientific objectives and corresponding approach as listed below:

1. **Bridge the gap in knowledge between the surface science and MD literature:** This will be addressed by applying fundamental knowledge from surface and colloid science literature to MD membranes to better explain colloidal adhesion in MD;
2. **Demonstrate the novel, scalable oxygen tolerant UV-assisted ATRP concept:** Reactions will be performed in open atmosphere to graft PAA brushes onto the surface of a commercial PVDF membrane and testing performance in MD;
3. **Show the performance of salinity responsive membranes for MD:** This is done using the surface-grafted negatively charged PAA brushes;
4. **Present evidence for the new type of Janus MD membrane for oily water treatment:** here the top of the roughness features is coated with patches of a hydrophilic compound (e.g., PAA); and
5. **Extend knowledge of EIS for MD analysis:** analyse oil wetting in MD by *in-situ* EIS especially using wider frequency ranges to provide more depth in the findings, which has not yet been presented in literature.

### 1.8 Thesis Layout:

The approach undertaken and findings from this study to address the goals are presented over the following eight chapters:

- **Chapter 1:** Introduction and research objectives (the current chapter);

## Chapter 1 Introduction

- **Chapter 2:** A literature review on the effects of surface interactions in the adhesion of colloidal particles onto MD membranes;
- **Chapter 3:** The materials and methods applied in the current research;
- **Chapter 4:** The results of the preliminary investigations on the surface grafting results using UV-assisted oxygen-tolerant ATRP;
- **Chapter 5:** The results and discussions on the characteristics of the PVDF-PAA membranes as well as their behaviour against oily waters;
- **Chapter 6:** The proposed conceptual models that can explain the surface chemistry and underwater oleophobicity of the PVDF-PAA membranes;
- **Chapter 7:** The results and analyses of the *in-situ* MD-EIS studies on the PVDF and PVDF-PAA membranes for oil fouling and wetting studies; and
- **Chapter 8:** Conclusions and future directions

## Chapter 2 Literature Review

---

### 2.1 Introduction

Membrane distillation (MD) is a thermal-driven membrane process that can deal with highly concentrated streams. The applications of MD have been studied for a broad range of feed solutions employed in many industries including oil and gas, food, municipal wastewater, seawater desalination, textiles which can contain a combination of dispersed and emulsified oils [8]. Most of the MD studies on oily wastewaters involve the use of emulsified oily solutions [8], while there has been an increasing interest in dispersed (un-emulsified) systems due their abundance in the industries mentioned above [6, 9-23]. Herein, the wastewaters containing dispersed oils are referred to as oily waters. Treatment of oily waters using MD poses many challenges regarding the adhesion of oil droplets onto the membrane surfaces leading to blockage of pores and eventually membrane wetting. To address these issues, membranes with special functionalities have been developed by tuning the surface properties of the membranes to resist against oil adhesion. These membranes include omniphobic [24] and hydrophilic-hydrophobic Janus [25, 26] membranes. Omniphobic membranes have a re-entrant surface topography and are coated with hydrophobic compounds to lower their surface energy [24]. Hydrophilic-hydrophobic Janus membranes consist of a hydrophilic top layer and a hydrophobic substrate with the former facing the feed solution [25, 26].

Oily waters are often categorized as a type of a broad class of solutions, namely, the colloidal dispersions (or simply colloids) [76]. Colloids are broadly defined as multiphase systems where the size of the dispersed particles or droplets (colloidal particles) usually ranges from a few nanometers to tens of micrometers. In this study, the definition of colloids is limited to the dispersions in which the matrix phase is liquid. Similar to other colloids, the adhesion of oil droplets to membrane surfaces are governed by the surface interactions between the droplets (colloidal particles) and the membrane. In addition, as suggested by the studies on the mechanism of oil adhesion onto Janus and omniphobic membranes, underwater oleophobicity is an important characteristic in the resistance of MD membranes against the adhesion of oil droplets [8, 25].

Therefore, the design of oil resistant membrane for MD requires the understanding of two aspects, namely, surface interactions and underwater oleophobicity. While these two aspects are fundamentally related to each other, they have different roles in the dynamic process of pore blockage and wetting. It is hypothesized that, for the membrane to become wetted, the oil droplets should first be able to reach the membrane surface and adhere to it. For oils, this stage is mainly governed by the same principles as in the surface interactions between colloids and flat surfaces. Subsequent spreading of the oil droplet on the membrane surface and its intrusion into the pores is governed by the underwater wettability principles and spreading of the oil on the membrane



surface. While underwater oleophobicity has been the focus of many studies [6, 7, 9-18, 20-23], the study of surface interactions is at its early stages in MD and has been gaining increasing attention over the recent years [28-31]. Nevertheless, despite the presence of a rich literature in surface and colloid science on surface interactions, the accumulated knowledge in this field has not yet been adequately adopted for understanding fouling in MD membranes. Therefore, the main focus of this literature review chapter is to bridge this gap by exploring the underlying physics of surface interactions and their effect on colloidal adhesion in MD.

The scope of the discussions in this chapter broadly encompasses all colloidal feed solutions within the simplifying assumptions that will be discussed further in each section. This approach is aimed to provide a better understanding of the behaviour of colloids in MD considering the wide range of feed solutions that can be treated using this process. The variety of the chemicals that can adhere to the membranes can exist in different forms, ranging from single dissolved molecules to a collection of the molecules. However, unless stated, for simplicity, the colloidal particles discussed in this review are assumed to be spherical with a smooth and chemically homogeneous surface. Additionally, here, unless otherwise stated, it is assumed that the colloidal particles are rigid and their interfaces are not mobile. Although some of these assumptions are in contrast with the properties of liquid droplets such as oils, they can still capture the most important aspects of surface interactions for these systems leading to the attachment of oil droplets.

To systematically explore the literature on surface interactions relevant to MD, this literature review will be presented as follows:

- The interfaces involved in colloidal adhesion in MD (**Section 2.2**);
- Types of surface interactions and the effects of surface chemistry and feed solution properties, as well as interaction force between colloidal particles and smooth and nonporous flat surfaces (**Section 2.3**);
- The effect of surface topography, chemical heterogeneities, and their combined effects on the surface interactions between flat surfaces and spherical particles (**Sections 2.4, 2.5, and 2.6**);
- The above reviewed features considered in the context of the surface interactions in MD membranes and strategies to create adhesion-resistant membranes (**Section 2.7**);
- Review the state of the art on *in-situ* wetting and fouling detection by electrochemical impedance spectroscopy (EIS) (**Section 2.8**); and
- Summary of findings of this literature review (**Section 2.9**).

## 2.2 Interfaces involved in colloidal adhesion

The interfacial surface interactions of the MD membranes should be considered in the context of operation conditions, i.e., when the membranes are brought into contact with the feed solution. In

this state, the MD membranes consist of composite interfaces with a combination of solid (membrane)-water and air-water interfaces. In hydrophobic, superhydrophobic, and omniphobic membranes, the solid-water and air-water interface is formed on both the top surface and the pore entrances [24]. However, in Janus (hydrophilic-hydrophobic) membranes, the air-water interfaces can be located below the top layer, while the solid water interfaces facing the feed solution can form on the top surface of the membrane [25, 26]. A schematic representation of the simplified models for the mentioned membranes is shown in **Figure 2.1**. In the models shown in this figure, for simplicity, the surface roughness is assumed to be limited to the top surface of the membranes.

The position of the solid-water and air-water interfaces depend on the wetting regime of the surface. On the one hand, the Cassie-Baxter wetting regime describes a metastable state, in which the rough surfaces are in partial contact with the liquid (here, water) and the liquid partially intrudes the space in between the roughness features [77, 78]. On the other hand, the Wenzel regime describes a thermodynamically stable regime in which the liquid completely contacts the solid rough surface, without any trapped air pockets [77, 78]. The Cassie-Baxter regime is expected to commonly occur during MD, where hydrophobic, superhydrophobic, and omniphobic membranes are in use [24, 78]. In these cases, as shown in **Figure 2.1**, a combination of air-water and solid-water interfaces are formed on this surface, which can interact with the colloidal particles in the feed solution. The Wenzel state can be expected to form on all of the mentioned membrane types as well as Janus membranes due to its thermodynamic origin [78]. In this case, the feed liquid only forms solid-liquid interfaces on this surface that can participate in the surface interactions in MD. For a functioning MD membrane, the air-water interfaces are located at some point inside the pores regardless of the wetting state of the top surface (or generally, regardless of the wetting state of the lowest level of hierarchy in a hierarchically rough membrane). Therefore, this air-liquid interface is expected to be present in all MD membranes, but its position relative to the pore depth depends on the design of the membrane, and its role in the colloid-membrane interactions depends on whether this interface can directly be exposed to the colloidal particles.

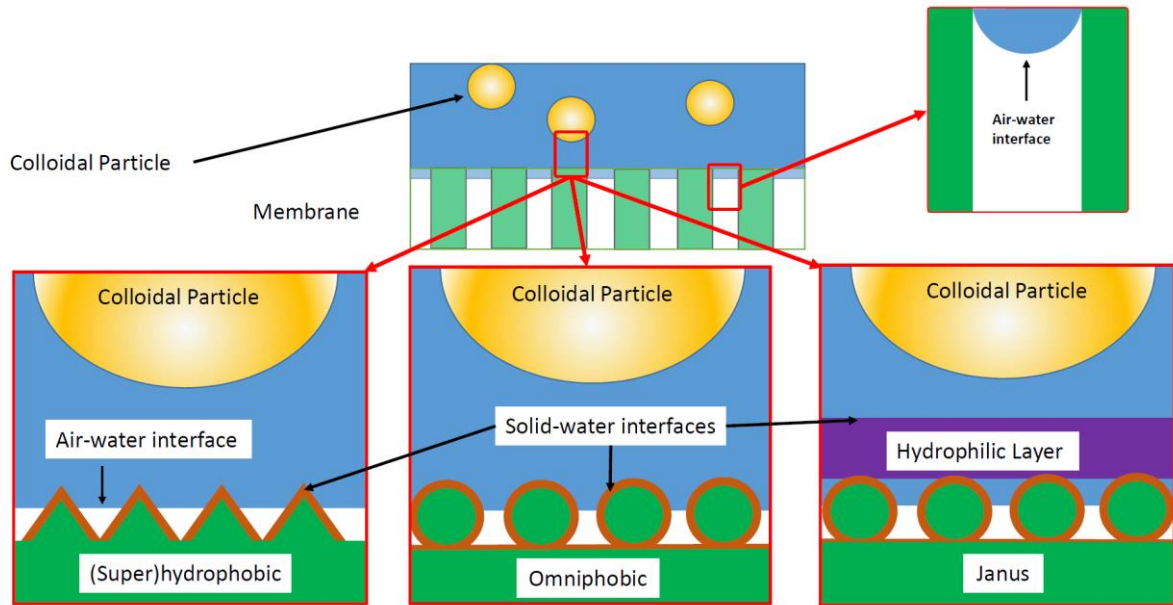


**Figure 2.1:** Schematic illustration of the interfaces involved in surface interactions between different types of MD membranes and colloidal particles. The hydrophobic and superhydrophobic surfaces have roughness features with converging, straight, or randomly rough cavities, while the roughness features of the omniphobic membranes usually have re-entrant (converging-diverging) cavities. The Janus membranes can have either of the hydrophobic, superhydrophobic, or omniphobic surfaces as its substrate. The shown schematics are only examples of these membranes for illustrating the positions of the solid-water and air-water interfaces.

The complexity of the interfaces involved in the colloid-membrane surface interactions in MD requires specially designed theoretical and experimental research to properly investigate these effects on particle adhesion and subsequently on performance reduction. However, this topic is in its early stages with only a few works in this area from 2017 to 2023 [28-31]. Therefore, here, the full model of the interfaces in MD membranes is broken down to four simpler cases that can be analysed individually on the role of the surface interactions in particle adhesion and how the surface properties affect these interactions. Later on, a general understanding can be obtained by combining these four scenarios. These cases/scenarios involve:

- **Case 1:** A smooth flat surface with homogeneous chemical composition;
- **Case 2:** A rough flat surface with homogeneous chemical composition (in Wenzel state);
- **Case 3:** A smooth flat surface with chemical heterogeneities; and
- **Case 4:** A rough flat surface with chemical heterogeneities and generalization to MD membranes.

Cases 1-3 are assumed to be nonporous unless otherwise stated. These cases are discussed to introduce the fundamental concepts that are later used to form Case 4, which is the porous structure of the MD membranes described in Figure 2.1. In addition, in Cases 1-3, the flat surface is assumed to be nonporous unless otherwise stated. The above-mentioned four cases will be discussed in **Sections 2.3 to 2.6**, followed by a discussion on MD membranes in **Section 2.7**. Throughout the discussions, it is attempted to constantly link these different interactive phenomena with observations in MD membranes.

## 2.3 Surface interactions between a smooth nonporous flat surface with homogeneous chemical composition and a spherical colloidal particle (Case 1):

### 2.3.1 Theory of surface interactions

Surface interactions in colloidal systems are often explained using the well-known DLVO theory, named after the scientists proposing this theory, B. Derjaguin and L. Landau, E. Verwey and T. Overbeek) [76]. According to this theory, the interaction energy between two surfaces at the distance  $h$  from each other,  $U(h)$ , is described as the sum of induced dipole-dipole interactions (LW energy) and the electrostatic interactions:

$$U(h) = U_{LW}(h) + U_{EDL}(h) \quad \text{Equation 2.1}$$

Where  $U_{LW}(h)$  is Lifshitz-Van der Waals (LW) interaction energy which is the result of dipole-dipole interactions between the surface materials, and  $U_{EDL}(h)$  is the electrical double layer (EDL) interaction energy arising from the electrostatic interactions between surfaces. It is sometimes more informative to demonstrate the surface interactions in the form of interaction force,  $f(h)$ , which can be obtained from the gradient of the interaction energy in the direction perpendicular to the surface [76]:

$$f(h) = -\frac{dU(h)}{dh} \quad \text{Equation 2.2}$$

Throughout this review, we will use both interaction energy, and interaction force when appropriate. LW and EDL interactions found in the surface science literature [76, 79, 80] will be briefly discussed here.

Lifshitz-Van der Waals interaction energy,  $U_{LW}(h)$  arises from the orientation (Keesom), induction (Debye) and dispersion (London) interactions of the electrical dipoles created by the electrons and protons of the constituent atoms and molecules of the interacting surfaces.

Therefore, these forces are the very property of all materials and are present between all surfaces in all types of media (i.e., gas, liquid, and vacuum) [76, 79, 80]. There are multiple methods for evaluating the LW energy between a smooth flat surface and a spherical colloidal particle in water [81]. One of these methods follows [81, 82]:

$$U_{LW}(h) = 2\pi\Delta G_{h_0}^{LW} \frac{h_0^2 a}{h} \quad \text{Equation 2.3}$$

where  $a$  is the radius of the particle,  $h$  is the distance between two surfaces calculated from the closest points of each surface with respect to each other, and  $\Delta G_{h_0}^{LW}$  is the Gibbs free energy of LW interactions at  $h = h_0$  ( $h_0 \approx 1.58 \text{ \AA}$  is the minimum distance between two atoms limited by Born repulsions resulting from the overlap of the electronic clouds of the interacting surfaces) calculated as described in [81, 82]. The LW energy is attractive between most surfaces in water. Therefore, the sign of this energy is almost always negative in practice [81, 82]. These interaction forces would form the basis for how MD membranes interact with colloidal particles that can foul the membranes and reduce performance.

The electrical double-layer (EDL) interaction energy,  $U_{EDL}(h)$ , arises from the electrostatic interactions between surfaces. Most colloidal particles and hydrophobic polymeric membrane surfaces are negatively charged at neutral pH. The adsorption of ions from the solution, presence of charged functional groups tethered to the surface, or preferential orientation of water molecules near the surface are among the common sources of surface charge in membrane and colloidal particle surfaces [79, 80]. The charge-neutrality rule dictates that the surface charge will be compensated by an equivalent opposite charge in form of counterions in the solution. However, it has been found that the compensating counterions not only adhere to the surface but also form a diffuse layer known as electrical double layer (EDL) [76, 79, 80]. The EDL interaction between two charged surfaces can be attractive or repulsive depending on their charge [76]. Additionally, the decay length in the EDL interaction energy depends on the ion concentration in the solution. The concentration of ions better manifests itself in a parameter known as ionic strength ( $IS$ ) of the solution defined as:

$$IS = 1/2 \sum_{i=1}^n c_i z_i^2 \quad \text{Equation 2.4}$$

In which  $c_i$  and  $z_i$  are the molar concentration, and valance of the ionic species  $i$ , respectively. The electrical double layer extends into the solution with a decay length known as Debye length ( $\kappa^{-1} = \sqrt{\frac{\epsilon_s \epsilon_0 k_B T}{2e^2 (IS)}}$ , In which,  $\epsilon_0$  and  $\epsilon_s$  are dielectric permittivity of vacuum, and the relative dielectric permittivity of the liquid medium respectively. In addition,  $e$ ,  $k_B$ , and  $T$  are the charge of a single electron, the Boltzmann constant, and the temperature (K), respectively. Beyond this

distance, the effect of the surface charge on its environment becomes negligible. With an increase in the  $IS$  of the solution, the electrostatic repulsions are screened more by the presence of ions in the solution, and the thickness of the EDL decreases due to charge screening by the ions present in the solution.

The EDL interaction energy ( $U_{EDL}(h)$ ) between a smooth flat surface and a spherical particle calculated by one of the existing methods for this purpose is represented by [81, 82]:

$$U_{EDL}(h) = \pi \varepsilon_s \varepsilon_o a \left[ 2 \xi_m \xi_p \ln \left( \frac{1 + e^{-\kappa h}}{1 - e^{-\kappa h}} \right) + (\xi_m^2 + \xi_p^2) \ln(1 - e^{-2\kappa h}) \right] \quad \text{Equation 2.5}$$

Where,  $\varepsilon_s$  and  $\varepsilon_o$ , are the relative electric permittivity of the medium and the absolute permittivity of the vacuum ( $\varepsilon_o = 8.854 \times 10^{-12} \frac{C}{V.m}$ );  $\xi_m$ , and  $\xi_p$  are the surface zeta potentials of the membrane and the particle, respectively;  $h$  is the distance between the particle and the flat surface,  $a$  is the diameter of the particle, and  $\kappa^{-1}$  is the Debye length of the solution at a given  $IS$ .

The DLVO interaction energy between a negatively-charged sphere and a negatively-charged flat surface is presented in **Figure 2.2**, alongside the contributions from LW and EDL energies. As can be observed by the figure, there is a deep energy minimum (primary energy minimum) near the plate surface followed by an energy barrier due to repulsive EDL interactions followed by a shallow energy minimum (secondary energy minimum).

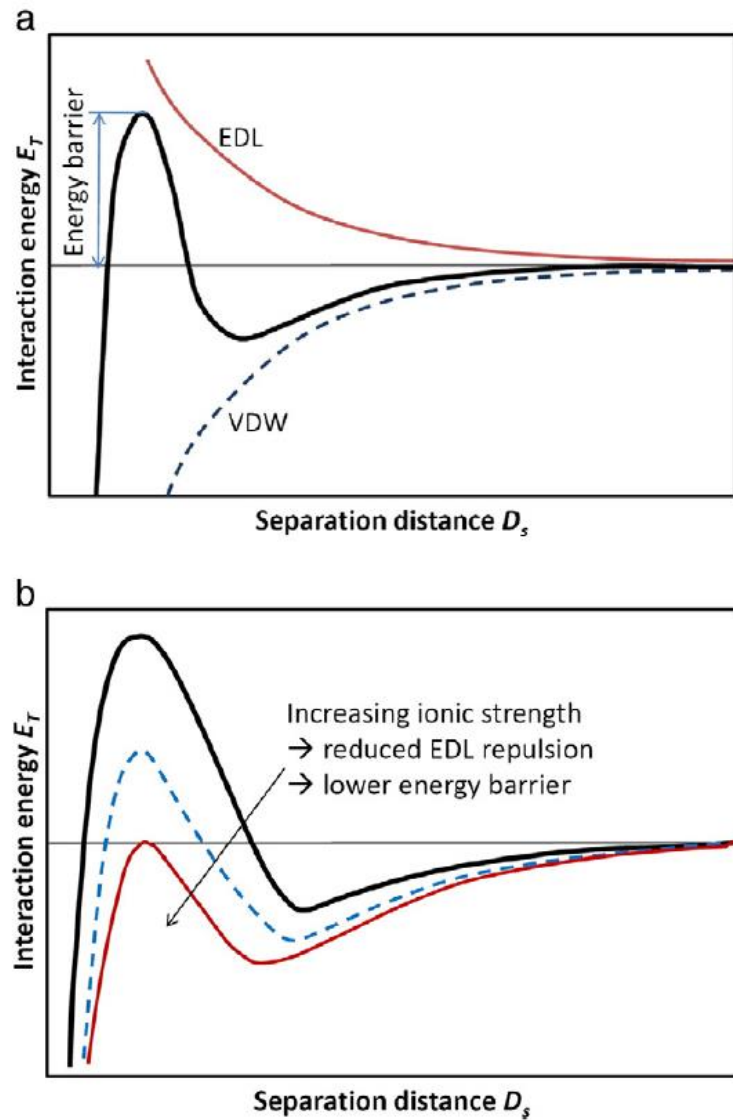


**Figure 2.2:** DLVO interaction energy between a flat plate and a spherical particle, (with permission from [83]).

### 2.3.2 Effect of $IS$ and ion valance

An increase in  $IS$  can lead to charge screening and decrease in Debye length, which may lead to the suppression of the energy barrier in the DLVO interaction energy subsequently leading to particle adhesion [76, 79, 80]. In addition, for multivalent ions, ion bridging can transform a repulsive interaction into attractive interaction even at low  $IS$  [76]. This is important in considering the feeds containing  $Ca^{2+}$  ions which are abundant in many surface waters and wastewaters. In presence of these ions, negatively charged surfaces can attract each other and lead to severe colloidal adhesion. This can happen between the surface of the membrane and colloidal particles or between two colloidal particles. With an increase in  $IS$ , monovalent or multivalent ions can adsorb onto different surfaces more readily. In some cases, this can lead to charge

reversal for the mentioned surface [84]. Charge reversal can also occur as a result of changes in the pH with surfaces becoming more negatively charged with increase in the pH due to the surface adsorption of  $OH^-$  ions [80].

### 2.3.3 Non-DLVO interactions

Although DLVO theory is widely-accepted in the literature, there are other types of surface interactions that are key to MD systems that are not accounted for in the formulation of this theory. These interactions are usually referred to as non-DLVO interactions [85]. Hydrophobic and hydration interactions [76, 79, 80] are among the major non-DLVO interactions that affect the adhesion of various colloidal particles on MD membranes.

Hydrophobic interactions occur between hydrophobic surfaces and are always attractive with an effective distance varying between a few to tens of nanometers [86]. Although hydrophobic interactions have been thoroughly studied in surface science, the underlying mechanism of this phenomenon is still an active topic of research [87-92].

Hydration interactions are related to the hydration of various chemical species on the surface by water, which creates a short-range but strong repulsive interaction energy between the hydrated surface and other surfaces (either hydrated or non-hydrated) [80, 93, 94]. Hydration interactions can be observed in hydrophilic surfaces containing functional groups that can form hydrogen-bonding with water or can be strongly hydrated by water molecules. These groups include ether, carbonyl, primary and secondary amines and carboxyl. Additionally, zwitterionic polymers can maintain a hydration layer due to the entrapment of water molecules in their structure [95-100]. A membrane surface or a colloidal particle with these groups on its surface exhibits hydration repulsion effect, when approaching another surface. The underlying mechanism of hydration interactions is still a topic of active research. It is sometimes described using acid-base (AB) (also known as electron-donor-acceptor) interaction energy, which is the result of Lewis-acid/base properties of the surface functional groups and those of the liquid medium (water) [101, 102]. The contribution from AB interactions is subsequently added to the DLVO theory to formulate the extended DLVO (XDLVO) theory which has been found to successfully explain some cases [29, 30, 81, 82, 102-107]. In other cases, it is common to use an empirical exponential function to describe this force between two hydrophilic surfaces [76]. It is worth noting that AB interactions are sometimes also used to explain the hydrophobic interactions [101].

Both hydrophobic and hydration interactions are influenced by the type and valency of ions in the solution [93, 108-115]. Each ionic species has a different hydration strength, therefore, it affects the hydrogen-bonded structure of water in different ways and with a different magnitude (the Hofmeister effect) [115]. The underlying mechanisms for the different behaviour of the ions in affecting surface properties is not well understood [93, 108-115].



Apart from the mentioned types of surface interactions, other types of surface forces such as capillary forces, steric repulsions, and depletion forces can influence the surface interactions between foulants (i.e., colloids) and membrane surfaces [76, 79, 80]. However, this review will mainly focus on DLVO forces and to some extent on hydrophobic interactions and hydration repulsions, as these represent MD systems more broadly. Additionally, where applicable, the effect of hydrodynamic forces will be discussed on the particle-membrane interactions.

#### 2.3.4 Effect of hydrodynamics

The total force applied on colloidal particles is the sum of hydrodynamic and surface interaction forces, which determines whether the particle can be brought into contact with the membrane surfaces. The adhesion and attachment of the particle then depends on whether the hydrodynamic shear force is large enough to overcome the adhesion force. After the attachment of the first particle, the adhesion of other particles is influenced by the attached particle as well as the underlying membrane surface. A membrane surface with attached particles is a new surface which can interact with the particles in a different way. To avoid the complexity related to dynamically changing interfaces, this review will only focus on the interaction of the colloidal particles with unfouled (clean) surfaces. The sequential surface adhesion follows the same principles of surface interactions between particles and surfaces, but involves the additional changes in surface properties caused by the adhesion of particles on the membrane surface [116, 117].

This section considered Case 1 where surfaces were smooth. However surface interactions between colloidal particles and membranes are also influenced by the topography, which will be discussed in the next section.

### 2.4 Effect of surface roughness on the interactions between MD membranes and foulants (Case 2)

As mentioned in **Section 2.2**, hydrophobic, superhydrophobic, and omniphobic MD membranes usually have different types of surface asperities (roughness features) on their top surface, which is exposed to the feed solution (**Figure 2.3**) [24]. For instance, in nanofiber membranes, the nanofibers and the nanoparticles (if applicable) comprise the asperities, while in other MD membranes the asperities are introduced to the surface by particle deposition, imprint lithography, or a combination of both [118-121]. Usually, the asperities and the membrane surface are further covered/coated/grafted with hydrophobic compounds to reduce their surface energy and enhance their anti-wetting properties. Therefore, understanding the effect of surface roughness on the surface interactions is important in designing membranes that can better resist particle adhesion.

In this section, the focus will be on the rough surfaces which are in Wenzel state and the liquid is in full contact with the roughness features. Therefore, the particles only interact with solid liquid interfaces. In addition, it is assumed that the membrane solid surface is comprised of a single compound showing homogeneous surface properties, and the surfaces have no pores unless stated

otherwise. Throughout this chapter, the interactions between surfaces with the same sign of the surface charge will be referred to as unfavorable interactions, while the interactions between oppositely charged surfaces will be referred to as favourable. It should be noted that attachment of particles to the membrane surface is the opposite of what is desired for MD membranes. However, since this terminology (i.e., favourable and unfavourable interactions) is widely used in colloid and surface science to refer to the particle attachment conditions, it will be adopted in the current discussions to avoid confusion.

#### 2.4.1 Cases where the size of the particles is larger than that of the asperities

The shape and size of asperities can affect the surface interactions between the membrane and foulant particles. If the foulant particle size is large as compared to the asperities, the asperities displace the point of contact between the particle and the membrane surface [86]. This makes the low-distance section of the energy-distance curve inaccessible due to the presence of the asperities. Conversely, if the particle size is small as compared to the asperity size, the interaction energy depends on the very location of the particles with respect to the asperities.

For instance, Martines et al. [122] studied the effect of asperity size and shape on the interaction energy between flat plates and spherical particles for two types of protruding asperities (hemispherical and cylindrical) under unfavourable attachment conditions. They found that an increase in the height of the asperities leads to the suppression of the DLVO energy barrier, and leading to particle adhesion. They also found that the hemispherical asperities reduced the energy barrier to a greater extent as compared to the cylindrical asperities. In another study, Henry et al. [123] investigated the deposition of particles using DLVO theory on a rough surface generated by random placement of hemispherical protrusions under both attractive and repulsive conditions. The authors found three parameters that play an important role in determining the surface interactions: roughness, surface coverage of asperities, and retardation of van der Waals interactions. It was found that the presence of roughness even at a very low surface coverage could lead to particle adhesion despite being under unfavourable conditions. With an increase in asperity radius, the height of the energy barrier was found to decrease until a critical asperity size was reached. Beyond the critical asperity size, the interactions between asperity and particle becomes comparable to the base surface of the plate (**Figure 2.3**). Therefore, above the critical asperity size, an increase in asperity size leads to an increase in the height of the energy barrier. The critical asperity size was found to increase with particle size and Debye length (**Figure 2.4**) [123]. The effective area of interaction of the particle increases with an increase in particle size. Therefore, for larger particles, the asperity diameter should increase further for the asperity to contribute more significantly as compared to the base surface. Therefore, a larger particle corresponds to a higher asperity critical radius.

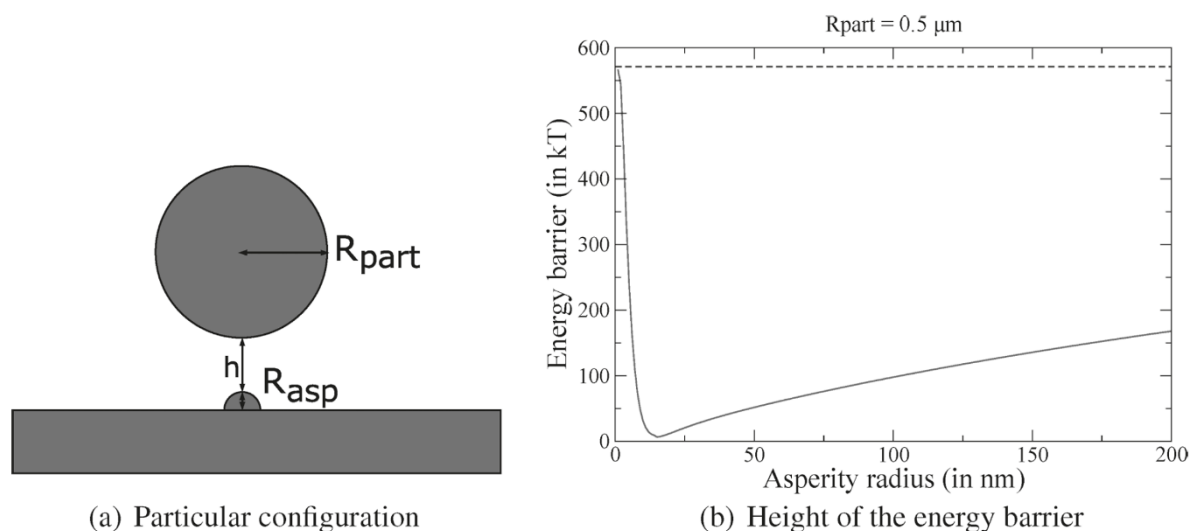


**Figure 2.3:** a) Schematic of the model used to calculate the interaction energy between a spherical particle and a rough plate, b) Changes of the energy barrier height of the shown model system with asperity radius for a particle with  $D = 5 \mu m$  under unfavorable attachment conditions. The dotted and the solid lines in the graph represent the energy barrier of the rough and smooth surface (in the absence of the asperity), respectively (with permission from [123]).

It was also observed that the critical asperity radius increases with an increase in Debye length (decrease in  $IS$ ) (**Figure 2.4**). This can be attributed to an increase in the electrostatic zone of influence (ZOI) of the particle on the plate surface, which is the projection of the effective area of the particle that has the most effective interaction with the plate surface. Its radius is defined as the geometric mean of the particle radius and Debye length [124]. A large ZOI means that the particle is influenced by a larger area on the flat surface, which in turn means that the interactions will be determined by the average surface properties of the flat plate. In contrast, with a smaller ZOI, the influence of asperities increases on the particle-plate interactions. This parameter will be described in more detail in **Section 2.5**.

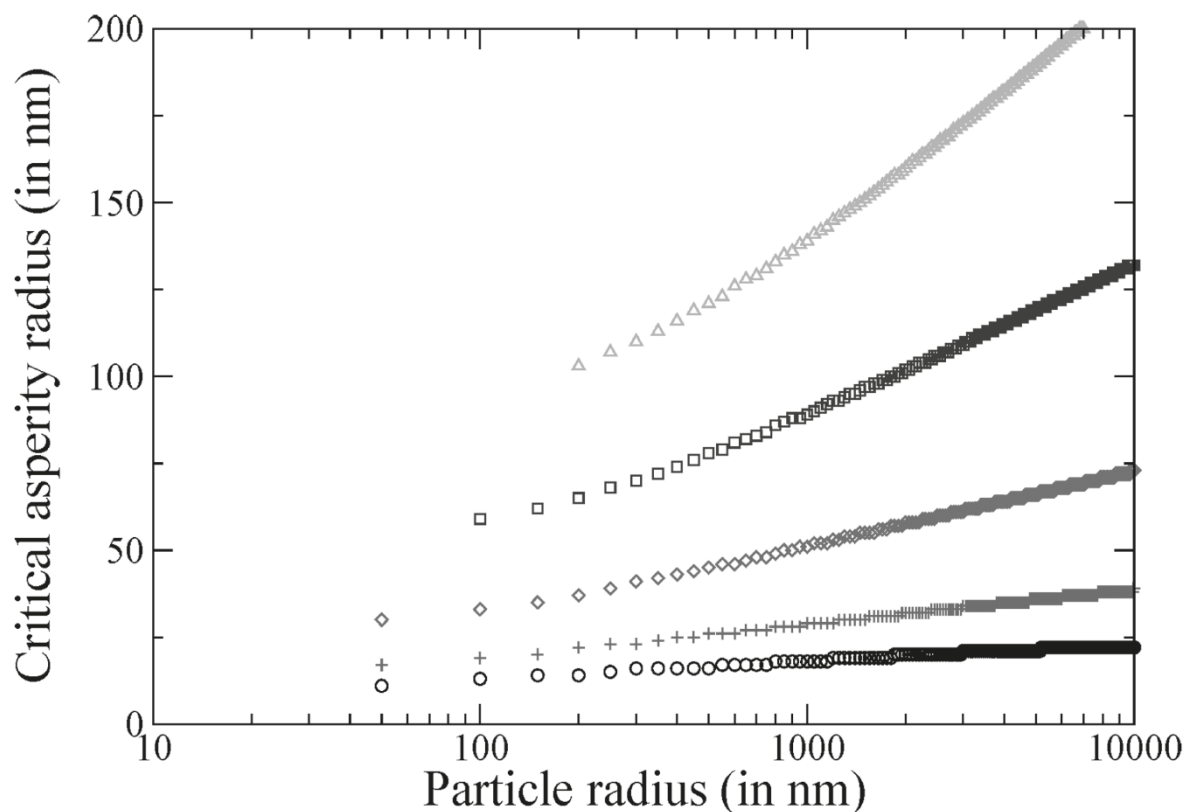


**Figure 2.4:** Changes in the critical asperity size as a function of the particle radius and Debye length ( $\kappa^{-1}$ ): circles for  $\kappa^{-1} = 3 \text{ nm}$ , plus marks for  $\kappa^{-1} = 5 \text{ nm}$ , diamonds for  $\kappa^{-1} = 10 \text{ nm}$ , squares for  $\kappa^{-1} = 20 \text{ nm}$ , triangles for  $\kappa^{-1} = 35 \text{ nm}$ , (with permission from [123]).

$IS$  is an important solution parameter that can affect the interactions between particles and rough surfaces. Similar to what was described in **Section 2.3**, an increase in ionic strength leads to a reduction in the range of the electrostatic interactions. Usually, if solution Debye length is much larger than the asperity size, the presence of the asperities does not significantly affect the surface interactions. However, when Debye length decreases (with increasing  $IS$ ) and becomes comparable to the asperity size, the effect of the asperity becomes notable. Another effect of the increase in  $IS$  is the increase in the depth of the secondary energy minimum (**Figure 2.2**), which can trap foulant particles. Therefore, roughness can in general lead to an easier adsorption of foulants at high ionic strengths. However, it should be noted that the adhesion due to the secondary minimum is reversible, and can be undone by decreasing the ionic strength. In addition, the presence of asperities also hampers the access of colloidal particles to the DLVO primary minimum located in the base of the asperities. This means that the particles can no longer irreversibly adhere to the surface, and can be detached from the surface more easily by washing with a low-ionic-strength solution.

In conclusion, in Case 2, if the particle size is comparable or larger than the size of the asperities, the DLVO interaction energy barrier between the flat surface and the particle is suppressed as compared to the case of an equivalent smooth surface (Case 1). The energy barrier in this case goes through a minimum with increasing asperity size and the minimum value depends on the solution Debye length (i.e.,  $1/S$ ). Generalization of these findings to MD should be performed with caution, as Wenzel state is the basic assumption of calculating the interactions in Case 1. Assuming a Wenzel state for the rough surfaces in MD, asperities smaller than the colloidal particles can lead to a higher likelihood of particle adhesion onto MD membranes. However, the detachment of the particles from the surfaces are also affected by the presence of the asperities. These effects will be discussed in **Section 2.4.5**.

#### 2.4.2 Cases where the size of the particles is smaller than that of the asperities

Unlike smooth surfaces, the surface interactions between particles and rough surfaces can be different over different regions of the surface, especially when the size of the particles is smaller than that of the asperities. In the above example (**Figure 2.3a**) the vertical position of the particle is located directly above the asperity top (axis of symmetry). However, if the particle is placed directly over the top of the valley area between two asperities, the interactions would be slightly different [122]. Therefore, it is more informative to plot the energy map of the interaction energy at different regions near the surface of the plate [125-129]. **Figure 2.5** shows an example of such energy maps obtained by Shen et al. [129] for the interaction energy between spherical particles and hemispherical asperities with different diameters under unfavourable attachment conditions. It was found that the height of the energy barrier was reduced at the top of the asperities, while it was enhanced at the base of the asperity. Additionally, it was found that the secondary energy minimum was enhanced at the base of the asperity which could trap the particles near the surface.

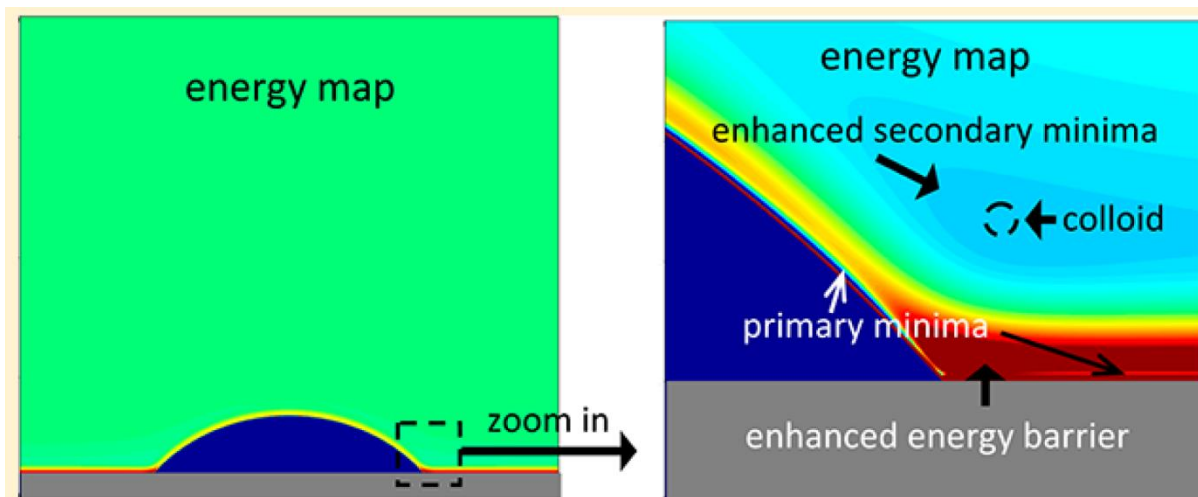


**Figure 2.5:** An example of the energy maps plotted by Shen et al. [129]. The regions of the primary and secondary energy minima as well as the energy barrier can be observed in the magnified view of the map (with permission from [129]).

Similar graphs have been obtained for surfaces with random roughness by other researchers [125, 128]. **Figure 2.6** shows an example of these maps which is overlaid on an image simulated based on an AFM image [125]. Similar to the case of hemispherical asperities, it can be observed in **Figure 2.6**, that the energy barrier is increased at the valleys, while it is lower at the top of the asperities, and it is attractive in some areas.

It can be concluded that in Case 2, if the size of the particles are smaller than the asperities, the surface interactions can be different on different regions of the surface. In MD, assuming a Wenzel state for the asperities, it can be conjectured that some areas such as the top of the asperities are more likely to attract the colloidal particles, while the base surface and the bottom of the roughness features are protected by the enhanced DLVO energy barrier. Nevertheless, each specific case of the MD membrane should be analysed in detail to for a more accurate determination of these effects,

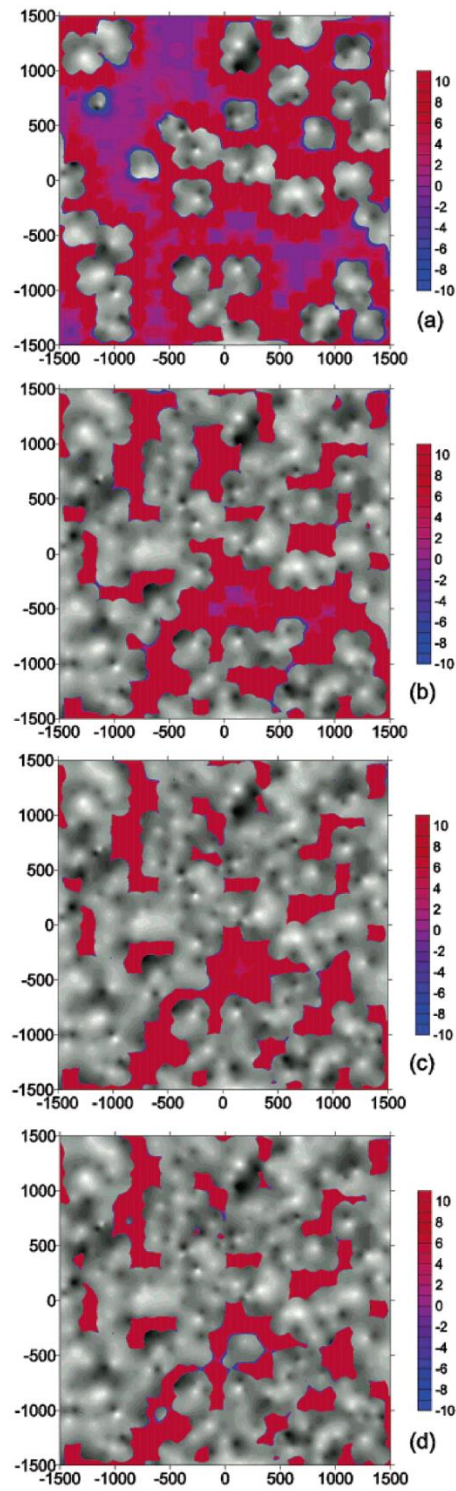


**Figure 2.6:** Map of the interaction energy for a particle of radius=50 nm approaching a simulated rough surface with separation distances of a) 50 nm, b) 25 nm, c) 10 nm, and d) 5 nm. In the above energy maps, x and y axes are in nm, and the colour bar on the right side of each map is in the units of  $k_B T$  (figure with permission from [125]).



### 2.4.3 Surfaces with random or hierarchical roughness features

The developments in membrane fabrication methods over the past years have enabled the preparation of MD membranes with controlled topography [24]. However, the surface roughness of most of the MD membranes developed in the literature can be classified as random or hierarchical roughness [130, 131]. Accordingly, to apply DLVO theory on these membranes, the topography of their surfaces need to be quantified first, using an appropriate model. This is a challenging task due to the complex geometry of these surfaces. To address this problem, it is useful to model the surface using surface fractal models. One of the fractal models that has been studied for this purpose is the Weierstrass-Mandelbrot (WM) model which has two important parameters to characterize the surface: fractal dimension (D) and fractal roughness (G). Feng et al. [132] modelled the rough surface of membrane bioreactor (MBR) membranes using WM model, and found that an increase in fractal roughness leads to enhancement of the attraction between foulants and the membrane under favourable conditions. Wang et al. [128] studied the effect of the parameters of WM model and found that at low fractal dimensions, increase in roughness height decreased the DLVO energy barrier between a nanoparticle and a randomly rough surface. Additionally, at a constant G, the energy barrier increased with D. In treating the surfaces with random roughness, the relative size of the smallest surface feature to the particle size plays a vital role. If the smallest surface feature becomes comparable in size with the particle, the surface interactions between the particle and surface can be enhanced compared to the flat surface. Therefore, the height of the energy barrier and the depth of the energy minimum increases under unfavourable conditions and favourable conditions, respectively. In contrast, if the projected area normal to the plate of the smallest roughness feature is significantly smaller than the particle, it dampens both attractions and repulsions. A fractal roughness has multiple levels of roughness which further complicates the analysis. Therefore, the results for the interactions between different surfaces and different particles can vary depending on the relative size of the particle and each level of hierarchy.

In conclusion, the MD membranes are usually fabricated with random or hierarchical roughness features. The length scale of some levels of hierarchy could be larger and some levels smaller than the colloidal particles under study. Therefore, a combination of the effects discussed in **Sections 2.4.2** and **2.4.1** apply for these surfaces. In addition, a quantitative study of the surface interaction on these surfaces sometimes requires the application of fractal models which adds further complexity to such investigations.

### 2.4.4 Interactions leading to colloidal deposition on rough surfaces

According to the above discussions, the surface interactions between colloidal particles and membrane surfaces can be affected by the presence of surface asperities. Now, the question is how effective these surface interactions are in the actual deposition of the particles on the



membrane surfaces. In other words, are these interactions strong enough to lead to the attachment of the particles to the membrane surface?

According to the DLVO theory, attachment and deposition of particles on membrane surfaces requires that the particles to be trapped in one of the primary or secondary energy minimum regions. Additionally, if the shear forces exerted by hydrodynamic flow on the particle are strong enough, particles can be carried with the flow instead of adhering to the membrane surface. These effects have been taken into account by several researchers [129, 133-136]. For instance, Shen et al. [129] found that for hemispherical asperities under unfavourable attachment conditions, the force map was skewed toward the back side of the asperities due to the hydrodynamic flow as shown in **Figure 2.7**.

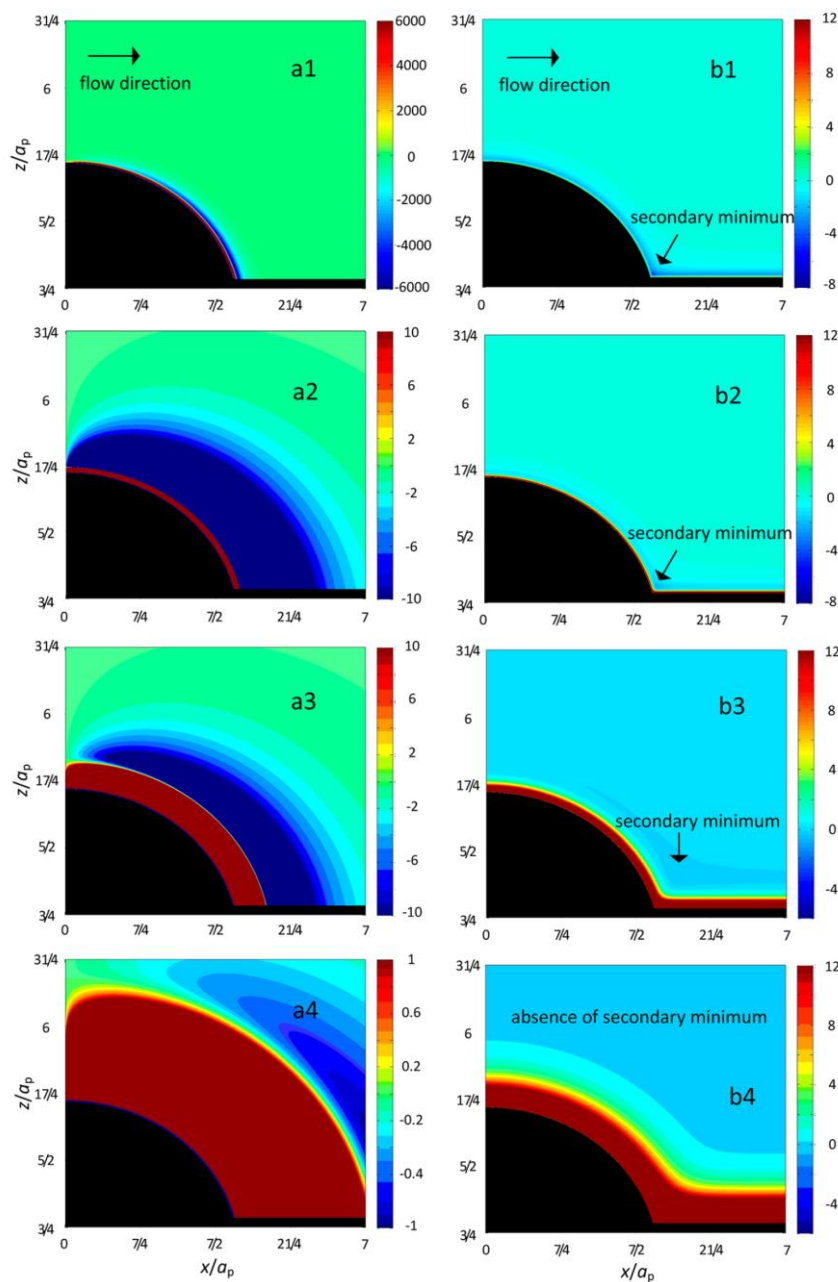


**Figure 2.7:** DLVO interaction force map normalized by the hydrodynamic drag force a), and (b) interaction energy (colour bars are in the units of  $k_B T$ ) for a colloidal particle with a diameter of the 66 nm interacting with an asperity with the radius of 100 nm at different ionic strengths (1: 0.2 M; 2: 0.1 M; 3: 0.01 M; 4: 0.001 M). The axes are normalized by particle diameter (with permission from [129]).

Particle deposition has been studied on rough surfaces under favourable conditions accounting for the hydrodynamic effects [133]. It was found that the deposition rate of the particles on rough surfaces pass through a minimum with an increase in the asperity radius (**Figure 2.8**). For these systems, with an increase in roughness size, the point of contact is displaced further from the flat surface decreasing the attraction. At the same time, an increase in the size of the asperities leads to an increased contribution from the asperities to the surface interactions. These two effects work in the opposite of one another creating a critical point.

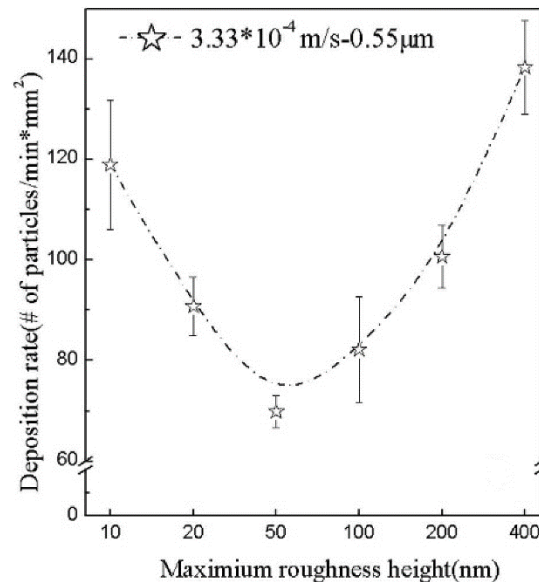


**Figure 2.8:** Dependence of particle (diameter= 0.55  $\mu\text{m}$ ) deposition rate ( $\frac{\text{number of particles}}{\text{min}\cdot\text{mm}^2}$ ) on the roughness height under unfavourable attachment conditions in the loading rate of  $3.33 \times 10^{-4} \text{ m/s}$ . A critical asperity size can be observed at the roughness height  $\cong 50 \text{ nm}$  (with permission from [133]).

In another study, Kemps and Bhattacharjee [134] investigated the attachment of particles under favourable conditions on rough surfaces with different arrangements (in-line vs staggered) of the asperities. An example of the particle-deposited surfaces with different arrangements of the asperities are shown in **Figure 2.9**. It was found that the particle trajectory around the asperities was controlled by the hydrodynamic flow in a way that they went over the asperity and the particles could not come into contact with the region behind the asperities. Therefore, a protected region formed behind the asperities, which despite its attractive surface forces, particles cannot

reach because of the hydrodynamic flow over the asperities. As a result of that, most of the particle deposition took place at the regions of the asperities facing the flow (**Figure 2.9**). In addition, due to the protective effect of the asperities, the in-line arrangement showed a lower deposition on the asperities located in the middle and the end of the studied region as compared to the staggered arrangement (**Figure 2.9**). This signifies the importance of the arrangement of the asperities on the surfaces.

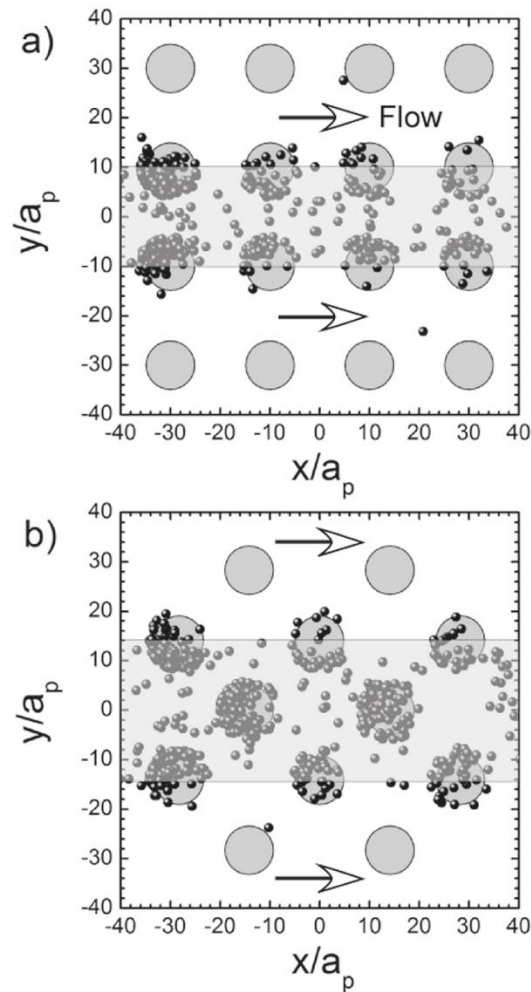


**Figure 2.9:** Top view of the particle deposition results on a surface roughened with spherical asperities in a) in-line and b) staggered configurations under favourable attachment conditions. The particle Peclet number is 1.4. The arrows show the direction of the flow (with permission from [134]).

In the context of MD membranes, the particle deposition can be conjectured to follow the same trend as discussed in **Sections 2.4.1 to 2.4.4** depending on the relative size of the particles and the asperities. For unfavourable conditions, the deposition rate is expected to go through a maximum with an increase in the asperity size, while for favourable conditions (which are to be avoided in MD), it is expected to go through a minimum.

#### 2.4.5 Particle detachment from rough surfaces

Particles detaching from the surface of rough surfaces under flow conditions is another important topic which deserves a special attention. Raveendran and Amirtharajah [135] investigated the detachment of polystyrene colloidal particles from glass beads in packed fluidized beds. They have calculated the forces exerted on the particles by hydrodynamic drag and lift, as well as the surface interactions. The surface interactions were modelled using the combination of van der Waals, Born, EDL, and hydration interactions. When the hydration effects were ignored, the interactions could not reproduce the observed experimental trends, suggesting that these forces played a determining role in the detachment force. Additionally, a distinction is made between adhesion forces and detachment forces. Water is the medium in calculating the LW adhesion forces, while for the detachment forces the medium is vacuum and the van der Waals attraction is higher. The effects of pH and ionic strength have been investigated on the particle detachment in this study. It has been found that an increase in pH and a decrease in ionic strength lead to a higher detachment efficiency, due to the reduction in the depth of the first energy minimum in DLVO interaction energy plot. It should also be noted that divalent ions have been used in the solution in the mentioned study. These ions can induce bridging effect between interacting surfaces that can lead to attractive forces between the flat surface as the particles with the charge of the same sign. Therefore, by decreasing the ionic strength of divalent ions, the bridging effect also decreases and leads to easier detachment.

Shen et al. [136] studied the detachment of nano- and micro-particles from glass beads. They first deposited the particles from a solution containing a divalent salt ( $\text{CaCl}_2$ ), and then used washing solutions with different concentrations of a monovalent salt ( $\text{NaCl}$ ) to detach the particles. In contrast to other research, they found that with an increase in the ionic strength of the washing solution, the detachment efficiency increases. This was attributed to the ion exchange between  $\text{Ca}^{2+}$  and  $\text{Na}^+$  ions. In addition, it was found that the presence of asperities decreased the detachment energy barrier. With an increase in the size of the asperities (**Figure 2.10**), the energy barrier for detachment gradually increased going through a minimum and was lower than the energy barrier of the smooth surface up to a certain asperity size for each ionic strength and particle size. Beyond this size, the detachment energy barrier crossed the smooth surface value under each condition, meaning that the detachment of the particles from a surface with large asperities became more difficult than that from a smooth surface under equivalent conditions. Moreover, the authors studied the depth of the secondary minimum in their system and found that its effect became noticeable at high ionic strengths of the washing solution. At lower ionic strengths, the kinetic energy associated with Brownian motion is higher than the secondary minimum depth and can detach particles trapped in the secondary minimum.

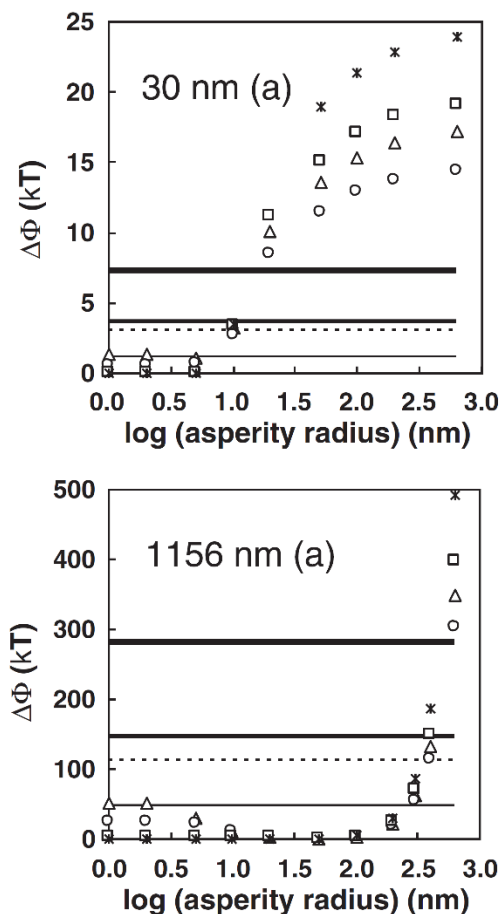


**Figure 2.10:** Variation of detachment energy barrier ( $\Delta\Phi$ ) for particles of diameter=30 nm (top) and 1156 nm (bottom) with asperity radius and ionic strength: asterisk= 0.001 M, square=0.01 M, sphere=0.1 M, triangle=0.2 M. The detachment energy barriers for particle-smooth plate are shown at different ionic strengths as bolder solid line for 0.001 M, bold solid line for 0.01 M, solid line for 0.1 M and dashed line for 0.2 M. (with permission from [136]).

Generally, since the point of contact between particles and surfaces is moved away from the base surface to the asperity top, the depth of the attachment energy minimum of the particle to a rough surface is smaller (weaker) compared to a smooth surface with similar chemical composition [86]. This means that for a rough surface it would be easier to detach the particles from the surface, as compared to an equivalent smooth surface. However, similar to the particle attachment, the detachment energy minimum depth goes through a critical value with an increase in asperity size, for the same reason discussed for the attachment probability (**Figure 2.3**).

#### 2.4.6 Summary of particles interacting with rough surfaces

Based on the above discussion, for unfavourable membrane surface attachment conditions, the existence of nanometer-size asperities is expected to smear the interaction energy barrier and lead to more particle adhesion. Additionally, based on the above discussions, these membrane surfaces can be cleaned more readily as compared to smooth membranes. All of the discussions made in

this section were based on simplifying assumptions of homogeneous chemistry of the surface. In the following section, the effect of chemical heterogeneities will be discussed on the surface interactions between smooth flat surfaces and spherical particles.

## 2.5 Surface interactions between a chemically heterogeneous smooth flat surface and spherical colloidal particles (Case 3)

### 2.5.1 Chemical heterogeneities on MD membrane surfaces

In **Section 2.3**, the effects of surface chemistry were discussed on the interactions between flat surfaces and spherical particles, where the interacting surfaces are assumed to be chemically homogeneous, meaning that their surface properties do not vary significantly over their entire surface. However, a truly chemically homogeneous surface with a uniform type and intensity of surface interactions is rarely the case in synthetically engineered membranes, e.g., MD membranes. As mentioned in **Section 2.2**, the membrane surface that interacts with the colloidal particles, consists of a combination of air (or vapour)-liquid as well as solid-liquid interfaces. The air-water interface is a hydrophobic surface and exists on all MD membranes in the form of the water meniscus at the pores (with a length scale of 200-1000 nm) and/or in the nonwetted portion of rough surfaces in Cassie-Baxter state (with a length scale of a few to hundreds of nanometers). Additionally, the solid-water interfaces of the membrane may contain various chemical groups which endow certain properties to these interfaces. The chemical heterogeneities on the solid-water interfaces of superhydrophobic and omniphobic membranes could originate from the materials constituting the asperities which are usually inorganic particles, and the hydrophobic coating materials [24]. The fluoroalkane-based hydrophobic coatings usually employed to coat the surface of these membranes may have defects due to incomplete coating, leaving patches of the substrate material exposed to the solution. The solid-water interface of Janus membranes can become heterogeneous due to the addition of hydrophobic chemicals such as perfluorooctanoate to the coating layer [7]. Additionally, in these membranes, depending on the coating method [25, 26, 137], the hydrophilic top layer might not completely cover the hydrophobic substrate, leaving patches of hydrophobic surface on an otherwise hydrophilic surface. The air-water interface in Janus membranes is usually limited to the pores. Depending on the structure of the substrate, this interface may protrude into the substrate or may only exist directly on the side of the hydrophilic coating layer facing the hydrophobic substrate.

According to the above discussion, most MD membranes contain chemical surface heterogeneities that can affect their surface interactions with colloidal particles. Therefore, understanding the effect of chemical heterogeneities on the surface interactions between the membrane and colloids is important in understanding the effectiveness of various methods for the fabrication of membranes with better resistance against the colloidal adhesion. In this section, we

will focus on the interactions between smooth but chemically heterogeneous membrane surfaces and spherical colloidal particles. Additionally, most of the examples discussed in this section will be focused on DLVO forces, while generalization to other forces will be made qualitatively where applicable. The more complex systems consisted of the combination of physical and chemical heterogeneities will be discussed in the next section extending the discussed theories to MD membranes.

### 2.5.2 Definition and theory of heterogeneous surfaces

Here, for simplicity, we will assume that the chemical heterogeneities form separate microdomains on the surface of the membrane. These microdomains will be referred to as patches, and the ratio of the surface area of these patches to that of the entire surface will be referred to as the patch density.

The macroscopic (mean-field) theories of surface interactions introduced in **Section 2.3** rely on the averaging of the properties of the chemical species on surfaces. This approach can successfully explain the interactions between chemically homogeneous surfaces. However, for chemically heterogeneous surfaces, the local fluctuations in the chemical composition of the surfaces can change the way the membrane surface interacts with the foulants. These fluctuations are not accounted for in the mean-field models that consider the surface to be homogeneous. For instance, let us consider a negatively charged flat surface covered with a small fraction of positively charged patches in a way that the net surface charge is still negative. According to the mean field approach, the interactions between this surface and a negatively charged spherical foulant would be no different from what it would be expected if the surface was homogeneous and negatively charged (with the charge equal to the net charge of the patchy surface). However, in practice, under certain conditions, the particles can adhere to the chemically heterogeneous surface. This phenomenon cannot be explained using the mean-field approach. For addressing this problem, individual contributions from the patches and the substrate should be accounted for in a local level for analyzing the surface interactions. In a local level, only a limited region on the membrane makes most of the contribution to the particle-membrane interaction forces. As the particle approaches the surface, this area becomes larger until it reaches a limit determined by the particle size and the Debye length (for EDL interactions). This area is often referred to as electrostatic zone of influence (ZOI) [138]. There are two widely-used approaches to define the ZOI which are shown in **Figure 2.11** [138]. In the first approach, the ZOI is defined by intersecting the Debye shell of the particle with the plate surface. In the second approach, ZOI is defined by intersecting the two Debye shells related to the particle and the plate. The radius of the ZOI obtained through both methods is proportional to  $\sqrt{R_p \kappa^{-1}}$ , in which  $R_p$  is the radius of the particle and  $\kappa^{-1}$  is the



Debye length of the solution. The values of this parameter are only slightly different due to the difference in their prefactor (prefactor of 2 for first method and  $\sqrt{2}$  for the second method).

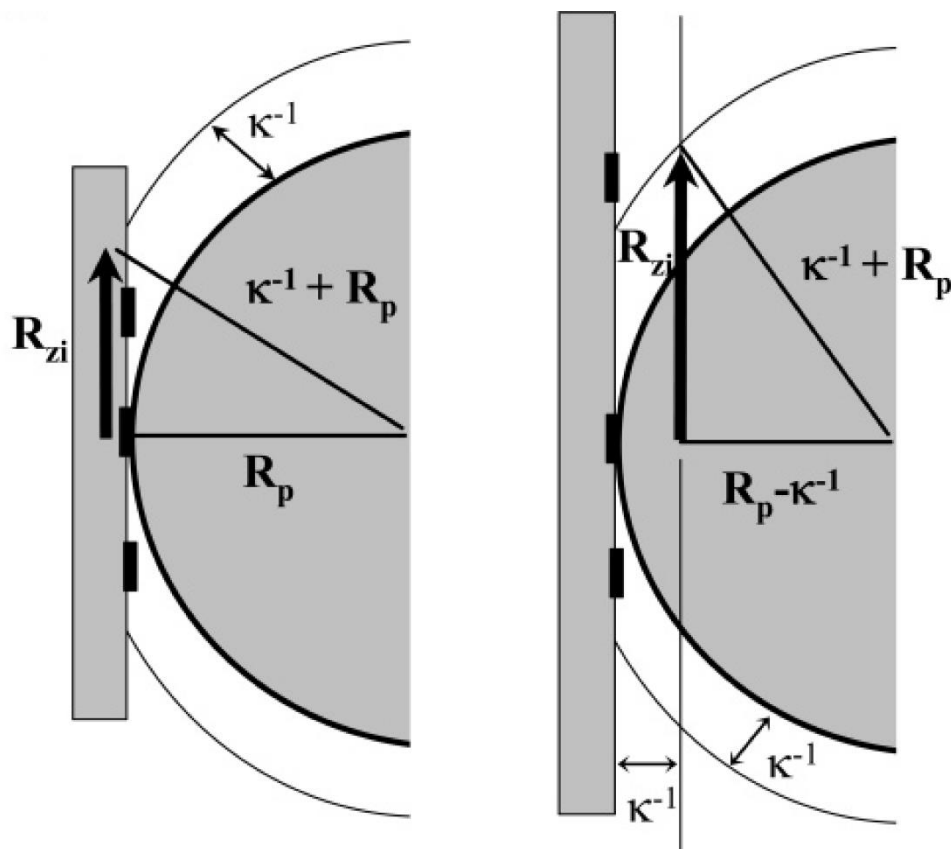


**Figure 2.11:** Different definitions of zone of influence (ZOI) and its radius,  $R_{zi}$ . A sphere with the radius of  $R_p$  is in contact with a patchy planar surface.  $\kappa^{-1}$  is Debye length of the solution. In the definition shown on the left,  $R_{zi}$  can be calculated using Pythagoras' theorem  $R_{zi}^2 + R_p^2 = (R_p + \kappa^{-1})^2$ . Alternatively, in the definition shown in on the right, the  $R_{zi}$  is the radius of the zone resulting from the intersection of the plane at the distance of one Debye length from the surface, and the volume of the “particle+particle Debye length”. Similar to the other definition,  $R_{zi}$  can be calculated for this definition using:  $R_{zi}^2 + (R_p - \kappa^{-1})^2 = (R_p + \kappa^{-1})^2$  (with permission from [138]).

### 2.5.3 Importance of ZOI in understanding heterogeneous surface interactions

The effect of particle size on its interactions with chemically heterogeneous surfaces can be explained using the concept of ZOI. For instance, Santore and Kozlova [138] investigated the effect of particle size and patch density on particle adhesion to chemically heterogeneous surfaces with a constant patch size. The base surface in their study consisted of silica (with an electrokinetic charge of  $-0.08/\text{nm}^2$ ), and the patches were created using poly(dimethyl aminoethyl methacrylate) (pDMAEMA) which is a cationic polyelectrolyte (with a coil size of ca. 11 nm and patch electrokinetic charge of  $+0.08/\text{nm}^2$ ). Two different sizes of negatively charged silica particles (460 and 1000 nm) were used in this study. They found that smaller particles had a lower



threshold patch density for adhesion, and attributed this phenomenon to be the effect of a small ZOI for smaller particles. A decrease in the size of the ZOI increases the relative size of the patch (which is constant in this case) to that of ZOI. This leads to a higher fluctuation effect of the patches in ZOI, making it more likely for the particles to adhere to the surface. This result is important in dealing with the particles of any shape, because the curvature of the particle determines the size of the ZOI, which in turn determines the likelihood of the particle adhesion. In other words, a higher curvature (smaller diameter) can lead to adhesion at lower patch densities. This is an important conclusion considering the interactions between MD membranes and colloidal particles. A possible effective strategy against colloidal adhesion would be to make sure that the chemically favourable patches are as small as possible; while the particles are as large as possible. Increase in the  $IS$  leads to the reduction of the Debye length which in turn results in the reduction in the size of ZOI. Therefore, the ratio of the patch size to the size of the ZOI increases, and the particle adhesion is influenced by the fluctuations in surface chemistry at a lower patch density [138].

The concept of ZOI is especially important in understanding the surface properties of chemically heterogeneous surfaces, because it explains the fluctuations in the interaction force that occur relative to the averaged force [138, 139]. These fluctuations are determined by the relative size of the patches to that of the ZOI.

For the systems with a patch size lower than the size of the ZOI, a decrease in the average distance between the patches (corresponding to an increase in the patch density) leads to an increased likelihood of particle adhesion [138, 139]. This phenomenon is attributed to the increased fluctuations of the surface interaction forces within the ZOI that can lead to particle adhesion despite the fact that the average surface charge of the flat surface has the same sign as the particles [138, 139]. Conversely, in these systems, with an increase in the distance between the patches (corresponding to a decrease in the patch density), the surface interaction forces experienced by the particles approaches the interaction forces that the particles would experience from a flat surface with the average surface properties of the patches and the base flat surface. Therefore, in this case, the behaviour is similar to the prediction of the mean-field approaches and the likelihood of particle adhesion is determined by the average properties of the flat surface [138, 139].

If the patches are large enough compared to the ZOI, or if the patch size is much larger than the ZOI, the surface interactions between the particle and the membrane are dominated more by the favourable patches, making it more likely for the particles to adhere to the membrane surface [140, 141]. The particles located directly above the patches only experience the surface interactions from the patch. Therefore, an apparently straightforward approach in studying these systems would be to calculate the interaction of the particle with the patch separately to obtain

the rate of deposition over that patch. The total deposition rate can then be obtained by simply summing the deposition rates on all patches. This model is known as the patchwise model, and was often used in calculating the deposition rate on chemically heterogeneous surfaces [141]. However, as will be discussed later in this section, this model was found to produce large errors because it does not take into account the simultaneous contribution from both patches and the substrate on the surface interactions with the particles [140, 141]. These effects usually influence the interactions due to the hydrodynamic motion of the particles [140, 141].

#### 2.5.4 Hydrodynamic considerations in particle deposition on chemically heterogeneous surfaces

The attachment of the particles to a chemically heterogeneous surface is also influenced by the hydrodynamics of the system. Duffadar and Davis [124] studied the interactions between negatively-charged spherical particles (diameter=1  $\mu\text{m}$ , surface potential = -27 mV) and chemically heterogeneous surfaces comprised of a negatively-charged base surface (surface potential = -27 mV) which was covered with randomly-distributed positively charged circular heterogeneities (diameter=11 nm, surface potential = +54 mV). They also considered the hydrodynamic effects in their calculations. Different patch densities (0.05, 0.1, and 0.16) were studied to investigate the effect of this factor on the surface interactions and particle deposition. In their research, the ZOI is defined as the area on the flat surface which makes at least 1% contribution to the total EDL interactions between the flat surface and the particle surface. This area varies with the changes in the distance between the particle and the surface. The particle trajectories obtained by Duffadar and Davis are shown in **Figure 2.12**. As shown in this figure, the particle follows different trajectories at each patch density, moving closer to the surface with an increase in patch density. The average path of each of these trajectories is dictated by the mean-field interactions between the particle and the patchy surface (dotted lines in **Figure 2.12**). However, with an increase in patch density, the fluctuations in the trajectory becomes more pronounced due to the fluctuations in the DLVO interaction force between particle and the flat surface caused by the attractive patches. As the patch density increased from 0.05 to 0.16, the fluctuations in the trajectory led to the adhesion of particles to the surface after traversing for a distance over the surface, even though the average charge of the flat surface was still negative. With an increase in patch density, the total area of the patches inside the ZOI become comparable to the area of the ZOI. This allows for the particle to move parallel to the surface at closer distance due to the reduction in repulsion. Additionally, the presence of the higher density of favourable patches inside the ZOI leads to more significant fluctuations in the interaction forces which can create fluctuations in the particle trajectory. These fluctuations at the close distance from the flat surface can eventually lead to the adhesion of the particle to the surface despite the average negative charge of the surface.

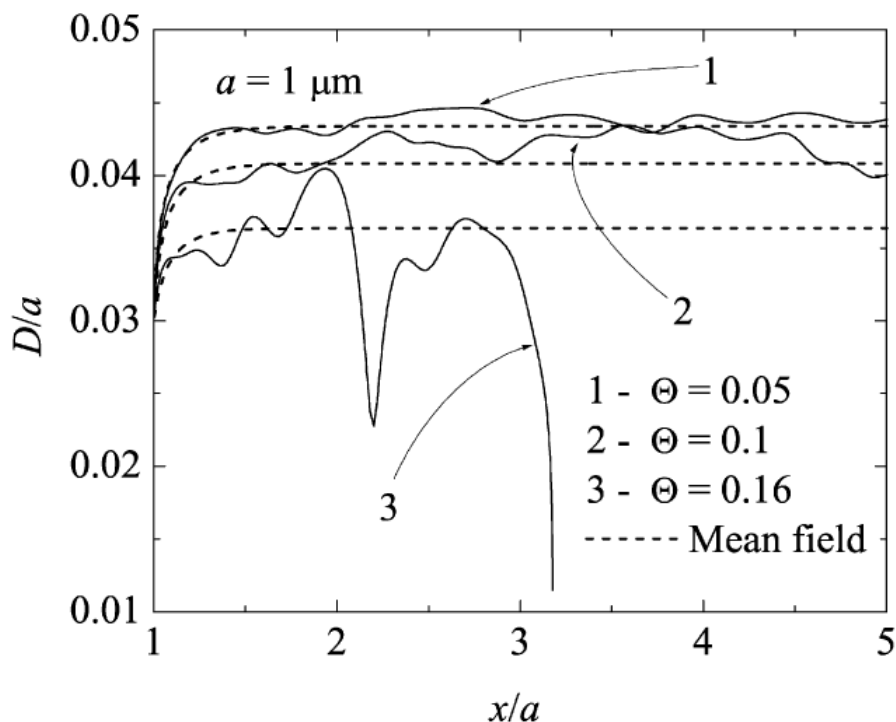


**Figure 2.12:** Trajectory of  $1 \mu\text{m}$  particles over a chemically heterogeneous flat surface with different patch densities ( $\Theta$ ) (with permission from [124]).

The effect of shear rate on particle deposition is complex due to the interplay between surface interactions and hydrodynamic effects. For instance, Kalasin and Santore [142] studied the effect of shear rate on the particle deposition on a base unfavourable surface with favourable patches at different patch surface fractions. The base surface consisted of silica (with an electrokinetic charge of  $-0.08/\text{nm}^2$ ), and the patches were created using poly(dimethyl aminoethyl methacrylate) (pDMAEMA) which is a cationic polyelectrolyte (with a coil size of ca. 11 nm and patch electrokinetic charge of  $+0.08/\text{nm}^2$ ). Negatively charged silica particles with a diameter of  $1 \mu\text{m}$  were used in this study. It was found that an increase in shear rate can lead to more particle deposition if the shear rate is strong enough to carry the particles toward the surface but not strong enough to detach them. Beyond a certain shear rate, particle deposition is decreased due to the ability of the shear force to detach the particles. They also found that at low shear rates, the threshold patch density for adhesion is lower than that at higher shear rates. Therefore, in terms of patch density, they found two regimes for particle adhesion kinetics: 1. the surface-controlled regime which takes place at low patch densities. In this regime, an increase in shear rate leads to a better detachment of particles and their prevention from adhering to the surface. 2. The hydrodynamics-controlled regime, in which the particle adhesion rate increases with shear rate due to a higher mass transfer from the solution bulk to the surface. It is worth mentioning that this study was performed at the dilute limit, and only the first stage of adsorption was accounted for

to avoid the effect of adsorbed particles on the new particles being adsorbed on the surface (as opposed to sequential adsorption models). The adhesion threshold patch density was also found to decrease with ionic strength. Additionally, at a constant IS, with an increase in shear rate, the adhesion threshold increased.

The decrease in deposition flux with an increase in shear rate is referred to as hydrodynamic bump effect by Elimelech et al [140]. In their research, they evaluated particle deposition on chemically heterogeneous surfaces under different flow conditions. Monodisperse positively charged latex particles were used with the diameter of  $2.1 \mu\text{m}$  and a zeta potential ranging between 41.2-71.6 mV at different ionic strengths of  $10^{-3.5}$ ,  $10^{-3.0}$ , and  $10^{-2.5}$  M of KCl, respectively. The collector plates used in this study were glass slides surface-modified by soft lithography to create stripes of  $5 \mu\text{m}$  of positively charged amine functionalized regions adjacent to  $5 \mu\text{m}$  nonfunctionalized negatively-charged glass stripes (patch density of 50%). For generating different flow conditions, the researchers varied the flow velocity of the impinging flow which was perpendicular to the flat patchy surface. They studied the deposition rate as a function of particle Péclet number ( $Pe$ ) which is that ratio of the advective motion of the particle to its diffusive motion ( $Pe = \frac{2Ru}{D}$  where  $R$ ,  $u$ , and  $D$  are the radius, velocity, and the diffusivity of the particle in the medium, respectively). It was found that at low Péclet numbers, the deposition rate was similar to the value predicted by the patchwise model [140]. However, at higher Péclet numbers, the experimentally obtained deposition rate decreased relative to the patchwise model. The authors attributed the observed results to the hydrodynamic bump effect (shown in **Figure 2.13**) that the particles experience due to the repulsive interactions with adjacent repulsive patches [140]. With an increase in Péclet number, the particles experience the hydrodynamic bump from the unfavourable patches more severely which prevents them from attaching to the adjacent favourable patches. This is an important result, because it shows the significance of the interplay between different factors that can be used in order to minimize fouling in MD.

By increasing the flow velocity, it is possible to enhance the adhesion resistance of a chemically heterogeneous system even though it might contain favourable patches, provided that the hydrodynamic bump effect is large enough. One way to enforce this condition is to design the size of the surface unfavourable heterogeneous spots comparable to or larger than the particle size. With an increase in ionic strength, the deposition flux was found to go through a maximum which can be explained in terms of hydrodynamic bump effect. The increase in ionic strength decreases the Debye length which leads to a decrease in ZOI. The decrease in ZOI reduces the effective region with which the particle interacts. Therefore, the particles approaching the favourable patches do not experience the repulsive force from the adjacent unfavourable patches. Therefore, with an increase in the advective flux of the particles, they can adhere to the surface

easier. An increase in the flow velocity beyond a critical point leads to a better detachment of the particles from the favourable patches, as well as the more severe exposure of the particles to the adjacent unfavourable patches. The trajectory of the particles rejected by the unfavourable patches at higher flow velocities cannot easily change (toward the surface) to adhere to the favourable patches.

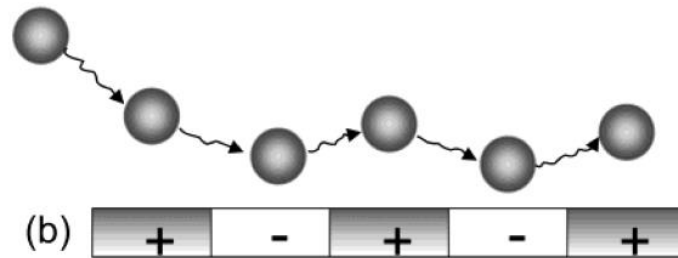


**Figure 2.13:** Schematic presentation of hydrodynamic bump effect (with permission from [140]).

The hydrodynamic bump can also lead to a higher deposition flux for the heterogeneous surfaces with a patch size larger than the particle size (or more accurately, the ZOI). The rejection of the particles from the adjacent unfavourable patches can create a high local concentration of the particles at the edge of the favourable patch leading to an enhanced deposition rate on the favourable patch [141, 143]. This deposition rate was found to be higher than an equivalent homogeneous favourable patch with the same properties [141, 143]. For instance, particle deposition flux was studied by Nazemifard et al. [141] on a circular chemically heterogeneous disk with radially concentric stripes of different charges using finite element method. In their model system, the liquid entered the collector channel perpendicular to the centre of the disk and flowed radially toward the perimeter of the disk. The radius of the particles was varied from  $0.1 \mu\text{m}$  to  $2 \mu\text{m}$  and they were negatively charged. The radius of each favourable and unfavourable areas was varied to obtain different coverage ratios from 0-100%. The sum of the length of favourable and unfavourable stripes varied from  $4 \mu\text{m}$  to  $20 \mu\text{m}$ . They found that the deposition rate is much higher on a surface with favourable patches, compared to an equivalent homogeneous surface with the same net charge (**Figure 2.14**). It was also found that the deposition rate has a nonlinear dependence on the patch density with a positive deviation from the patchwise heterogeneity model. A small fraction of favourable patches on an unfavourable surface significantly enhanced particle deposition, while the opposite was not true for unfavourable patches on a favourable surface. In other words, the deposition of the particles on a favourable surface was not disrupted significantly in presence of unfavourable patches. Additionally, the deposition flux increased with the patch density to a point that it became comparable (within 10%) with a fully favourable surface at 50% patch density. It should also be mentioned that a peak in

deposition rate was observed at the edge of each favourable patch which could be related to the repulsion of the particles from the adjacent unfavourable patches in the radial direction.

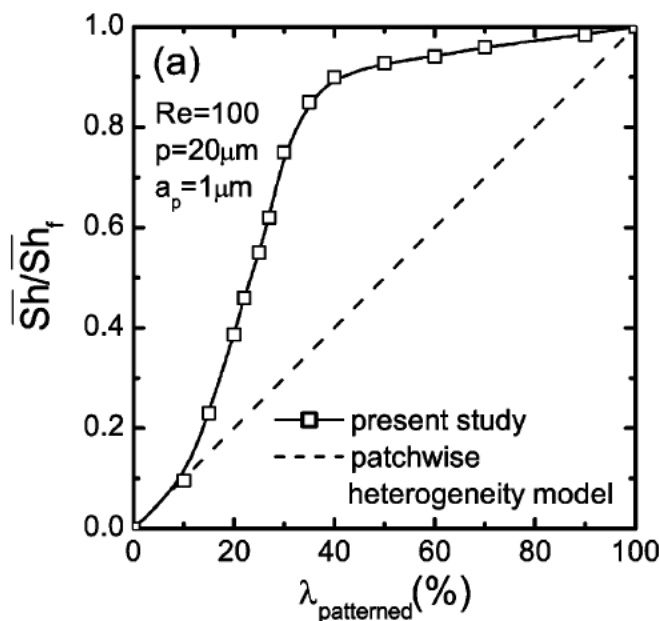


**Figure 2.14:** Deposition flux of negatively charged particles with a radius of  $1 \mu m$  on positively charged stripes with a width of  $20 \mu m$  (with permission from [141]).

Based on the above discussions, hydrodynamics can influence the attachment of particles on chemically heterogeneous surfaces. The trajectory of the particles moving over the surface can be affected by the presence of favourable patches on otherwise unfavourable flat surfaces. This can lead to particle deposition on the favourable patches regardless of the net surface charge of the flat surface. It was also found the unfavourable patches on an otherwise favourable flat surface can act as bumps repelling and preventing the particles from adhering to the favourable base surface due to the hydrodynamic bump effect. These results can further be employed in designing MD membranes with enhanced resistance against colloidal adhesion as described in **Section 2.6**.

### 2.5.5 Effect of frictional forces on attachment and detachment of particles on surfaces

Apart from hydrodynamic effects, the frictional forces between the particles and the membrane surface can affect whether the particles would remain stationary on the surface or will move on the surface due to the shear flow. This can be important regarding MD, because the particles might initially be trapped in one patch and roll over the surface and accumulate in certain regions such as the water meniscus inside the pores, forming aggregates and blocking the pores. In this regard, Duffadar and Davis [144] investigated the effect of frictional forces alongside hydrodynamic and surface forces in the deposition of spherical colloids on chemically heterogeneous surfaces consisted of favourable patches over an unfavourable substrate. Their particle trajectory results show that the particles undergo various different scenarios depending on the ionic strength, shear

rate, and particle-wall distances. For example, they observed a skipping motion by which the particle adheres to the surface for some distance and then detaches from the surface and continues its previous trajectory before attaching to the surface again. They have plotted adhesion phase diagrams (**Figure 2.15**) to indicate the conditions that lead to particle adhesion and rolling. It was found that with an increase in shear rate the arresting motion was completely eliminated. However, the particles would roll and skip over the surface provided that the adhesion force is high enough (e.g., high patch density and low ionic strength).

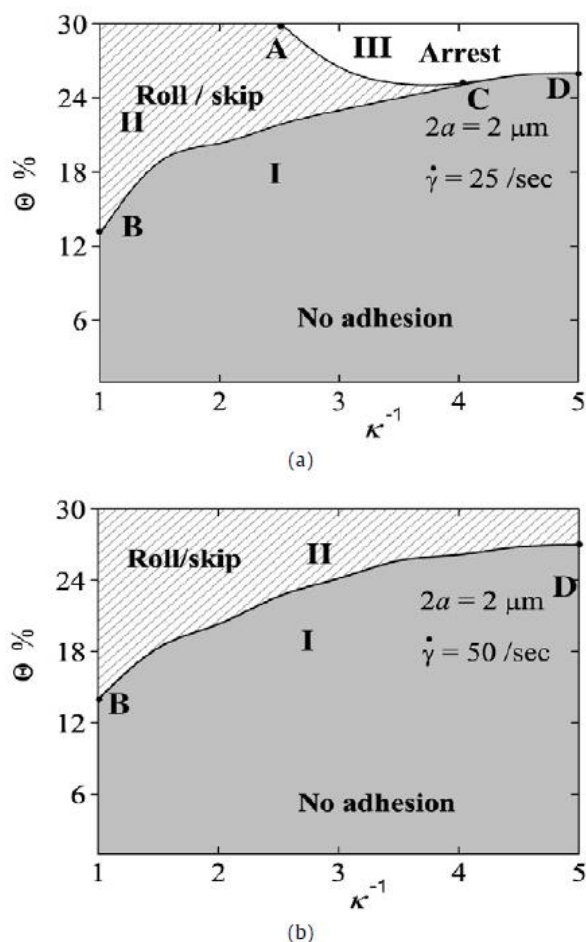


**Figure 2.15:** Adhesion phase diagrams by Duffadar and Davis as a function of patch density,  $\Theta$ , and Debye length ( $\kappa^{-1}$ ) (in  $\text{nm}$ ) for negatively charged particles with a radius of  $1 \mu\text{m}$  over a chemically heterogeneous surface at: a) shear rate of  $25/\text{s}$ , and b) shear rate of  $50/\text{s}$  (with permission from [144]).

### 2.5.6 Summary of surface interactions on chemically heterogeneous surfaces and relevance to MD membranes

Based on the above discussions, the surface interactions between colloidal particles and membranes can be affected significantly by the presence of chemical heterogeneities on the membranes. The particle adhesion in this case depends on the relative size of the ZOI of the

particle to the size of the favourable patches as well as the hydrodynamic flow characteristics of the particles over the membrane surface. In addition, the total surface charge of the membrane in these cases might not be a reliable parameter in evaluating whether or not the particles are likely to adhere to the membrane. Local particle adhesion can occur on favourable patches on the membrane surface while the overall surface charge of the membrane has the same sign as the particles. In MD membranes, the chemically heterogeneous surface is usually not smooth and the attractive patches can either be at a lower or a higher elevation from the base repulsive surfaces. Therefore, the combined effect of the roughness (topography) and chemical heterogeneities will be discussed in the context of DLVO theory in the next section.

## 2.6 Combined effect of topography and chemistry on the surface interactions between MD membranes and colloidal particles (Case 4)

The effects of physical and chemical heterogeneities on surface interactions were discussed individually in previous sections. A combination of these effects determine the interactions between colloidal particles and membrane surfaces in MD. Therefore, this combined effect and its implications on colloidal adhesion in MD will be discussed in this section.

As it was discussed in the previous section, the patch density and the relative size of the particle electrical ZOI to that of the favourable patches can determine the adhesion probability of the particle to this surface. It was also discussed that at low patch densities and patch size/ZOI ratios, the probability of adhesion is low and the interactions are dominated by the average properties of the surface. Here, assuming that the favourable patches are located in an elevated position with respect to the base surface, they create asperities with favourable attachment conditions. Conversely, as it was discussed in **Section 2.4**, the presence of the asperity moves the point of contact between the membrane and the particle to a new position, and depending on the relative size of the asperity and the particle ZOI, the particle can interact only with the asperity or with both asperity and the base surface [145, 146].

If the particle ZOI is larger than the asperity height, the particle-membrane interactions is mainly influenced by the repulsion exerted by the base surface and the attraction imposed by the asperities. However, due the elevated position of the favourable patches, the effect of the base surface in repelling the particles becomes weaker compared to an equivalent smooth surface with the same patch size [145, 146]. Therefore, if the interaction energy between the smooth patchy surface and the particle has an energy barrier due the repulsion from the unfavourable base surface, this energy barrier can become weaker for a rough surface in which the asperities are favourable.

If the ZOI is small in comparison to the asperity height, the particle mainly interacts with the asperity, while the contribution of the underlying base surface to this interaction is negligible.



Therefore, since the asperity is favourable for attachment, the particle can attach to the asperity regardless of the negative charge (unfavourable) of the base surface. Therefore, when the favourable patches are at an elevated position with respect to the unfavourable base, they can attract colloidal particles significantly more than when they are on the same level with the unfavourable base surface, because the particles are no longer repelled by the unfavourable base surface.

With an increase in the asperity height, the zone of influence of the particle has less overlap with the base surface, and with an increase in asperity height at some point the particle starts to solely interact with the asperity instead of the substrate. As a result, the attraction between the particle and the asperity can lead to enhanced particle adhesion. In cases that the particle ZOI is large as compared to the asperity height, the particle is affected by both asperity and the base surface.

## 2.7 Manifestation of surface interactions in MD membranes and rational design of adhesion-resistant membranes

As discussed in **Section 2.2**, the interfaces that participate in the membrane-colloid interactions in MD consist of various portions of solid-liquid and air (vapour)-liquid interfaces (**Figure 2.1**). The combined effect of this composite interface depends on the surface properties of its constituent elements, as well as its topographical characteristics such as surface density, position, and size.

### 2.7.1 Asperities in MD membranes

The solid-liquid interface in the MD membranes is usually negatively charged and the properties of this interface is controlled by the portion of the solid surface that is directly in contact with the feed liquid in either Cassie-Baxter or Wenzel regimes. For hydrophobic, superhydrophobic, and omniphobic membranes, the solid-liquid portion of the interfaces is usually rough and its interactions with colloidal particles follows the same principles discussed in **Section 2.4**. Based on the discussions of **Section 2.4**, for preparing a good adhesion-resistant MD membrane, particle attachment and detachment should be considered simultaneously. Below the critical asperity size, with an increase in asperity size, the energy barrier against particle attachment is suppressed, leading to more severe particle adhesion. However, the particle adhesion in this case is largely reversible and the original properties of the membranes can be retained more readily as compare to an equivalent smooth surface. Above the critical asperity radius, the energy barrier against particle attachment becomes larger, leading to a less severe fouling. However, the particles attached to the membrane surface are less likely to be removed upon exposure to low-salinity solutions, as compared to the case with asperities smaller than the critical radius. Therefore, finding the optimum asperity size depends on the trade-off between a high rate of reversible particle attachment at low asperity size against a low rate of irreversible particle attachment at

high asperity size. To mitigate irreversible fouling at high asperity size, the asperities can be designed to carry more negative charges. This way, the probability of attachment to the primary minimum decreases significantly.

The value of the critical asperity radius is not fixed for a given asperity-particle system, and changes with changes in the solution ionic strength. Therefore, the choice of a reference value for ionic strength would be necessary for calculating the relevant critical asperity radius. The most severe irreversible adhesion occurs at low solution IS, because the depth of the primary minimum is the highest (**Section 2.4**). Therefore, as a rule of thumb, the original feed ionic strength can be used as the reference, because it is lower than what the membrane actually experiences during the MD process (due to increase in concentration). The critical asperity radius obtained this way is the highest bound for this parameter. In addition to the above, calculation of the critical asperity radius and employing fabrication techniques that can produce the asperities with controlled size are among the challenges that need to be tackled in engineering adhesion-resistant MD membranes.

### 2.7.2 Chemical patches in MD membranes

The length scale of the chemical patches is an important factor to consider in designing MD membranes. As discussed in **Section 2.5**, the chemical heterogeneities on membrane surfaces exist in forms of solid-liquid and air-liquid interfaces. The length-scale of these chemical heterogeneities can range from a few to hundreds of nanometers depending on the type of the membranes and the method used to fabricate or modify their surface [24, 130].

The air-water interfaces in hydrophobic, superhydrophobic, and omniphobic membranes are located on the nonwetted portion of the rough surfaces (in Cassie-Baxter state) and on the pore entrances. In Janus (hydrophilic-hydrophobic) membranes, these interfaces are usually located on the pore entrances. Air-water interfaces can act as hydrophobic patches in MD membranes. Hydrophobic interactions are different from EDL interactions in the intensity and the nature and their effective range can exceed tens of nanometers [86]. Increasing the total area of favourable interfaces such as air-water interfaces beyond a certain point can increase the adhesion and entrapment of hydrophobic colloidal particles on these surfaces. It is a common practice in hydrophobic, superhydrophobic, and omniphobic membranes to attempt and make the membrane surface as hydrophobic as possible to ensure a Cassie-Baxter state [24, 130]. However, there is no research focusing on whether this increase in the total hydrophobic patches (air-water interfaces) can exacerbate the colloidal adhesion in MD. The local contribution of the hydrophobic forces from the air-water interfaces can lead to the adsorption of hydrophobic particles onto these interfaces. According to the discussions of **Section 2.5**, in a constant patch density, a surface with smaller favourable patches have a lower rate of particle deposition.

Therefore, for creating a membrane surface with lower likelihood for the adhesion of hydrophobic particles, membranes with smaller surface pores (pores at the surface of the membrane exposed to the solution) but instead increased number density of pores would be more favourable.

Another type of attractive patches are the areas on the surface resulting from surface treatments which use alternatively positively and negatively charged chemicals. The patchy surface is created in this case due to the incomplete coverage of the underlying substrate with the top layer. This is unavoidable in practice. However, the use of other alternative methods that do not involve positively charged intermediate surfaces might be helpful in avoiding such attractive patches.

Apart from attractive patches, the effect of repulsive patches should also be considered in the design of adhesion resistant membranes. For instance, these patches can be created in omniphobic and superhydrophobic membranes due to the application of metal oxides or silica nanoparticles in creating the re-entrant structure [24, 130]. These surfaces usually have a negative surface charge which can repel negatively-charged foulants. In addition, the shape of these particles also plays an important role in resisting the adhesion of negatively charged colloidal particles.

The fact that each interaction type between colloidal particles and membrane surfaces can have a different intensity can be utilized as an advantage in membrane design. For a given type of membrane surface, the membrane engineer has a plethora of options for selecting the materials that can act as repellents for certain foulants. Addition of these repellent materials to the membrane surface can significantly improve its adhesion-resistance properties.

### 2.7.3 Importance of underwater oil wetting resistance of MD membranes

For the oils, apart from their surface interactions with the membrane, underwater wettability of the membrane by oil droplets is another important characteristic in determining the resistance of membranes against oil adhesion and wetting [8, 25]. Therefore, the membranes showing a high underwater oil contact-angle (underwater oleophobic surfaces) are favorable in the treatment of oily waters. While underwater oil repellence is observed in omniphobic membranes only under special circumstances [7, 147-149], Janus membranes are usually highly oleophobic underwater [8, 25]. This property is imparted on Janus membranes by their hydrophilic top layer that can maintain a hydration layer acting as a barrier against the adhesion and spreading of oil droplets on its surface [25]. However, the stability of the hydrophilic top layer remains to be a challenge in Janus membranes because of its poor integration with the hydrophobic substrate [25, 26]. In this regard, surface grafting methods are gaining increasing attention for fabricating Janus membranes [32]. In these methods, typically, a hydrophilic polymer is covalently tethered to the hydrophobic substrate, creating more stable membrane as compared to those in which the binding takes place due to hydrophobic or electrostatic interactions.

#### 2.7.4 Polyelectrolytes and their stimuli-responsive behaviour in the design of oil resistant MD membranes

Surface grafted polyelectrolyte brushes are among the materials that have been used to form adhesion-resistant surfaces due to their electrostatic charge and ability to maintain a hydration layer in their vicinity [150]. Due to the ionic nature of polyelectrolyte brushes, their surface properties can be tuned by adjusting the pH and ionic strength of the solution. Weak anionic (acidic) polyelectrolytes become more underwater oleophobic with increasing pH [151, 152]; while the opposite is often found with weak cationic (basic) polyelectrolytes [150]. For both anionic and cationic brushes, with an increased ionic strength, the brush thickness goes through a maximum [151]. Changes in the brush thickness can be explained in terms of electrostatic interactions, osmotic pressure, and steric repulsions. At low salt concentrations (typically less than  $10^{-3}$  M), an increase in the salt concentration leads to an increase in charge density within the brushes due to the reduction in Debye length [151]. This phenomenon leads to the expansion of the brush and is referred to as the osmotic brush regime. With further increase in the salt concentration (typically above  $10^{-3}$  M, the electrostatic interactions within the brush decreases leading to its collapse, namely salted-brush regime [151]. The increase in the brush thickness due to salt concentration was found to be correlated to the increase in its underwater oleophobicity [150, 152-154]. Polyelectrolyte brushes are gaining an increased attention in creating fouling resistant self-cleaning membranes in UF [155, 156], NF [157], FO [158], and RO [40] applications. However, the application of these brushes is limited in MD [32].

#### 2.7.5 Grafting of polyelectrolytes using atom-transfer radical polymerization (ATRP)

Polyelectrolytes are usually grafted from their constituent monomers (grafting-from) onto different substrates using controlled radical polymerization methods such as atom-transfer radical polymerization (ATRP) to form well-defined polymer brushes [34, 159-161]. In addition, controlled radical polymerization methods such as ATRP usually require an oxygen-free atmosphere which limits their facile applicability in membrane modification. For employing ATRP on membranes, the surface grafting reactions need to be performed either inside deoxygenated reaction vessels that limits the size of the membrane coupons, or under a glove box which restricts the application of this method to the laboratories with access to this equipment [34]. Oxygen sensitivity in ATRP is attributed to the tendency of oxygen to react with the catalyst and hinder the propagation reaction, leading to a complete cessation of the polymerization [66]. New reaction schemes have been developed to tackle the problems related to deoxygenation in ATRP [68], which include the use of reducing agents as in activators regenerated by electron transfer (ARGET)-ATRP [162] and supplemental activator and reducing agent (SARA)-ATRP [67]. In addition, it was found that UV light can be employed to circumvent the oxygen-sensitivity of ATRP by regenerating the catalyst and can be used to control the reaction time, so that the

reaction can be performed under open atmosphere to create polymer brushes [66, 68, 163]. However, to the best of our knowledge, such UV-assisted ATRP technique has not yet been employed to graft polymer brushes onto membranes.

## 2.8 Application of electrochemical impedance spectroscopy (EIS) for *in-situ* fouling and wetting detection in MD

In the study of fouling in MD, the drop in flux is often used as an indication of fouling (or excessive particle adhesion), while wetting is detected by monitoring the electrical conductivity of the permeate solution. More advanced techniques have been employed to monitor fouling and wetting, which include optical coherence tomography (OCT) [164-167], and electrochemical impedance spectroscopy (EIS) [19, 69-75]. Among the mentioned methods, EIS is gaining increasing attention due to its versatility and sensitivity to the changes in the membrane properties. It is a powerful technique that has been applied for *in-situ* fouling studies in various membrane processes such as reverse osmosis (RO) [168-182], nanofiltration (NF) [183-186], ultrafiltration (UF) [187-199], microfiltration (MF) (together with UF), [200-206], and electrodialysis (ED) [200-206]. It has also been applied for *in-situ* wetting [19, 70-75] and fouling [69] studies in MD. EIS measurements are commonly performed by passing an AC current through the system and measuring the potential difference. Different parameters are then calculated as a function of frequency ( $f$ ), which can provide information on the changes taking place in the system. Below, two common methods for *in-situ* EIS measurements, namely the single frequency measurements and wide-frequency sweep will be discussed.

### 2.8.1 Single-frequency *in-situ* EIS measurements in wetting detection in MD

Wetting studies using EIS in MD have been performed predominantly using single-frequency measurements [19, 70-75]. In this method, the EIS measurement is performed at one frequency and the data acquisition is repeated by a predefined time-step during the MD process to monitor the changes in the system. The measurement frequency is commonly chosen in a way that it represents the properties of the physical element under study as reported by [19, 75]. In these studies, focussing on the membrane properties, the measurement frequency is chosen in the mid to high frequency range (10 kHz to 1 MHz) which is related to the ohmic resistance and capacitive behaviour of the system, so that the EIS data can be attributed to the membrane properties. Although this relationship can exist, the membrane properties are not the only parameters affecting the electrical properties of the system at any selected frequency. Other parameters such as electrical double layer (EDL) properties and permeate properties, that change during the MD process, can also affect the EIS data acquired at a single frequency. One approach to address this problem is to place the electrodes in direct contact with the membrane [19, 75]. Although this approach is effective in decreasing the effect of ohmic resistances of the feed and permeate

liquids, it still suffers from possible interferences from the interfaces between the solids (i.e., the membrane or the electrodes) and liquids (i.e., feed or permeate). Another approach to address this issue is to employ membranes with special design such as conductive membranes [69] or layer-by-layer membranes [70] to exclude the effects of permeate properties. These membranes with conductive surface layer have been designed to replace at least one of the electrodes [69, 70]. While this method is promising in terms of excluding the effects of permeate properties, the changes in the interfacial membrane properties on the feed side can still influence the obtained results. In addition, this approach limits the applicability of EIS to the membranes with special designs.

It can be concluded that single-frequency *in-situ* EIS measurements suffer from the limited information that they can provide on the changes in the impedance of the system during MD. This problem can be tackled using wide frequency sweep measurements discussed in the next section.

### 2.8.2 Wide-frequency sweep *in-situ* EIS measurements in wetting detection in MD

Another method for *in-situ* EIS measurements is wide-frequency-sweep sampling which has been applied more commonly in other membranes but also to a limited extent, in MD [69]. In this method, the EIS measurements are performed at a wide range of frequencies (5-6 orders of magnitude), and the frequency sweep is repeated multiple times during the MD process. This method provides more information (e.g., EDL effects and changes in permeate and feed salinity) on the behaviour of the system as compared to the single-frequency method. However, interpretation of the EIS results using this method depends on the equivalent circuit models proposed to analyse the data, and on how well these models can be applied to the system under study [69]. The complexity of the equivalent circuit model applied for the system requires detailed considerations to obtain reliable values for the circuit components (e.g., resistors and capacitors) representing the physical element of interest (e.g., the membrane). In all prior works, a holistic approach provided the needed information on the behaviour of the system by observing the trends in the EIS data and comparing them to the phenomena taking place in the system, which are monitored through traditional membrane process parameters, such as the permeate flux, solute rejection, etc., that are recorded simultaneously with the EIS data.

In conclusion, a wide-frequency sweep benefits from its ability to capture the behaviour of the system over a wide range of frequencies, providing insight on different properties of the system. However, this approach suffers from the complexities and errors associated with the equivalent circuit analysis. Considering the potential applications of MD in water reclamation from produced wastewater in various industries (e.g., shale oil and gas, food, and metal forming) [8], a dedicated EIS study with oily solutions on MD membranes is needed to shed further light on the fouling and wetting mechanisms in different water environment.

### 2.5. Conclusions and future directions:

In this chapter, to understand the oil adhesion resistance of MD membranes, the surface interactions between colloidal particles and MD membranes were investigated by reviewing the surface science literature.

For this purpose, first the interfaces of MD membranes that participate in surface interactions were identified for the three common membrane types, namely, (super)hydrophobic, omniphobic, and Janus membranes. The interfaces in these membranes can generally be broken down to two main components of air-water and solid water interfaces. The air-water interfaces form on the rough surfaces and pore entrances and solid water interfaces are formed between the membrane material and the feed solution at the points of direct contact with the feed water. Therefore, the MD membranes are usually consisted of rough surfaces in combination with chemical heterogeneities. To understand the underlying physics of the surface interactions for this complex system, different scenarios were first analysed separately, and were subsequently combined together to paint the full picture of the MD membranes.

In the next step of these analyses, the well-known DLVO theory as well as other theories were discussed for the interactions between smooth flat surfaces and spherical particles. It was found from the literature that parameters such as IS and surface potential (or charge) of the membrane and particle determine the attraction or repulsion between the membrane and the particles. In addition, the DLVO interaction energy between the smooth flat surface and the colloidal particle exhibits an energy barrier that prevents the adhesion of the particle to the flat surface.

Next, it was found that the addition of asperities (roughness features) onto the flat surface can affect the surface interactions depending on the relative size of the asperities and the particle. When the asperities are smaller than the particles, their presence decreases the height of the DLVO energy barrier leading to a high likelihood of particle adhesion. However, when the asperities are larger than the particles, the surface interactions depend on the location of the particles with respect to the asperities. The adhesion of the particles on rough surfaces are also affected by hydrodynamics of the systems, because the hydrodynamic motion of the solution can provide enough force to detach the particles from the surface and carry them over the asperities. Under the hydrodynamic flow of the solution, it was found that a closely-spaced in-line arrangement of the asperities favours the adhesion resistance by benefiting from the hydrodynamic flow of the particles over the asperities.

In the next step of this analysis, the effect of chemical heterogeneities was analysed on the surface interactions between a smooth flat surface and colloidal particles. Here the concept of ZOI was employed as an aid to understand the surface interactions between smooth patchy flat surfaces and colloidal particles. If the size of the favourable patches are smaller than the ZOI of the



particles, surface adhesion takes place at a higher patch density, because of a large contribution of the base surface in determining the surface interaction energy. However, if the size of the patches are larger than the particle ZOI, the particle is directly influenced by the favourable patch, and particle adhesion takes place more readily. Therefore, on an unfavourable surface with favourable patches the adhesion of the particles to favourable patches can take place even though the total surface has the same net surface potential (or charge) as the particles. Hydrodynamics were found to affect the surface interactions in this case by exposing the particles to the unfavourable patches creating a hydrodynamic bump effect that can repel the particles off the surface and prevent surface adhesion.

Next, the combined effect of topography and chemical heterogeneity was analysed in relation to MD membranes. It was conjectured that the portion of the membrane solid surfaces that are in direct contact with the feed solution play a crucial role in controlling the colloidal adhesion to these membranes. The roughness features that constitute this portion can determine whether the colloidal particle adheres to the solid surface of the membrane. In addition, it was conjectured that the air water interfaces present in MD membranes could act as attractive patches that trap hydrophobic particles and may play a role in pore blockage on the membranes.

Apart from the effects of surface interactions on oil adhesion, underwater oleophobicity was identified as another important factor in oil-resistant MD membranes. This property is related to a high resistance to the spreading of an oil droplet on the membrane while immersed underwater. Janus membranes were introduced as one of the membrane types with high underwater oleophobicity. However, the poor stability of the hydrophilic top layer in these membranes poses challenges in their long-term durability. Oxygen tolerant UV-assisted ATRP was introduced as possible solution to address this problem. In addition, the application of polyelectrolytes in creating oil resistant membranes was highlighted in this chapter.

Finally, the state of the art in the analysis of wetting and fouling using *in-situ* EIS measurements was reviewed and analysed. It was found that most of the studies in MD employed single-frequency measurements, while wide-frequency sweeps were rare in the literature. The single frequency measurements attributed the changes in the impedance at a selected frequency to the changes in the membrane properties, while the changes in other parameters such as the permeate and feed characteristics can also affect the impedance.



## Chapter 3 Materials and Methods

---

### 3.1 Materials

A commercial PVDF membranes Immobilon®-P<sup>SQ</sup>, (average pore size=0.2  $\mu\text{m}$ ) and Immobilon® (average pore size=0.45  $\mu\text{m}$ ) were purchased from Merck-Millipore (Darmstadt, Germany). Dodecane ( $\geq 99.9\%$ ), sodium acrylate (NaAA), NaOH, (3-Aminopropyl)triethoxysilane (APTES) (99%), Cu(II)Br<sub>2</sub> (99%), n-hexane (99%), 2,2'-bipyridyl (bipy), 2-Bromo-2-methylpropionic acid (BMPA), and  $\alpha$ -bromoisobutyryl bromide (BiBB) (98%) were purchased from Sigma-Aldrich (St. Louis, USA). Toluene (99.8%), and triethylamine (TEA) (99%) were purchased from ThermoFisher Scientific (Massachusetts, USA). All chemicals were used as received without further purification.

### 3.2 Characterizations

#### 3.2.1 Attenuated total reflectance Fourier transform infrared spectroscopy (ATR-FTIR)

The ATR-FTIR measurements of the as-prepared membranes were performed using a Perkin Elmer ATR-FTIR spectrometer (Perkin Elmer, Germany), in the wavenumber range of 600-4000  $\text{cm}^{-1}$ , and the data were averaged over 16 scans for each specimen.

#### 3.2.2 Contact-angle experiments

The contact-angle experiments of the membrane surfaces were performed using a drop shape analyzer (DSA25E, Krüss, Germany) and were analyzed using Advance software (Krüss, Germany). For in-air water contact angle experiments, the experiment was repeated at least 5 times at 5 different spots for each sample. The underwater oil contact angle tests were performed with dodecane under Milli-Q water and under saline solutions with salinities varying from 0.0010 M to 3.0 M NaCl. Due to the challenges in capturing the contact angle of the oil droplets under water, the dynamic process (i.e., the approach, contact, and retraction of the needle) capturing the attached oil droplet was recorded using the video recording function of the Advance software (Krüss, Germany). Screenshots were extracted from the recorded videos of each test at each stage of approach, contact, and retraction of the needle.

#### 3.2.3 Scanning electron microscopy (SEM) and energy dispersive X-ray (EDX) spectroscopy

SEM was performed using a Phenom II SEM (ThermoScientific, USA) equipped with a built-in EDX spectrometer. Dry membrane samples were gold-sputtered prior to the SEM image acquisition. The images were acquired from top surface of the samples at the magnification of 10,000x to 20,000x with the beam energy of 10 keV. EDX analysis was performed on three selected spots on top of the membranes as well as for three regions on the surface on each membrane.

### 3.2.4 Streaming potential analysis

Streaming potential analysis was performed using a Surpass electrokinetic analyzer (Anton Paar, Austria) in the pH range of 2.5 to 9.0 to obtain the surface zeta potential of the membranes. The electrolyte solution was 0.1 M NaCl and the pH was adjusted using HCl (0.1 M) and NaOH (0.1 M) solutions by the titration function of the instrument.

### 3.3 Method development for surface modifications

The aim of the surface modifications is to graft PAA onto membrane surfaces employing Oxygen-tolerant UV-assisted ATRP. The grafting reactions consisted of four main steps including OH-functionalization [23, 207], grafting of the initiator anchoring compound, grafting of the initiator onto the anchoring groups [197, 208, 209], and the ATRP of sodium acrylate onto the anchored initiators [66, 163]. The concentration of each species was chosen based on the values commonly chosen in the literature without further optimization [23, 66, 163, 197, 207-209].

In this research, two methods were pursued to create oil resistant membranes. In the first method, the entire membrane surface and pores were subject to surface treatment, while in the second method, only the top surface (facing the feed solution) of the membrane was subject to the surface treatments. The aim of the first method was to develop a benchmark for studying the effect of sparse-grafting of PAA on the oil adhesion properties and oil fouling in MD. It was also employed to refine and troubleshoot the possible issues with the experimental setups and implementation of the chemical reactions. Another important goal of this method was the selection of a membrane compatible with the selected reaction conditions. The second method was employed to develop an extreme end toward making a surface with concentrated patches of hydrophilic PAA molecules on a hydrophobic membrane surface to investigate the effect of surface interactions in the point-of-contact of the membrane and the feed liquid.

### 3.4 Approach 1: Grafting of PAA on the entire membrane

The aim of this method is to use the entire membrane surface and inside of the membrane pores as a base for grafting of PAA with different grafting densities. The purpose of this method is to create a benchmark that can subsequently be used to analyse the effect of sparse-grafting of hydrophilic compounds on the membrane surfaces. A commercial PVDF membrane (average pore size=0.45  $\mu\text{m}$ ) was employed in this approach.

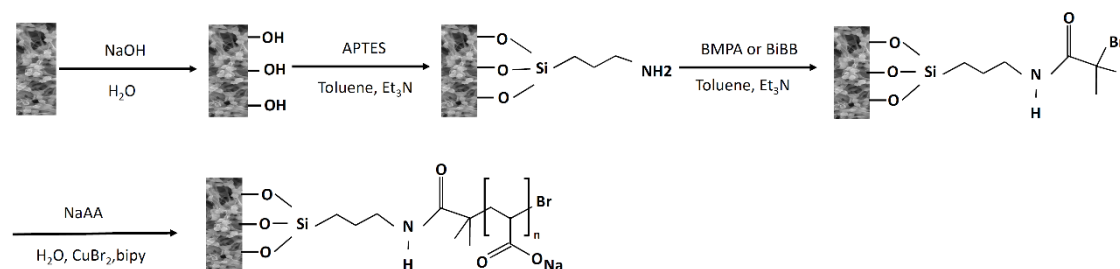


**Figure 3.1:** Proposed reaction steps for grafting of the poly(acrylic acid) (PAA) sodium salt on the surface of the PVDF membrane. The selected initiators were BMPA and BiBB for **Approaches 1** and **2**, respectively.

### 3.4.1 Alkaline treatment (OH-grafting)

In this approach, the membranes were fully prewetted before the initial step of surface treatment. For prewetting the membranes, the membrane coupons were first soaked in pure ethanol in a beaker to ensure that ethanol fills the membrane pores and makes it translucent. The ethanol was subsequently replaced by Milli-Q water by adding copious amounts of Milli-Q water and draining the beaker multiple times. The final membrane was removed from the beaker and placed in another beaker filled with Milli-Q water to avoid drying. For alkaline treatment reactions, the membrane was submerged in a highly-concentrated alkaline solution (7.5 M NaOH) at  $70 \pm 4^\circ\text{C}$  for 3 h [23]. The membrane was then removed from the beaker and washed thoroughly with Milli-Q water and dried in a drafted atmospheric oven at  $60^\circ\text{C}$  overnight, followed by drying in a vacuum oven at  $60^\circ\text{C}$  for 6-8 h to remove the residual moisture.

### 3.4.2 APTES-grafting

For this step, the OH-functionalized membranes were immersed in a 0.03 M solution of APTES in toluene, and the reaction was carried out in a sealed container under  $\text{N}_2$  blanket for 24 h in room temperature [210]. After the reaction, the membranes were extracted from the container and washed thoroughly with ethanol and water, and dried in a drafted oven at  $60^\circ\text{C}$ .

### 3.4.3 Initiator-grafting

In this step, BMPA was grafted onto the surface of the APTES-treated samples. For grafting of the initiator, a 0.02 M solution of BMPA in toluene was prepared at room temperature [197, 208, 209]. In addition, TEA was used for a few of the tested samples as a catalyst that can assist the silanization reaction. To perform the initiator grafting, the membranes were immersed in the solution and the reaction vessel was purged with  $\text{N}_2$  for 30 min to remove the moisture. Next, the reaction vessel was sealed and the reaction continued for 24 h at room temperature, on an orbital mixer [197, 208, 209]. At the end of the reaction, the membranes were removed from the vessel and washed thoroughly with ethanol and water, and dried in a drafted oven at  $60^\circ\text{C}$  overnight.

### 3.4.4 Oxygen tolerant UV-assisted ATRP for PAA grafting using **Approach 1**

ATRP was performed for all samples using a solution of NaAA, Cu(II)Br<sub>2</sub>, and bipy in water with the molar ratio of [NaAA]:[Cu(II)Br<sub>2</sub>]:[bipy] 0.5:0.005:0.01 [66, 163]. The mentioned solution was poured into several glass petri-dishes and the membranes were immersed in the petri-dishes. The polymerization started by exposing the petri-dishes to UV light (wavelength= 362 nm, power density at the exposure distance of 10 cm=2-2.5 mW/cm<sup>2</sup>) from above in open atmosphere at room temperature. The reaction was terminated by switching-off the UV light after 3 h. The membranes were then removed from the petri-dishes and washed thoroughly with ethanol and water, and dried in a drafted oven at 60°C overnight. In some of the samples, TEA (with a concentration of 0.2 M) was added to the reaction medium as catalyst. **Figure 3.2** presents the two alternative methods of loading the samples into the petri-dishes used in **Approach 1**. In the method shown in **Figure 3.2a**, the membrane was submerged in the polymerization solution inside a petri-dish, and another petri-dish (empty) was placed over the solution pushing the extra solution out of the petri-dish and floated over the solution. In the method shown in **Figure 3.2b**, the membrane was first placed on a dry petri-dish and a few drops of the polymerization solution was poured onto the membrane. The membrane was then covered using a microscope glass slide. The latter method was previously used in the literature for grafting of different polymers on silicon wafers [66].

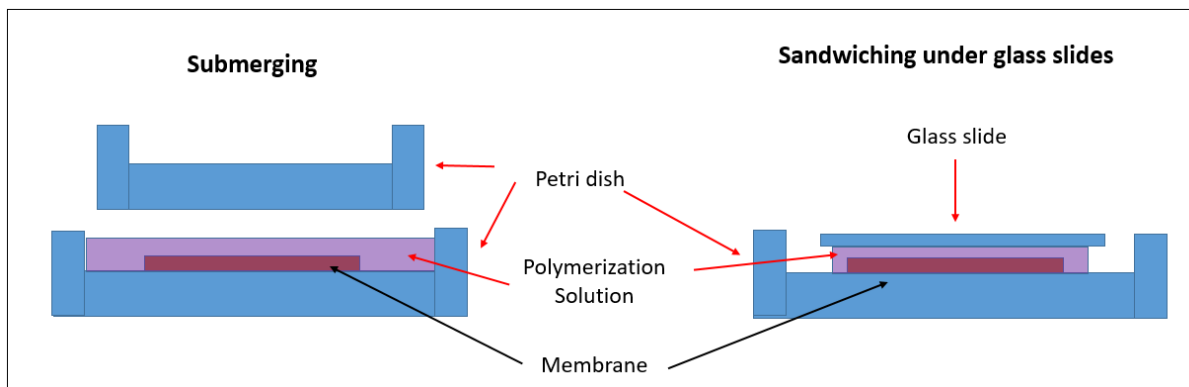


**Figure 3.2:** The schematic illustration of Different methods of performing the ATRP reactions by a) submerging the membrane in the polymerization solution, b) sandwiching the membrane and the polymerization solution between the petri dish and a glass slide.

### 3.5 **Approach 2:** Grafting of PAA on top of the roughness features of the MD membranes

In this approach, the PAA chains were grafted onto the commercial PVDF membranes (average pore size=0.2  $\mu\text{m}$ ) without the initial prewetting of the membranes to limit the grafting sites for the PAA brushes to the top surface of the membrane. The specific reaction conditions for this approach are described below:

### 3.5.1 Alkaline treatment

the PVDF membranes were initially OH-functionalized using a 7.5 M NaOH solution at room temperature for 3 h (alkaline treatment). For this purpose, a dry membrane coupon (without prewetting [207]) was fixed in a custom-made module exposing the top surface to the modification solution, while sealing the bottom surface. The membrane was secured in the custom-made module using silicone gaskets ensuring no liquid could bypass the membrane and reach the unexposed face of the membrane. Upon removal of the membrane from the module, the unexposed face of the membrane was carefully examined to ensure it was completely dry and free of any traces of liquid. After the alkaline treatment, the membrane was washed thoroughly with MilliQ water, and dried overnight in a drafted oven at 60°C.

### 3.5.2 APTES grafting

After the alkaline treatment, the membrane was removed from the module, washed thoroughly with MilliQ water, and dried overnight in a drafted oven at 60°C. The membranes were then functionalized by amine groups (-NH<sub>2</sub>) using a solution containing 0.03 M APTES and 0.044 M TEA in toluene, in a sealed container under N<sub>2</sub> blanket for 24 h at room temperature [210].

### 3.5.3 Initiator grafting

Next, the initiator, BiBB, was grafted onto the membranes using a solution containing 0.02 M BiBB and 0.01 M TEA in toluene, under N<sub>2</sub> blanket for 24 h at room temperature [197, 208, 209]. After each APTES and BiBB grafting steps, the membrane was washed thoroughly with n-hexane, and dried in a drafted oven at 60°C overnight.

### 3.5.4 Oxygen tolerant UV-assisted ATRP for PAA grafting employing **Approach 2**

For ATRP, the initiator-grafted membranes were first pre-wetted by ethanol in a glass beaker. The ethanol was then replaced by water through washing the membrane with copious amount of water. The pre-wetted membrane was transferred to and submerged in a petri-dish containing 25 mL of an aqueous solution containing [NaAA]:[Cu(II)Br<sub>2</sub>]:[bipy] with the molar ratio of 0.5:0.005:0.01 [66, 163]. The ATRP reaction was initiated by exposing the petri-dish to the UV light (wavelength= 362 nm, with the irradiance of 2-2.5 mW/cm<sup>2</sup> at the exposure distance of 10 cm) from the top in open atmosphere at room temperature [66]. The reaction was terminated after 3 h by switching off the UV light and removing the membrane from the petri dish. The membrane was then washed thoroughly with ethanol and water, alternately, and was dried in a drafted oven at 60°C overnight. The schematics for the reaction setup of **Approach 2** is shown in **Figure 3.3**. As observed from this figure, in Approach 2, the membrane was immersed in the polymerization solution without covering the reaction medium, directly exposing the system to the atmosphere.

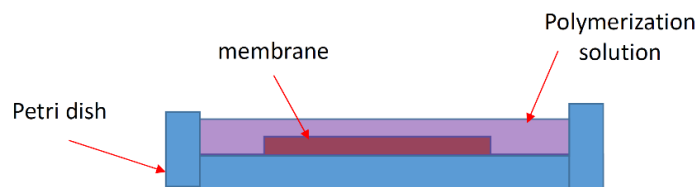


**Figure 3.3:** The schematic illustration of the reaction setup for performing the UV-ATRP reactions by submerging the membrane in the polymerization solution in **Approach 2**.

### 3.6 Membrane distillation experiments

MD experiments were performed in a custom-made module with a feed inlet temperature of 60°C and permeate inlet temperature of 20°C in the countercurrent configuration, with crossflow velocity of 3.13 m/min on both feed/permeate sides. The schematic of the MD setup is shown in **Figure 3.4**. The PVDF and PVDF-PAA membranes were tested against a mechanically dispersed aqueous oil solution containing 0.1 % (v/v) dodecane and 0.1 M NaCl. Immediately before performing MD on oily solutions, both membranes were tested with a 0.1 M NaCl solution for 2 hours to ensure the integrity of the membranes. The electrical conductivity (EC) of the permeate solution was monitored in real-time by an EC-meter probe placed inside the permeate container. The permeation flux data obtained from MD on the PVDF-salt system over the first 5 h of the experiment was used to calculate the standard error for the flux calculations and was employed in the flux graphs as error bars. At the end of each MD experiment, the membranes were removed from the module immediately to visually examine for any translucent spots created on the membrane surface as a result of possible wetting.

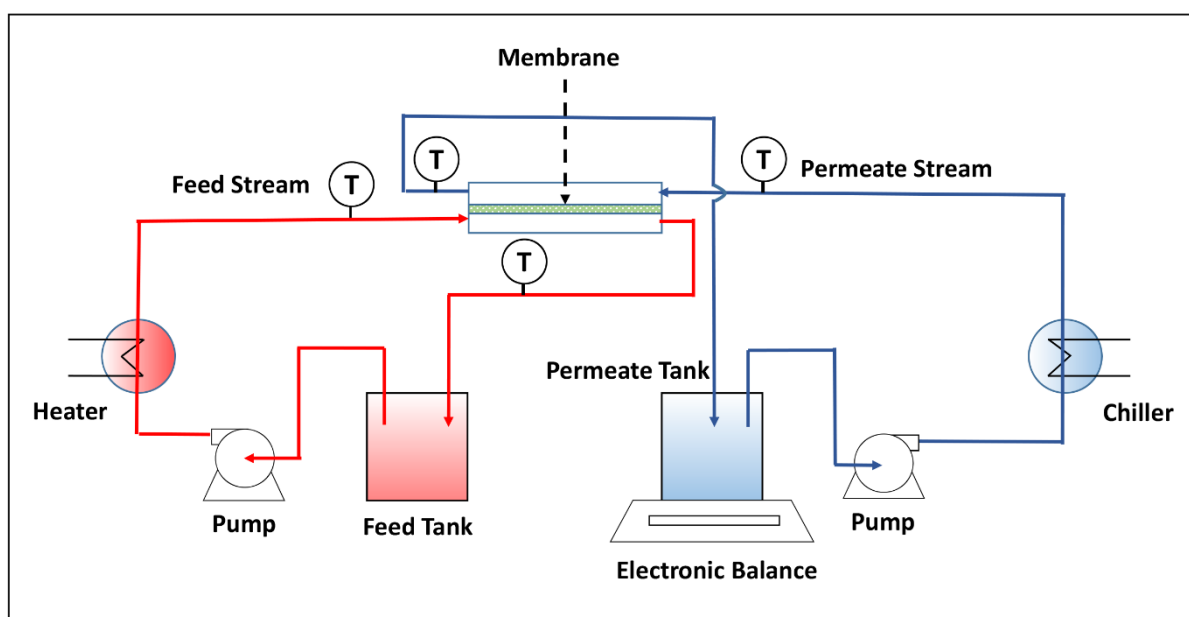


**Figure 3.4:** Schematic of the setup used to conduct MD experiments in this work. T indicates the location of the thermocouples for temperature measurement.

### 3.7 Preparation of the saline oil dispersions

The oil dispersion was prepared first with 4 mL of dodecane that was dispersed in 4 L of Milli-Q water using a high-shear mechanical mixer (Unidrive X1000, Caterpillar) at 15000 rpm for 15 min. Then, 23.38 g (0.4 mol) of NaCl was added to the solution and dissolved using a magnetic stirrer for 10 min. After the dissolution of the salt, the mixture was stirred again using the high shear mixer at 15000 rpm for 15 min. The solution was prepared at room temperature (about 20°C), and the resulting dispersion was stable at least for 2 h, but showed signs of phase separation visually observable as the solution becoming transparent on the bottom section of the container. Therefore, during the MD, the feed solution was replaced with a fresh solution at  $t=2$  h and  $t=4$  h from the start of the experiment to extend the time during which the membrane was exposed to the oily dispersion. In addition, the MD experiment was allowed to continue overnight (20 h in total) to observe the long-term effects of any possible oil wetting on the EC of the permeate solution. The oil droplets in the prepared dispersions were too large for the available DLS instruments for a successful measurement of droplet size distribution. Therefore, the oil droplet size was not measured for the prepared feed solutions pre- or post-MD.

### 3.8 EIS experiments

The EIS experiments were performed using an electrochemical workstation (Autolab PGSTAT12, Metrohm, Herisau, Switzerland) equipped with a FRA3.2 module. The tests were performed in potentiostatic mode with a current range of 100 nA to 10 mA and a maximum root-mean square (RMS) voltage amplitude of 0.01 V to avoid Faradaic reactions. A two-electrode configuration was employed using stainless steel electrodes with the working/sensing electrode facing the membrane from the feed side and the counter/reference electrode facing the membrane from the permeate side. A schematic of the MD cell showing the parts including the EIS electrodes in exploded view is shown in **Figure 3.5**.

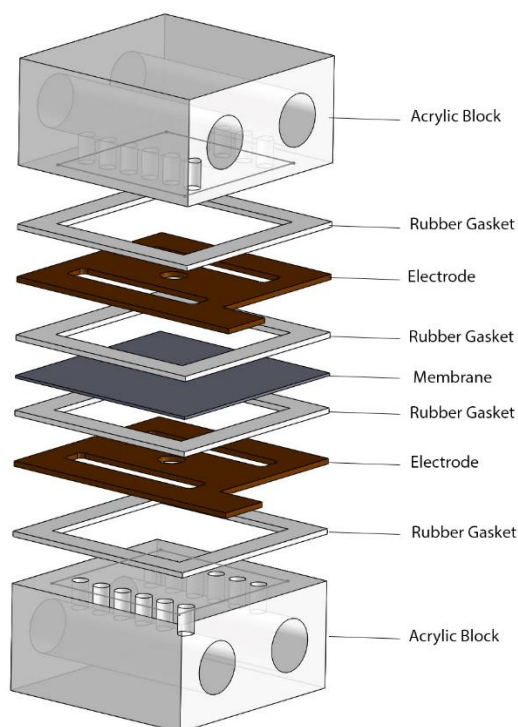


**Figure 3.5:** Exploded view of the MD cell employed in the current research, showing location of the electrodes, the flow channels, and the membrane.

The data acquisition was performed in both static (without MD operation), and dynamic (during MD operation) modes to obtain information on the changes taking place on the values of the equivalent circuit parameters, and to establish correlations between the EIS data and the physical properties of the MD system. For the static tests, the module was detached from the MD setup, and was filled with the relevant solution at room temperature. The frequency ( $f$ ) range for the static tests was 0.1 Hz to 500 kHz with 10 measured frequencies per decade. For the dynamic tests, the data acquisition took place *in-situ* during MD operation, performing one complete frequency sweep per hour with the first sweep starting at  $t=0$  h at the frequency range of 1 Hz to 500 kHz with 10 measured frequencies per decade (20 full frequency sweeps per each test). Each frequency sweep took about 15 min to 30 min, depending on the level of the noise and the ability of the instrument to acquire proper data in the low-frequency range. The capacitance of the rubber gaskets was obtained by numerical fitting using OriginPro 9.1. The rest of the obtained data were analysed and fitted by Nova 2.1.4 (Metrohm, Herisau, Switzerland). The curve fitting was done in slightly different manners depending on the level of noise in the original data (e.g., those with  $Z' < 0$  and  $-Z'' < 0$ ). For example, the fitting range for the noisy data sets was limited to the range of  $100 \text{ Hz} \leq f \leq 500 \text{ kHz}$ . For other data sets, the fitting was performed over the entire measured frequency range.



# Chapter 4 Proof of concept for oxygen-tolerant UV-assisted atom-transfer radical polymerization (ATRP) of Poly(acrylic acid) (PAA) onto PVDF Membranes

## 4.1 Introduction

The aim of this chapter is to develop a benchmark for refining and troubleshooting the possible issues with the experimental setups and implementation of the chemical reactions for oxygen-tolerant UV-ATRP on PVDF membranes. In this section, preliminary ATR-FTIR and water contact angle results are presented on the prepared samples. The aim of the performed characterizations was to investigate the success of each step of the surface modifications.

## 4.2 Validation of the initiator grafting reactions

### 4.2.1 ATR-FTIR Results on the treated and untreated membranes

ATR-FTIR results on the pristine PVDF, alkaline treated (PVDF-OH), APTES-treated (PVDF-APTES), initiator-grafted (PVDF-BMPA) and PAA-grafted (PVDF-PAA) membranes are shown in **Figure 4.1**. As can be observed from **Figure 4.1**, the PVDF-PAA membrane showed a new peak at 1550-1650  $\text{cm}^{-1}$ , which can be assigned to the  $-\text{COOH}$  stretching related to the acidic form of PAA [211-215]. However, no other peaks related to any characteristic bonds related to the grafted functional groups are observed in the collected spectra of the other steps of the surface treatment. This result could be attributed to the extremely low concentration of the functional groups on the membrane surface.

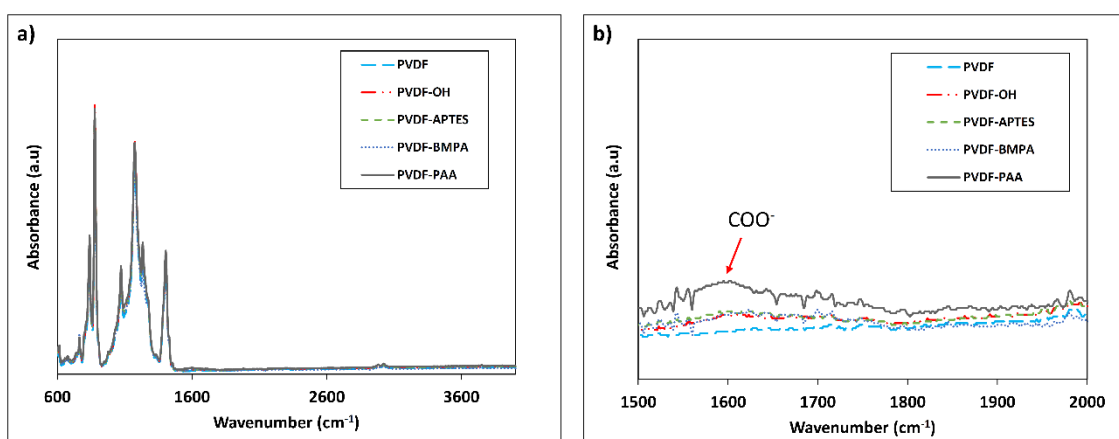


**Figure 4.1:** ATR-FTIR results on the pristine and surface-modified PVDF membranes using **Approach 1**: a) full view of the ATR-FTIR spectra, b) magnified view of the spectra (1500-2000  $\text{cm}^{-1}$ ) for observing the carbonyl peaks of the surface-grafted PAA.

To understand the effect of the presence of TEA in the polymerization solution in the ATRP of PAA, the ATR-FTIR spectra of the PVDF grafted in presence and in the absence of TEA were compared. **Figure 4.2** illustrates the ATR-FTIR spectra for the PVDF samples prepared using the two different ATRP methods with two different reactant compositions. As can be observed from this figure, the PAA-grafted membranes showed no significant difference in their FTIR spectra suggesting that the reaction was successful in both cases. However, ATR-FTIR data cannot be used for a quantitative measure of the grafting density or the degree of polymerization. For this purpose, water contact angle experiments might provide additional insight as to which method is more favourable.

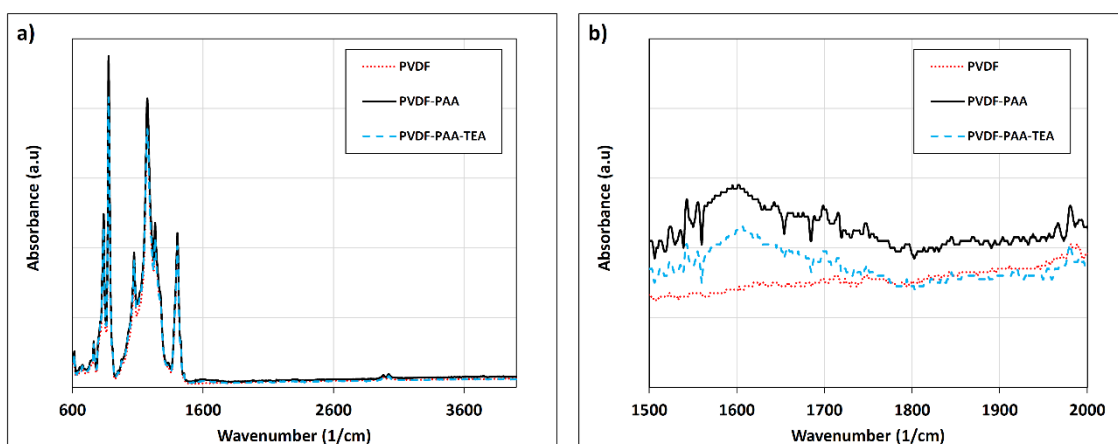


**Figure 4.2:** ATR-FTIR results on the pristine, PVDF-PAA, and PVDF-PAA-TEA membranes prepared using **Approach 1**: a) full view of the ATR-FTIR spectra, b) magnified view of the spectra (1500–2000  $\text{cm}^{-1}$ ) for observing the carbonyl peaks of the surface-grafted PAA.

#### 4.2.2 Water contact-angle measurements

Water contact-angle tests were performed to analyse the surface properties of the modified and pristine membranes. The WCA results for the treated and untreated PVDF samples are shown in **Figure 4.3**. As can be observed from this figure, different treatment steps resulted in different changes in the contact angles of the PVDF membranes. The OH-treated membranes exhibited a fully hydrophilic behaviour and the water droplets immediately wicked into the membrane. However, the membranes demonstrated higher contact-angle after APTES treatment. PVDF-PAA and PVDF-PAA-TEA membranes showed lower contact angles compared to the PVDF-APTES membranes. However, the contact angles of these membranes were unstable and the recorded values of contact angle were related to the average of multiple measurements within the first minute after dispensing the water droplet onto the membrane. Nevertheless, the PVDF-PAA membrane showed a lower contact-angle values as compared to the PVDF-PAA-TEA. This result could be due to the possible de-grafting effect of TEA in presence of water, which suggests that the use of TEA in the polymerization solution might be unfavourable for the reaction.

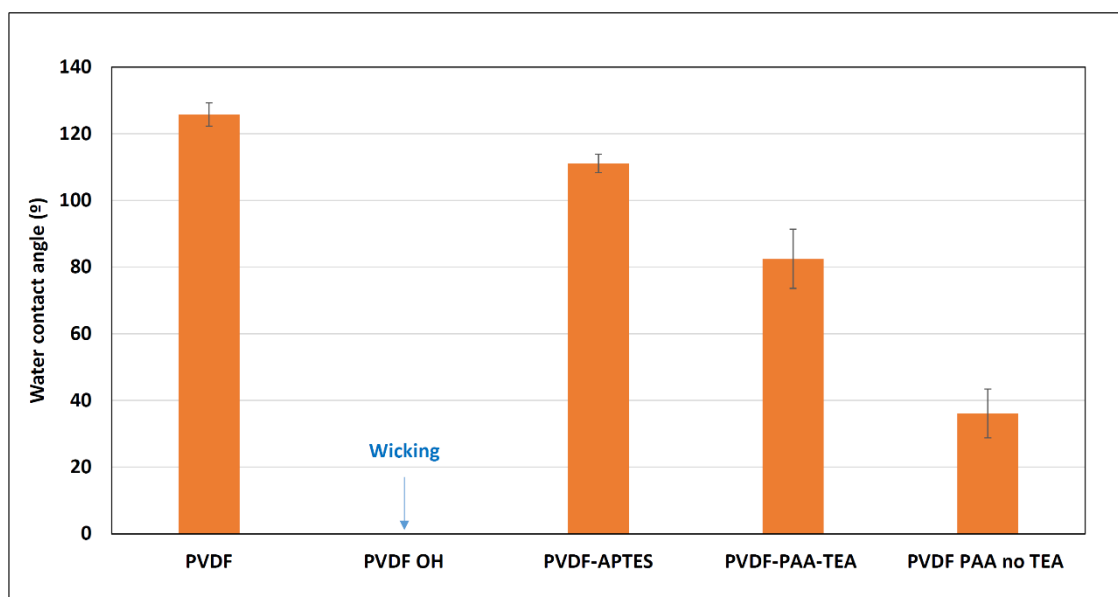


**Figure 4.3:** Water contact-angle results on the surface of the pristine as well as the treated membranes. The water droplets wetted the PVDF-OH membranes upon contact.

### 4.3 Discussions and conclusions on Approach 1

**Approach 1** was performed to fully graft PAA on the surface of the membranes as well as inside the membrane pores, to obtain a benchmark on the reaction conditions. Based on the visual observations made during the modifications process, PVDF membranes maintained their integrity during all of the modifications steps, therefore, these membranes are more suitable to be used for the next steps of this study.

According to the ATR-FTIR results, the surface concentration of the functional groups that were grafted before PAA was too low to show any noticeable effect on the ATR-FTIR spectra. However, the PAA chains exhibited a peak at  $1550\text{-}1650\text{ cm}^{-1}$ , which can be attributed to  $\text{-COOH}$  stretching of the PAA molecules which confirms the success of the employed reaction conditions [211-215]. In addition, it was found that the presence or absence of TEA in the polymerization solution did not have an effect noticeable in the ATR-FTIR spectra on the success of the ATRP in PAA grafting. Water contact angle results provided additional insight into the changes in the surface properties of the membranes through different stages of surface modifications. Especially, these results showed a lower contact angle for PVDF-PAA as compared to PVDF-PAA-TEA, implying that the presence of TEA in the polymerization solution might have led to the de-grafting of PAA chains by catalysing the hydrolysis of the silane bonds (formed by the APTES grafting) in presence of water [216].

In general, results of this chapter indicated the success of the oxygen-tolerant UV-assisted ATRP in the grafting of PAA onto the PVDF membranes. Nevertheless, membranes grafted using **Approach 1** cannot be directly employed for MD applications due their hydrophilic nature.

Therefore, as describe in **Chapter 3, Approach 2** was designed to limit the grafting sites for the PAA molecules only on the top (feed-facing) surface of the membrane. This approach will be adopted in the rest of the thesis and the results of this approach will be discussed in **Chapters 5 to 8**.

# Chapter 5 Salinity-responsive poly(acrylic-acid)-grafted PVDF membranes by oxygen tolerant atom-transfer radical polymerization (ATRP) for oil-resistant membrane distillation

---

## 5.1 Introduction

In the previous chapter, the successful grafting of PAA chains was verified for **Approach 1** which resulted in a hydrophilic membrane. As described in **Chapter 3**, the employed method for the surface treatments of **Approach 1** was further developed into **Approach 2** by grafting the PAA chains only on the top surface of the PVDF membrane. This approach is hypothesized to be effective against the adhesion of dispersed oil droplets in the treatment of oily waters due to the hydration and electrostatic repulsions between PAA brushes and the oil droplets.

In this regard, the current chapter is focused on the characterizations, salinity responsive behaviour, and MD performance of a commercial PVDF membrane (pore size = 0.2  $\mu\text{m}$ ) modified using **Approach 2**. For this purpose, the surface chemistry and morphology of PVDF and PVDF-PAA membranes will be analysed in **Section 5.2** using various methods such as ATR-FTIR, and SEM-EDX analyses to confirm the success of the oxygen tolerant UV-ATRP in the grafting of PAA brushes onto the PVDF membranes. Next, the underwater oil adhesion properties of both membranes as well as the salinity responsive behaviour of the PVDF-PAA membrane will be analysed in **Section 5.3**. Finally, the performance of both membranes will be evaluated in the MD of a saline oil dispersion containing 0.1 % (v/v) dodecane and 0.1 M NaCl in water in **Section 5.4**. Full description of the experimental procedures used in the current chapter can be found in **Chapter 3**.

## 5.2 Surface chemistry and morphology of the PVDF-PAA membranes

Changes in the surface chemistry of the membranes can be observed through the ATR-FTIR results shown in **Figure 5.1**, where the inset of this figure shows the magnified region in the range 1500-4000  $\text{cm}^{-1}$  of the same spectra. As can be observed in the inset graph, a new peak can be observed for PVDF-PAA at 1580  $\text{cm}^{-1}$  which can be attributed to the asymmetric stretching of  $\text{-COO}^-$  related to the sodium salt of PAA [211, 214, 217]. This peak is followed by a shoulder at 1680  $\text{cm}^{-1}$  which can be assigned to the  $\text{-COOH}$  stretching related to the acidic form of PAA [211-215]. Additionally, a broad peak can be observed in PVDF-PAA in 3000-3500  $\text{cm}^{-1}$  which can be attributed to the  $\text{-OH}$  groups in the hydrogenated form of PAA [211-214]. The presence of both

forms of PAA can be attributed to the exchange of  $H^+$  and  $Na^+$  ions, as a result of exposure of the PAA sodium salt to water during the washing process [215].

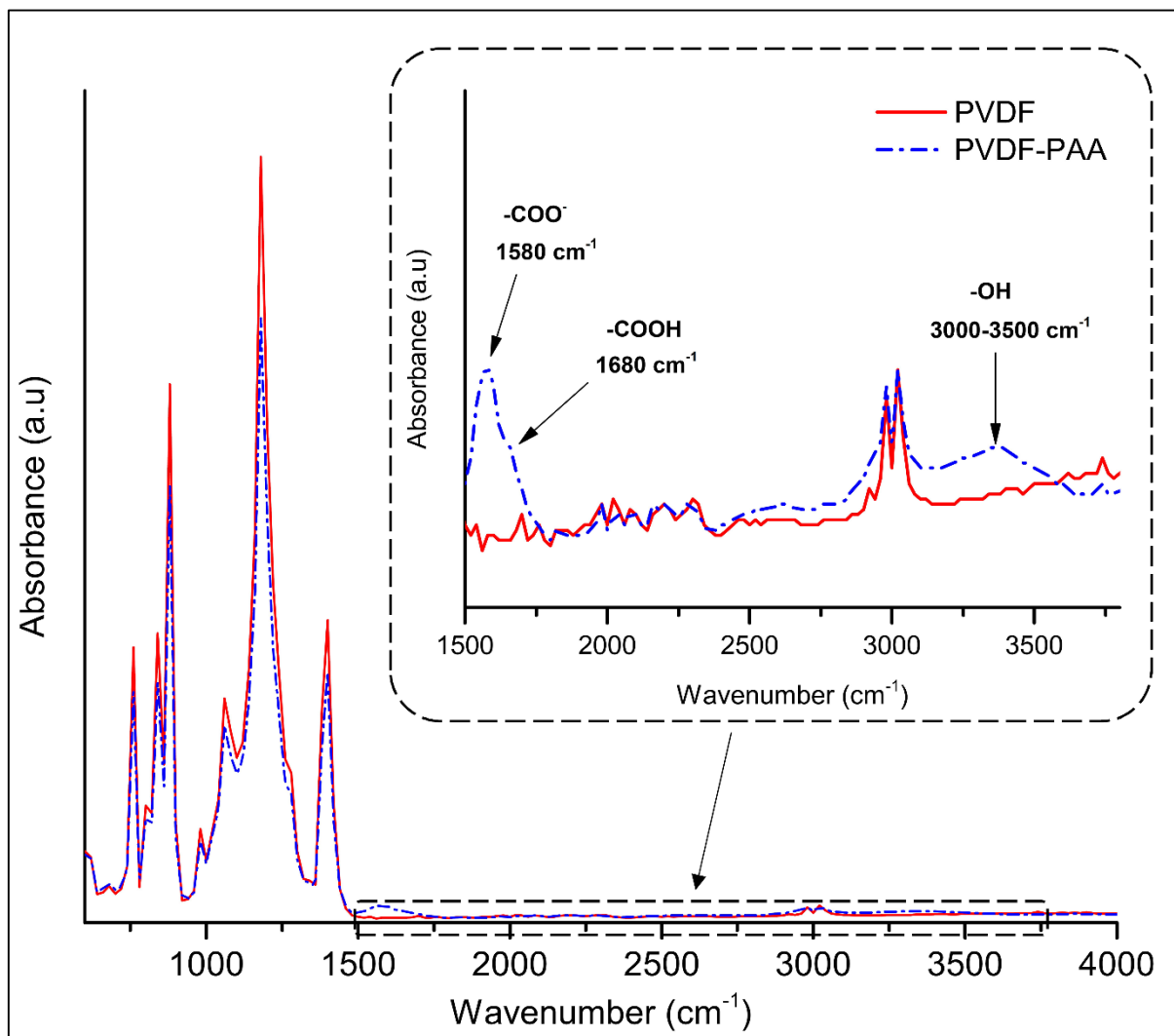


**Figure 5.1:** ATR-FTIR spectra of PVDF and PVDF-PAA membranes.

SEM analysis was performed to investigate the changes in the surface morphology of the PVDF membranes due to PAA grafting. The SEM images obtained from the top surface (the surface facing the feed solution) of the PVDF and PVDF-PAA membranes are shown in **Figures 5.2a** and **b**. As can be observed from these figures, there is no noticeable difference in surface morphology between the PVDF and PVDF-PAA membranes.

EDX analysis on the PVDF and PVDF-PAA membranes can provide information on the effect of PAA grafting on the elemental composition of the membrane surfaces. This analysis was performed on three selected spots on top of the nodular roughness features (asperities) (**Figures 5.2c** and **d**), as well as for a region (**Figures 5.2e** and **f**) on the surface on each membrane. It

should be noted that the electron beam penetration depth for the EDX spectra is ca. 2 – 5  $\mu\text{m}$  [218], meaning that the obtained results could be influenced by the corrugations of the surfaces as well as the underlying bulk material that can make an additional contribution to the elemental composition measured by the instrument.

The resulting EDX spectra of the spot and region analyses are shown in **Figure 5.2g**. As can be observed from the EDX spectra (**Figure 5.2g**), oxygen is present on the surface of both modified and unmodified samples with relatively low concentrations. PAA chains contain oxygen and carbon atoms that can increase the surface concentration of these elements on the membrane surface in the PVDF-PAA membrane as compared to those in the PVDF membrane. However, addition of PAA onto the PVDF membrane affects the concentration of all of the elements on the PVDF simultaneously. Therefore, instead of analysing the values of the atomic concentrations, it is more informative to analyse the relative concentrations of O/F, O/C, and C/F in the obtained results. The results of these calculations are shown in **Figure 5.2h**. As can be observed from the concentration ratios of the spots, the concentration of oxygen and carbon has increased relative to fluorine for the PVDF-PAA membrane illustrating the presence of PAA chains on the top of the surface asperities.

However, a comparison of the values obtained for the region analysis does not show any significant difference between the two samples, with the PVDF-PAA sample having a slightly higher O/F ratio. In addition, comparison of the region results and the spot results for both membranes show a large difference for the PVDF-PAA, while the difference is smaller for the PVDF membrane. This suggests the possibility of a higher grafting density on top of the asperities for the PVDF-PAA membrane. This could be the result of the minimal intrusion of the alkaline solution in the first surface modification treatment step (**Chapter 3**), which limited the anchoring points of the PAA chains to the top regions of the roughness features. This hypothesis will be discussed in more detail in **Sections 5.3** and **Chapter 6**. Alternatively, the high oxygen content on top of the surface asperities in PVDF-PAA could mean that the molecular weight of the PAA chains located here is larger than those located in the valley regions, due to a better exposure to UV light during ATRP.



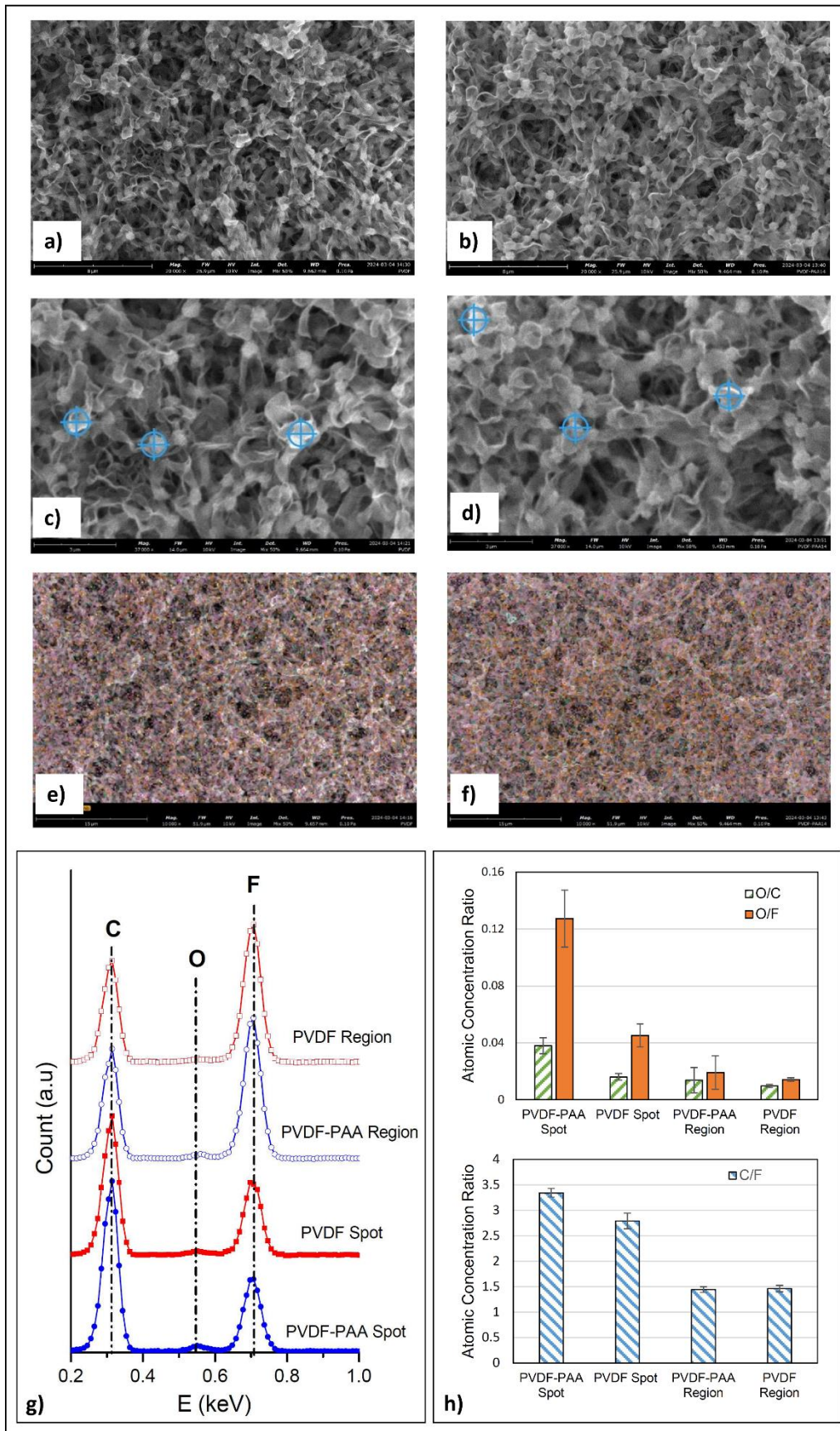


**Figure 5.2:** SEM images of PVDF (a) and PVDF-PAA (b) membranes. Spots selected for the EDX analysis of PVDF (c), and PVDF-PAA (d) membranes. Region images for the EDX analysis on the PVDF



(e) and PVDF-PAA (f) membranes. e) Atomic concentration ratio of O/C and O/F in PVDF and PVDF-PAA obtained from the EDX analysis. The scale bars correspond to  $8 \mu\text{m}$  (in a and b),  $3 \mu\text{m}$  (in c and d), and  $15 \mu\text{m}$  (in e and f).

Streaming potential analysis was performed to obtain the apparent surface zeta potential ( $\zeta$ ) of the PVDF and PVDF-PAA membranes, in order to study the effect of PAA on the surface zeta potential, the results of which are shown in **Figure 5.3** as a function of pH. As observed, the presence of negatively-charged PAA molecules on PVDF-PAA has led to a larger negative surface zeta potential on the membrane surface as compared to the PVDF membrane. The isoelectric point (IEP) of the PVDF-PAA membrane is reached at a higher pH as compared to the PVDF membrane. This could be due to the PAA chains being deprotonated at a higher pH ( $\text{pK}_a$  of PAA is 4.3-4.9 [63]). In addition, presence of the secondary amine groups on the anchoring points of the PAA molecules and unreacted primary amine groups from APTES may have contributed to the increase in the pH of the IEP in the PVDF-PAA membrane. The amine groups of PVDF-PAA can become protonated at low pH leading to a more positive surface charge as compared to PVDF.

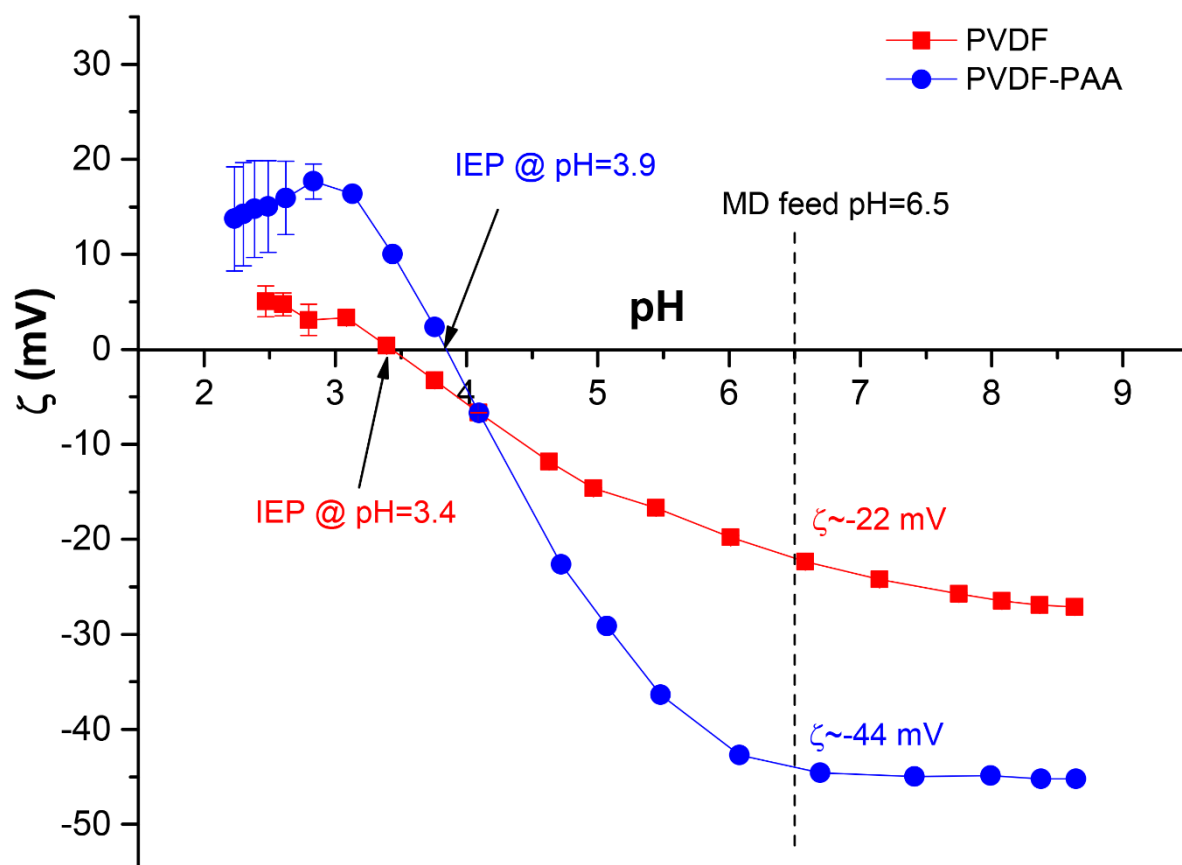


**Figure 5.3:** Surface zeta potential of PVDF and PVDF-PAA membranes as a function of pH using a 0.1 M NaCl solution at room temperature. The error bars represent the standard deviation of four measurements and are smaller than the data points for  $\text{pH} > 3$ .

The in-air water contact-angle (WCA) results for PVDF and PVDF-PAA membranes are shown in **Figure 5.4**. As observed, the WCA decreased from  $134 \pm 2^\circ$  for the pristine PVDF to  $110 \pm 3^\circ$  for PVDF-PAA. However, it should be noted that hydrophobic properties of the studied MD membranes cannot be unambiguously interpreted from the WCA results due to their rough and porous structure which affects the apparent contact angle [147, 148]. The observed decrease in the apparent contact angle suggests a change in surface chemistry or topography which needs to be complemented by other results.

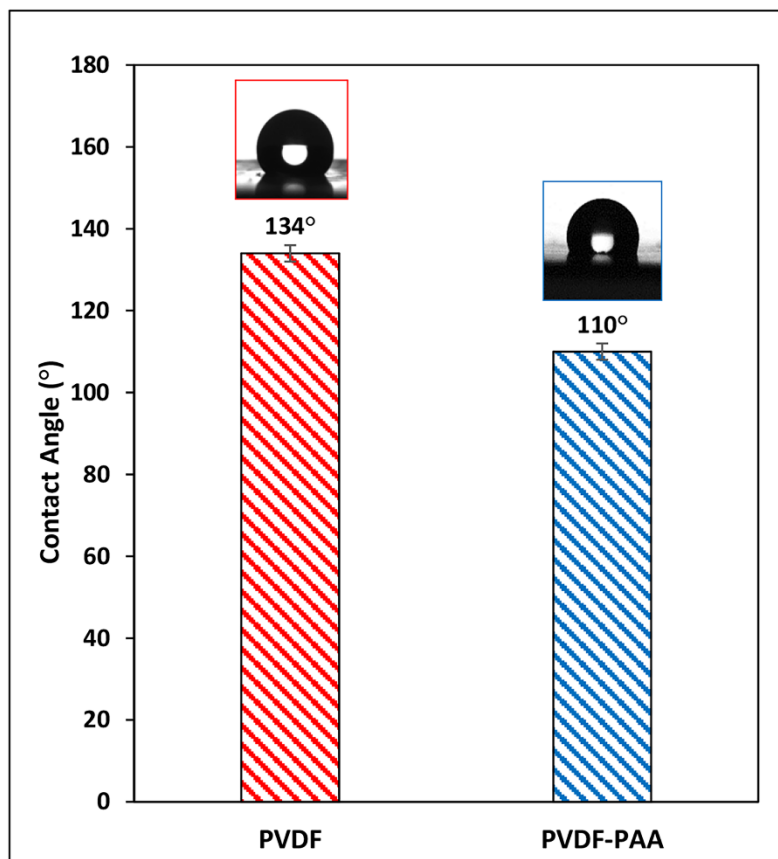


Figure 5.4: Water contact angle of PVDF and PVDF-PAA membranes

### 5.3 Salinity-responsive behaviour and underwater oleophobicity of the PVDF-PAA membranes

To analyse the salinity-responsive behaviour of the grafted brushes, underwater oil adhesion tests were performed on PVDF and PVDF-PAA membranes using dodecane in aqueous solutions with different concentrations of NaCl (from MilliQ water to 3 M NaCl). Snapshots from the oil adhesion experiments at the respective stage of approach, contact and retraction are shown in **Figure 5.5**.

For the PVDF membrane, in all of the tested solutions, when the oil droplet came into contact with the membrane surface, it instantaneously snapped onto the surface (the “contact” stage in

**Figure 5.5)** breaking off from the needle. The penetration of the oil droplet continued afterward until the droplet was completely infused into the membrane leaving a translucent area on the sample (not shown in the figures).

For the PVDF-PAA membrane under Milli-Q water and under 0.001 M NaCl solution, the oil droplet adhered to the surface in the contact step, but did not show the instant snapping behaviour upon contact which was observed for the PVDF membrane. Upon retraction, the oil droplet remained attached to the membrane, subsequently penetrating the membrane over time. With further increase in the salinity of the solutions (from 0.01M NaCl up to 3 M NaCl), the oil droplets did not adhere to the PVDF-PAA membrane surface upon approach, contact, or retraction.

The observed increase in underwater oleophobicity of PVDF-PAA with salinity can be attributed to the response of the PAA brushes to the presence of NaCl in the solution and stretching of these brushes in the osmotic brush regime (as explained in **Chapter 2**, Section 2.7.4). However, according to the previous studies on brush-coated nonporous smooth surfaces, the osmotic brush regime does not persist in salt concentrations of higher than 0.1-0.5 M [151, 214, 219, 220]. Instead, the salted brush regime prevails at salt concentrations of higher than this threshold, and the adhesion force of the oil droplets to the brush-grafted surfaces is expected to increase with salinity due to the collapse and dehydration of the brushes [154, 221]. Nevertheless, the increase in the adhesion force at high salinities ( $\geq 0.1$  M NaCl) did not seem to noticeably undermine the underwater oleophobicity of the PVDF-PAA membranes investigated in the current study.

A similar behaviour was observed by other researchers in their studies on antifouling zwitterionic brush-grafted surfaces [40, 152, 158, 222-224]. For instance, Zhang et al., [158] grafted a zwitterionic polymer, namely poly(sulfobetaine methacrylate) (PSBMA) brush onto a commercial thin-film composite forward osmosis (FO) membrane to increase its underwater oil-resistance properties. They observed a slight increase in the brush height for the brushes in 0.5 M NaCl as compared to those in DI water. In addition, they observed an increase in underwater oil contact angle and a decrease in the adhesion force of the brush-grafted surfaces in presence of 0.5 M NaCl. In their FO experiments, the flux of the modified membranes showed a decline with time, but when the membranes were cleaned using the 0.5 M NaCl solution, almost 94% of the original flux was recovered after each cleaning step, while the cleaning had a weaker effect when DI water was used. This effect highlights the ability of the salt in the detachment of oil droplets from brush-grafted surfaces [40, 158].

The analysis of the effect of salt on the underwater oleophobicity of brush-grafted porous and rough hydrophobic surfaces of MD membranes is more complex than that on smooth non-porous surfaces. This complexity originates from the entrapment of water and/or air pockets inside the pores and roughness cavities of the membrane surface, forming a four-phase system of oil, water,

air, and solid membrane [147]. A partially hydrophilic membrane surface adds another solid phase to the mentioned four-phase system, making the analysis even more complex. In addition, apart from affecting the thickness and hydration of the PAA brushes, the change in the salinity can affect the oil-water, solid-water, and air-water interfacial tensions. The combination of these effects can lead to underwater oleophobic scenarios under special conditions of surface energies and topographies [147-149]. Therefore, it is possible that the response of the PAA chains to salinity is only one of the contributing factors to the observed changes in the underwater oleophobicity. The underwater oleophobicity of the PVDF-PAA membranes will be further investigated in **Chapter 6** by proposing models for the surface chemistry of PVDF-PAA membrane and considering the wetting states of the membrane surfaces.

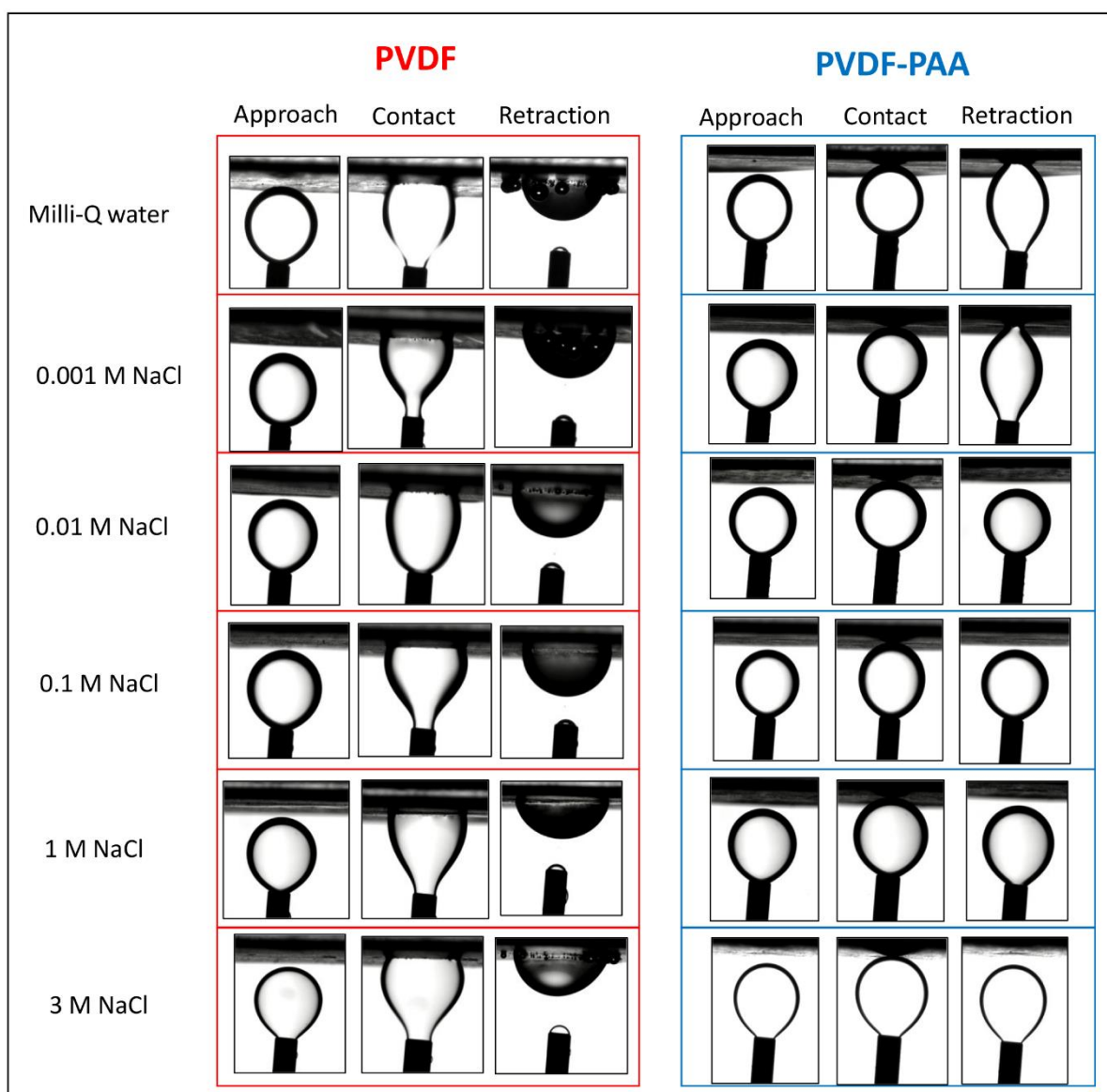


**Figure 5.5:** Results of underwater oil adhesion tests on PVDF and PVDF-PAA membranes.

#### 5.4 Effect of membrane surface modifications on oil fouling resistance of the MD membranes

The permeation flux and EC for PVDF and PVDF-PAA alongside a photograph of each membrane after the process are shown in **Figure 5.6a** and **b**, respectively. As can be observed in **Figure 5.6a**, for the PVDF membrane, permeate flux started to decrease by about 17% from  $\sim 12.5 \text{ kg}/(\text{m}^2 \cdot \text{h})$  at  $t=1 \text{ h}$  to  $\sim 10.1 \text{ kg}/(\text{m}^2 \cdot \text{h})$  at  $t=2 \text{ h}$  from the start of the MD test. The flux further decreased down to  $\sim 2.6 \text{ kg}/(\text{m}^2 \cdot \text{h})$  at  $t=5 \text{ h}$ . Until this point, no significant change was observed in EC. However, beyond this point, the permeate EC started to rise alongside the value of the flux until the end of the experiment (20h), suggesting the intrusion of the feed liquid into the permeate stream. A visual observation of the membrane after MD (**Figure 5.6a**) showed that the PVDF membrane had become translucent at many spots, particularly in the regions where the membrane was in direct contact with the spacer, as well as the edges of the membrane. The decrease in flux in the MD of dispersed oils has been widely observed for hydrophobic membranes in the literature [6, 7, 9-14, 16-18, 20, 22, 23]. This phenomenon can be attributed to the adhesion of the oil droplets to the membrane as a result of hydrophobic interactions which leads to pore blockage. The subsequent increase in flux (observed from  $t=5 \text{ h}$  to  $t=20 \text{ h}$ ) could be related to the leakage of the salt solution across the membrane due to oil fouling as implied by the onset of the increase in the permeate EC [6, 7, 9-18, 20-23].

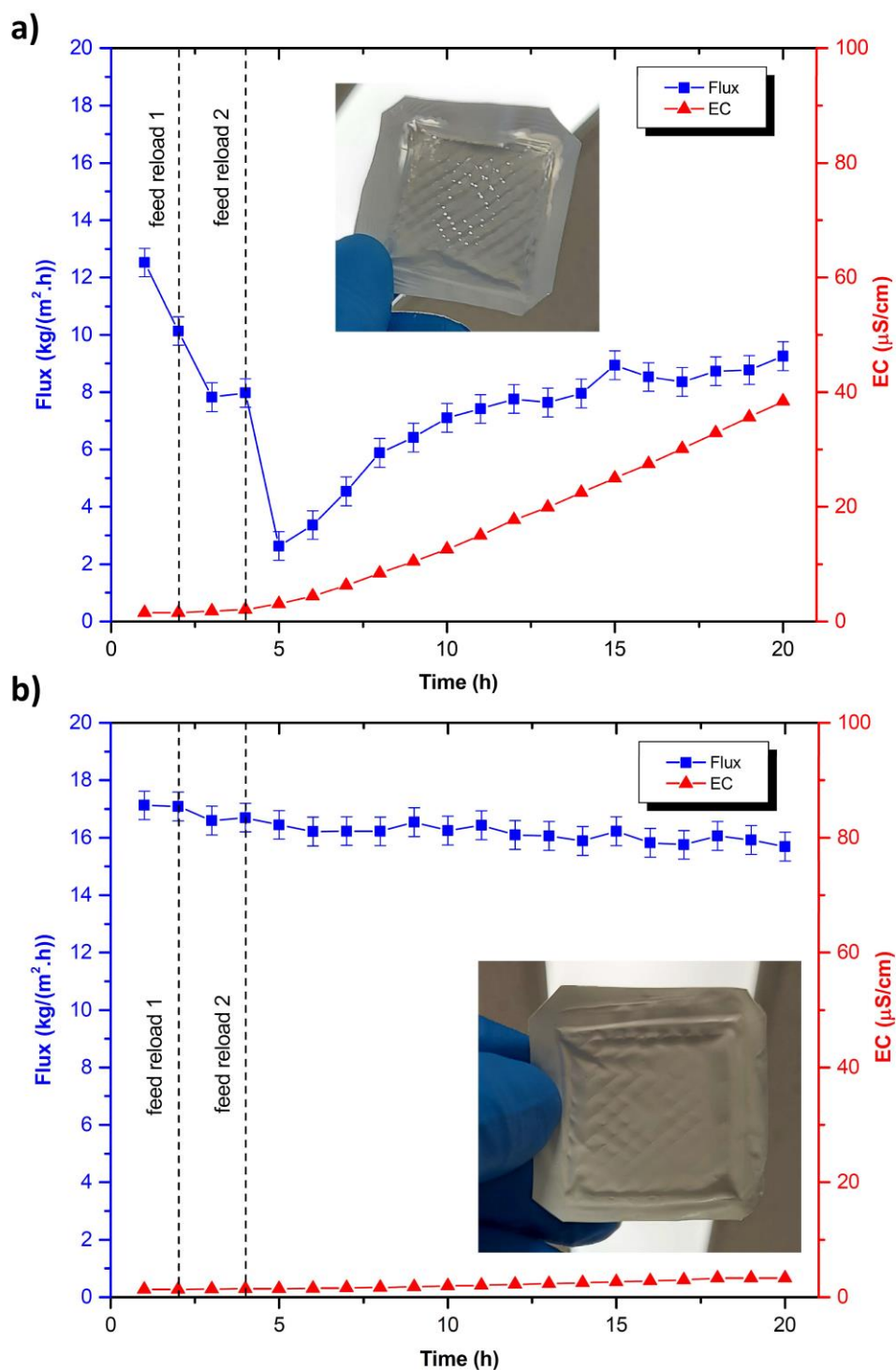


**Figure 5.6.** MD permeation flux and EC for a) PVDF and b) PVDF-PAA. Feed and permeate inlet temperatures were constant at 60°C and 20°C, and the crossflow velocity of both feed and permeate was 3.13 m/min. The oily dispersion contained 0.1 % (v/v) dodecane and 0.1 M NaCl in water.

In contrast to the PVDF membrane, the flux of the PVDF-PAA membrane and its permeate EC (**Figure 5.6b**) were almost constant with a slight decrease in flux from 17 kg/(m<sup>2</sup>·h) to 16 kg/(m<sup>2</sup>·h) throughout the test (20 h). In addition, the visual observation of the membrane coupon after the MD (the photograph in **Figure 5.6b**) did not show any sign of translucent areas, further

confirming that the membrane was not wetted during the tested period. This behaviour can be attributed to the underwater oleophobicity of the PVDF-PAA membranes in the salinity of 0.1 M NaCl based on visual observations as discussed in **Section 5.3**.

The importance of underwater oleophobicity of the MD membranes in the oil adhesion resistance has been highlighted by many researchers [6, 7, 9, 10, 12-18, 20-23]. However, the relevance of this property to the membrane performance is not well-understood yet. For instance, Wang et al. [18] prepared two hydrophilic-hydrophobic Janus membranes by coating a hydrophobic PVDF membrane with positively charged (poly(diallyldimethylammonium chloride) (PDDA)) and negatively charged (polydopamine (PDA)) hydrophilic polymers. Their findings suggested that despite both polymers being in-air hydrophilic and underwater-oleophobic, the PDA-coated membrane showed good oil adhesion resistance and a stable permeation flux during MD (for 12 h) of dispersed shale-gas oil solutions due to its negative surface charge, while the membrane coated with PDDA was fouled severely with a significant flux drop in less than 6 h. The observed effects were attributed to the electrostatic repulsions between the negatively charged PDA and the negatively charged oil droplets. Generally, a negative surface charge is considered to be more favourable for the oil-resistant membranes because the dispersed oil droplets are almost always negatively charged and the oil-membrane electrostatic repulsions can contribute to the resistance of the membrane to oil adhesion [18, 154].

In the current research, the surface zeta potential of PVDF-PAA was measured to be  $\sim -44$  mV (Figure 5) which was almost twice its value for the pristine PVDF ( $\sim -22$  mV) at the pH of the MD experiments (6.5). Therefore, electrostatic interactions could contribute to the oil-adhesion resistance of the PVDF-PAA membrane. In addition, the PAA brushes maintain a hydration layer on the membrane that can prevent the adhesion of oil droplets onto the membrane.

The anti-oil wetting properties of the PVDF-PAA membrane could also originate from the special geometry of the membrane surface and the location of the PAA brushes on the membrane surface. As discussed in Section 3.2, the PVDF-PAA membrane was found to be underwater oleophobic under 0.1 M NaCl solution. However, the in-air WCA results showed that the PVDF-PAA membrane had an apparent contact angle of larger than  $90^\circ$  which is in contrast to most studies that observed an in-air contact angle of lower than  $90^\circ$  for the Janus membranes [6, 7, 9, 10, 12-14, 16-18, 20, 21, 23]. This implies that other phases may play a role in the underwater oleophobicity of the PVDF-PAA [147, 148]. Therefore, the underwater oleophobicity of the PVDF-PAA membrane will be analysed further by developing a model for the surface structure of this membrane in the next chapter (**Chapter 6**).

## 5.5 Conclusions

Negatively charged polyelectrolyte brushes of PAA were explored in the current research for creating salinity-responsive anti-oil-adhesion membranes due to their strong hydration and negative electrostatic charge. Surface grafting of the PAA brushes was performed using UV-assisted oxygen tolerant SI-ATRP on a commercial PVDF membrane to address the current challenges of the commonly used surface-initiated (SI)-ATRP in using oxygen-free atmosphere.

The surface modifications were performed without pre-wetting of the PVDF membranes, and the resulting PVDF-PAA membrane was found to be in-air hydrophobic despite the hydrophilic modification of the top surface. The analysis of the surface chemistry and morphology of the membranes showed evidence of a higher surface concentration of oxygen and carbon on top of the surface roughness features as compared to the wider region on the membrane implying that the surface grafting has taken place predominantly on the top of the roughness features.

The underwater oil adhesion tests performed under different salinities as well as under Milli-Q water for both membranes showed that oil could penetrate the PVDF membrane under all of the tested conditions. However, for the PVDF-PAA membrane the oil penetration only occurred in Milli-Q water and in the saline solution with 0.001 M NaCl, while for the higher salinities up to 3 M NaCl, the oil droplet did not adhere or penetrate this membrane. The increase in the oil adhesion resistance of the PVDF-PAA membranes in response to the increase in salt concentration can be attributed to the response of the PAA brushes as well as possible changes in the surface energies of the interacting surfaces, which should be further analysed in future studies.

The PVDF and PVDF-PAA membranes were tested in MD with an oil in water dispersion containing 0.1% (v./v.) dodecane and 0.1 M NaCl. The MD results showed that the PVDF membrane was fouled and wetted by oil immediately; while the PVDF-PAA membrane maintained its non-wetting behavior throughout the test period of 20 h with only a slight flux drop from 17 kg/(m<sup>2</sup>.h) to 16 kg/(m<sup>2</sup>.h).

Salinity-responsive membranes can potentially be employed in the applications involving complex wastewaters containing hydrophobic, hydrophilic and amphiphilic solutes that can adhere to various types of surfaces. Switching the surface properties to the opposite wetting state in response to salinity can be utilized in these membranes to detach the adhered foulants from the membrane surface. Nevertheless, more research is needed to identify the limitations of the polyelectrolyte-grafted MD membranes and to develop suitable in-situ cleaning strategies to fully harness their stimuli-responsive behavior in fouling removal and membrane regeneration.



# Chapter 6 Proposed models for the surface chemistry of the as-prepared PVDF-PAA membrane and their wetting properties

---

## 6.1. Introduction

This chapter focuses on the development of conceptual models for surface structure of the PVDF-PAA membrane described in **Chapter 5** to better understand the underwater oleophobicity of this membrane. For this purpose, two models are firstly proposed here for the membrane surfaces which are different in terms of the position/distribution of the PAA molecules on the surface. Next, the in-air water contact angle and the underwater oil contact angle of these models are evaluated under different wetting scenarios and based on different combinations of assumptions for the wetting states and the phases involved in the each of the proposed models. These contact angle values are plotted as a function of two independent parameters, namely, the surface fraction of the PAA on the top surface ( $f_{PAA}$ ), as well as the surface fraction of the top surface ( $f_{top}$ ) (described below in **Section 6.2**), to identify the conditions that can lead to underwater oleophobicity in each scenario.

## 6.2. Models for the surface chemistry of PVDF-PAA membrane

As described in **Chapter 3** (Materials and Methods), the OH-functionalization was performed by exposing the PVDF membranes to the alkaline solution without pre-wetting the membranes. The alkaline solution leads to the local “-OH”-functionalization of the membrane at the points of direct contact between the liquid and the solid surface (i.e., solid-liquid interfaces). The surface-tethered -OH groups constitute the reaction sites for the subsequent surface modification steps. Therefore, the PAA chains are expected to be located at the liquid-solid interfaces originally in a direct contact with the alkaline solution of the first modification step.

The portion of the surface that is functionalized by -OH groups depends on the membrane surface properties (e.g., surface energy, roughness, pore size), surface tension of the alkaline solution, the progressive hydrophilization of the membrane, and reaction conditions (e.g., time and temperature). Therefore, the exact wetting regime of the membrane in terms of Cassie-Baxter and Wenzel theories during the alkaline treatment process cannot be determined using the available experimental data in this study. However, it is possible to perform a qualitative analysis and develop a model that can describe the behaviour of the as-prepared PVDF-PAA membrane.

Due to the hydrophobic nature of the PVDF membrane substrate, the alkaline solution cannot penetrate the membrane upon initial exposure to the membrane surface. If it is assumed that no further solution ingress occurs beyond the solid-liquid-air contact line as a result of the alkaline treatment, and only the top surface of the nodular roughness features is functionalized by -OH groups (and later by PAA molecules). It is also assumed that the -OH groups and the corresponding PAA molecules are not located on the inner surfaces of the pores. Herein, this model will be referred to as **Model 1**. The final result of this model is shown in **Figure 6.1a** with the PAA chains located only on top of the surface roughness features (represented by the green circles on top of the outer surface in **Figure 6.1**), and the air-water interface forming both on the partially wetted roughness features and near the entrance of the pores.

Another extreme case can happen in case the three-phase (air-liquid-PVDF) contact line of the alkaline solution advances into the external roughness cavities and partially enters the pores down to a point in a certain depth beneath the top surface of the membrane. This model is referred to as **Model 2**. A schematic illustration of the final product (i.e., after PAA grafting) of this model is shown in **Figure 6.1b** with PAA chains covering the top surface as well as a portion of the interior surface of the pores, and the air-water interfaces forming inside the pores. The surfaces shown in **Figures 6.1a** and **b** are assumed to be topographically similar to each other with a rough outer surface and cylindrical and uniform-sized nanometer scale pores. In addition, for simplicity, the surface-grafted PAA molecules are assumed to have negligible effect on the surface roughness.

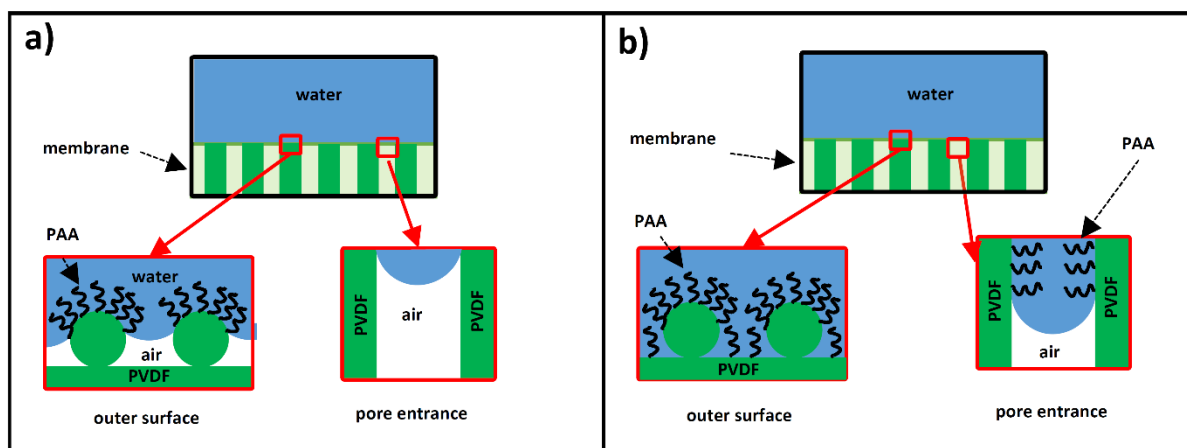


**Figure 6.1:** Schematic illustrations of a) **Model 1**, where only the top surface of the membrane is partially grafted with PAA molecules; and b) **Model 2**, where the top surface of the membrane is fully grafted by PAA molecules and the internal surface of the pores is grafted by PAA down to a certain depth (below the membrane surface facing the feed). For both schematics, the green circles on top of the outer surface represent the nodular roughness feature of the membrane. Close-up images on bottom have ~nm dimension scale.

### 6.3. In-air-water contact angle of the proposed models:

The Cassie's equation can be employed to obtain a relationship for the in-air water contact angle of both membranes (**Models 1** and **2**). Schematics of a water droplet on the membranes are shown in **Figures 6.2a** and **b** for **Models 1** and **2**, respectively. Here, for simplicity, the membranes are assumed to be consisted of two types of surfaces, namely the part of top surface with roughness features and the interfaces at the pore entrances. The surface fraction of each portion is denoted as  $f_{top}$  and  $f_{pore}$ , respectively. In addition, the fraction of the PAA-grafted portion and the fraction of the liquid interfaces with phases other than PAA (air, oil, water) at the top surface are denoted as  $f_{PAA}$  and  $f_{top\ liquid}$ , respectively. In all of the derivations in this chapter, it is assumed that  $f_{top} + f_{pore} = 1$  and  $f_{PAA} + f_{top\ liquid} = 1$ . In other words, it is assumed that the fraction of each surface is equal to its vertical projection. Although this assumption is not true in general [225], it can be employed for a semi-quantitative analysis of the wettability of the model surfaces.

In **Model 1**, the top of the roughness features is in contact with water and the wetting state obeys Cassie-Baxter regime. In addition, it is assumed that the liquid entry pressure into the pores is high enough so that the water meniscus is stable near the pore entrances. Therefore, for the in-air contact angle of water ( $\theta_{w,total}$ ) in **Model 1**, Cassie's equation yields:

$$\cos \theta_{w,total} = f_{top} \cos \theta_{w,top} + f_{pore} \cos \theta_{w,air} \quad \text{Equation 6.1}$$

Where,  $\theta_{w,top}$  and  $\theta_{w,air}$  are in-air contact angles of water on the top surface and on air. Since water does not spread in air it can be assumed that  $\theta_{w,air} = 180^\circ$  and thus  $\cos \theta_{w,air} = -1$ . In addition, since the top surface of the membrane is governed by Cassie's law:

$$\cos \theta_{w,top} = f_{PAA} \cos \theta_{w,PAA} + f_{PVDF} \cos \theta_{w,air} \quad \text{Equation 6.2}$$

Where,  $f_{PAA}$  and  $f_{PVDF}$  are the surface fractions of the PAA-grafted and the bare portion of the roughness features on the top surface of the membrane in **Model 1**, and  $\theta_{w,PAA}$  is the in-air water contact angle of a flat and smooth PAA-grafted surface. Similar to above,  $\cos \theta_{w,air} = -1$ . Since  $f_{top} + f_{pore} = 1$  and  $f_{PAA} + f_{PVDF} = 1$ , by substituting **Equation 6.2** into **Equation 6.1**, we obtain:

$$\cos \theta_{total} = f_{top} f_{PAA} (\cos \theta_{w,PAA} + 1) - 1 \quad \text{Equation 6.3}$$

Therefore, for  $\cos \theta_{total} \leq 0$  the following relationship should hold:

$$f_{top} f_{PAA} \leq \frac{1}{(\cos \theta_{w,PAA} + 1)} \quad \text{Equation 6.4}$$

In **Model 2**, the PAA chains cover the top surface as well as a portion of the internal surface of the pore walls. Therefore, the top surface is fully in contact with water (in Wenzel state). However,

the calculation of the water contact angle for this model is not straightforward, and the difference between the Laplace pressures of the top of the test droplet and that of the water capillary in the pores should be accounted for in order to obtain the correct water contact angle. However, for simplicity, it is assumed that at the pore entrances, the test liquid (water) comes into contact with itself and the contact angle of water with itself is zero. Accordingly, for the in-air water contact angle ( $\cos \theta_{w,total}$ ) of **Model 2**, we have:

$$\cos \theta_{w,total} = f_{top} \cos \theta_{w,top} + f_{pore} \cos \theta_{w,water} \quad \text{Equation 6.5}$$

Here,  $\theta_{w,water}$  is assumed as the contact angle of water with itself which is equal to zero. For the top surface, since the test liquid can fully penetrate the roughness features, the in-air water contact angle ( $\theta_{w,top}$ ) can be described using Wenzel's equation:

$$\cos \theta_{w,top} = R_f \cos \theta_{w,PAA} \quad \text{Equation 6.6}$$

In which  $\theta_{w,PAA}$  is the in-air water contact angle of a flat and smooth PAA-grafted surface, and  $R_f$  is the roughness factor (the ratio of the true area to the vertically projected area of the surface,  $R_f \geq 1$ , and  $-1 \leq R_f \cos \theta_{w,PAA} \leq 1$ ).

Similar to above,  $\cos \theta_{w,water} = 1$ , and  $f_{top} + f_{pore} = 1$ . Therefore, by substituting **Equation 6.6** into **Equation 6.5**,  $\cos \theta_{total}$  is obtained as:

$$\cos \theta_{w,total} = f_{top}(R_f \cos \theta_{w,PAA} - 1) + 1 \quad \text{Equation 6.7}$$

Since the maximum of  $R_f \cos \theta_{PAA}$  is equal to 1, the right hand side of **Equation 6.7** is always positive. Therefore, **Model 2** cannot lead to a membrane with an in-air contact angle of more than  $90^\circ$  ( $\cos \theta_{w,total} \leq 0$ ).

Combining with the in-air contact-angle results obtained in this study (**Figure 5.4** in **Chapter 5**), it can be hypothesized that the PVDF-PAA membranes prepared in this study can be described by **Model 1**.

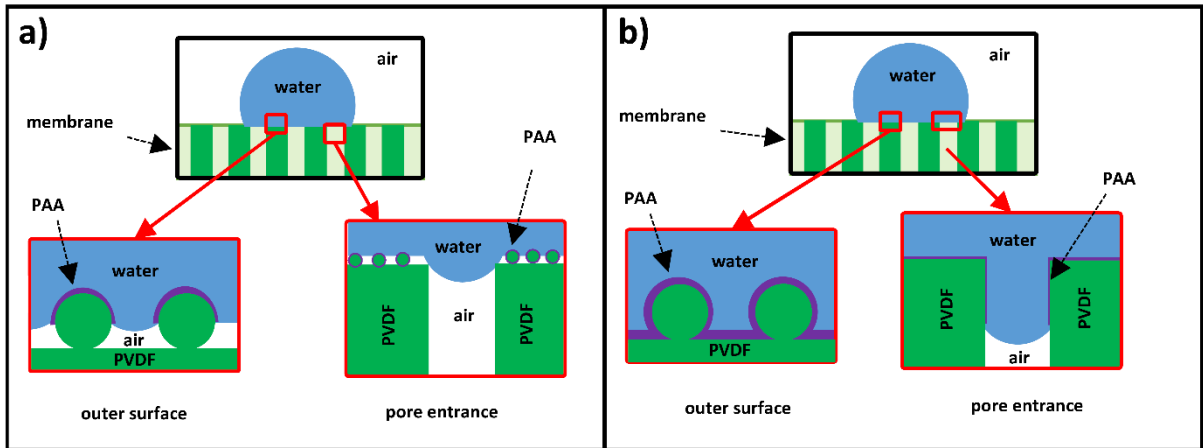


**Figure 6.2:** In-air water contact angle of the surfaces of PVDF-PAA membranes according to a) **Model 1**, and b) **Model 2**. The PAA-grafted region is shown as a smooth layer for simplicity (in violet colour)

#### 6.4. Underwater oil contact angle of the proposed model surfaces

The underwater oil contact angle of the proposed models can be calculated in a similar manner as its in-air water contact angle using a combination of Cassie's and Wenzel's equations. However, here, each of the proposed model can show a different behaviour depending on the phases that are trapped in the roughness features of the top surface, the wetting state of the top surface, and the pre-existing phase inside the pores. For instance, for **Model 1**, apart from the PAA-grafted portion of the top surface, the oil droplet can come into contact with one of the phases, i.e., air, water, or the solid-PVDF phases, creating three different cases/scenarios for the top surface. In addition, in the pore entrances, the oil droplets can come into contact either with air or with pre-existing water trapped in between the air and the oil droplet creating two different cases for the pore entrances. These cases create a total of six different scenarios for **Model 1**. Conversely, **Model 2** can only accommodate the Wenzel state on the top surfaces, because its top surface is fully covered with PAA ( $f_{PAA} = 1$ ). It also involves one case for the pore entrances with water being the phase in contact with the oil droplet. Therefore, only one scenario will be analysed for **Model 2**.

For the mentioned scenarios, the relationship for their underwater oil contact angle ( $\cos \theta_{o,total}$ ) is calculated in **Table 6.1** as a function of the surface fraction of the top of the membrane surface ( $f_{top}$ ), surface fraction of the PAA grafted portion on the top of the membrane surface ( $f_{PAA}$ ), underwater oil contact angle of the PAA ( $\cos \theta_{o,PAA}$ ), and underwater oil contact angle of the PVDF ( $\cos \theta_{o,PVDF}$ ) (where applicable). In all of the calculations, when applicable, it is assumed that oil completely spreads on water with  $\cos \theta_{o,water} = 1$ , and that oil does not spread on its interface with air ( $\cos \theta_{o,PAA} = -1$ ) [147]. The relationships for  $\cos \theta_{o,total}$  as well as other details

about each model and scenario are presented in **Table 6.1**. In addition, detailed derivation for the underwater oil contact angles of “**Model 1-Scenario 1**” as well as **Model 2** are presented in **Appendix A**.

Based on the calculated relationships for  $\cos \theta_{o,total}$  in **Table 6.1**, it is possible to determine whether the oil droplet would spread on the membrane under each condition. For this purpose, the literature data were employed for approximating the values of  $\theta_{o,PAA} \sim 150^\circ$  [226, 227] and  $\theta_{o,PVDF} \sim 40^\circ$  [6, 7, 14, 17, 18], respectively. It should be noted that for PVDF, the literature data are related to porous and rough membrane surfaces which may deviate significantly from the intrinsic underwater oil contact angle for this polymer. However, this value can be used for the purpose of the current qualitative analysis. In addition, the roughness factor ( $R_f$ ) for Wenzel’s equation in **Model 2** is assumed to be equal to 1.1 to ensure that the assumption of the Wenzel state is physically valid. Larger values of  $R_f$  can lead to a  $\cos \theta_{o,PAA}$  value smaller than -1, which means that the Wenzel state cannot describe these systems with higher roughness factors.

**Table 6-1:** The underwater oil contact angle of the membranes according to the proposed models under different scenarios. The phases on the top surface and in the pores refer to the interfaces of the mentioned phases with oil.

Model	Scenario	Top Surface Phases	Pore Entrance Phase	$\cos \theta_{o,total}$
1	1	PAA-air	air	$f_{top} f_{PAA} (\cos \theta_{o,PAA} + 1) - 1$
	2	PAA-water	air	$f_{top} (f_{PAA} (\cos \theta_{o,PAA} + 1) + 2) - 1$
	3	PAA-PVDF	air	$f_{top} (f_{PAA} (\cos \theta_{o,PAA} - \cos \theta_{o,PVDF}) + 2) - 1$
	4	PAA-air	water	$f_{top} (f_{PAA} (\cos \theta_{o,PAA} + 1) - 2) + 1$
	5	PAA-water	water	$f_{top} f_{PAA} (\cos \theta_{o,PAA} - 1) + 1$
	6	PAA-PVDF	water	$f_{top} f_{PAA} (\cos \theta_{o,PAA} - \cos \theta_{o,PVDF}) + 1$
2	1	PAA	water	$f_{top} (R_f \cos \theta_{o,PAA} - 1) + 1$

The schematics of each model and scenario as well as the wettability phase diagrams plotted in terms of  $\cos \theta_{o,total}$  vs.  $f_{top}$  and  $f_{PAA}$  are presented in **Figures 6.3** and **6.4** for **Model 1**, and in **Figure 6.5** for **Model 2**. In the mentioned figures, the oleophobic regions with  $\cos \theta_{o,total} < 0$ , and the oleophilic regions with  $\cos \theta_{o,total} \geq 0$  were shown in red and blue, respectively.

As observed from **Figure 6.3b**, “**Model 1-Scenario 1**” leads to underwater oleophobic states for all combinations of  $f_{top}$ , and  $f_{PAA}$ . This is an important result, because it implies that a hydrophobic surface can become underwater oleophobic if the top of the surface roughness features is covered with hydrophilic compounds, and the rest can maintain a stable air-water

interface. Similar surfaces have been discovered in nature that show superior resistance against fouling in marine environments [228]. In addition, in **Scenarios 2 and 3 (Figures 6.3d and f)**, an increase in  $f_{top}$  at low  $f_{PAA}$  leads to a transition from oleophobic to oleophilic state. This is due to the effect of the oil-water (in **Scenario 2**) and oil-PVDF (**Scenario 3**) interfaces on the top surface of the membrane which allow the spreading of oil. This shows that maintaining a stable Cassie-Baxter state (involving oil-PAA and oil-air interfaces) on the top surface is crucial for the membrane in maintaining its underwater oleophobicity.

As shown in **Figures 6.4b, d, and f**, the presence of water in the pores of the membrane in **Model 1 (Scenarios 4, 5, and 6)** changes the behaviour of the membrane making it more prone to oleophilic behaviour at low  $f_{top}$  (i.e., high portion of the pores). Similar to above, the spreading of oil on oil-water interfaces leads to a better spreading of the oil droplets on the membrane surface in these scenarios. In **Scenarios 5 and 6 (Figures 6.4d, and f)**, the oleophobic region becomes limited to high  $f_{top}$  and  $f_{PAA}$  due to the easier spreading of oil on oil-water (in **Scenario 5**) or oil-PVDF (in **Scenario 6**) interfaces on the top surface of the membrane. The behaviour of **Model 2 (Figure 6.5)** is essentially similar to the **Scenario 5** of **Model 1** at  $f_{PAA} = 1$ , becoming underwater oleophobic at  $f_{top} > 0.5$ .

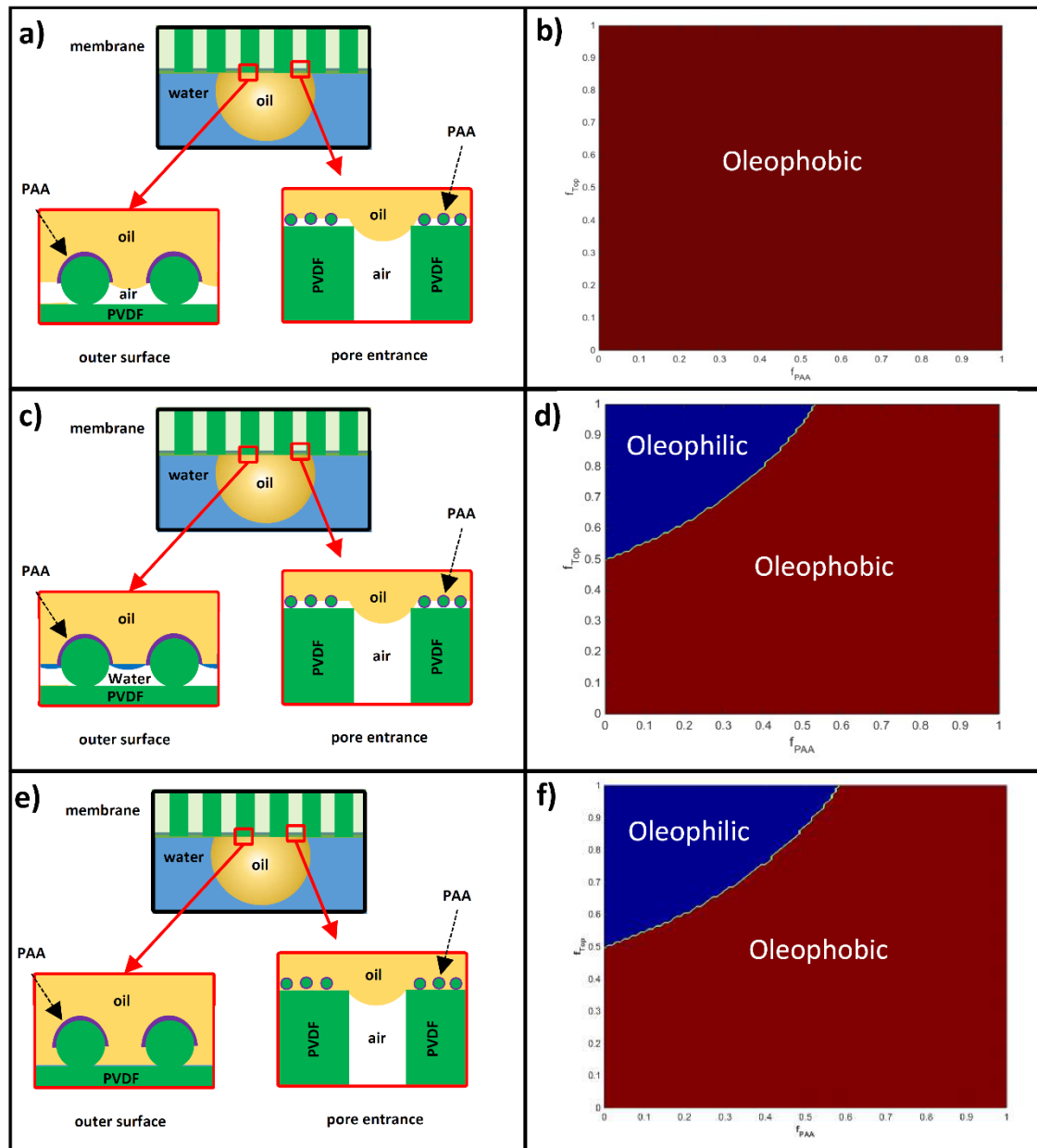


**Figure 6.3:** The schematic presentation of the underwater oil contact angle of PVDF-PAA membrane and the wettability phase diagrams/plots of  $\cos \theta_{o,total}$  as a function of  $f_{top}$  and  $f_{PAA}$  according to **Model 1-Scenarios 1** (a and b), **2** (c and d), and **3** (e and f). The region coloured in red shows the combinations of  $f_{top}$  and  $f_{PAA}$  with  $\theta_{o,total} > 90^\circ$ , while the blue region show the combinations leading to  $\theta_{o,total} \leq 90^\circ$ .



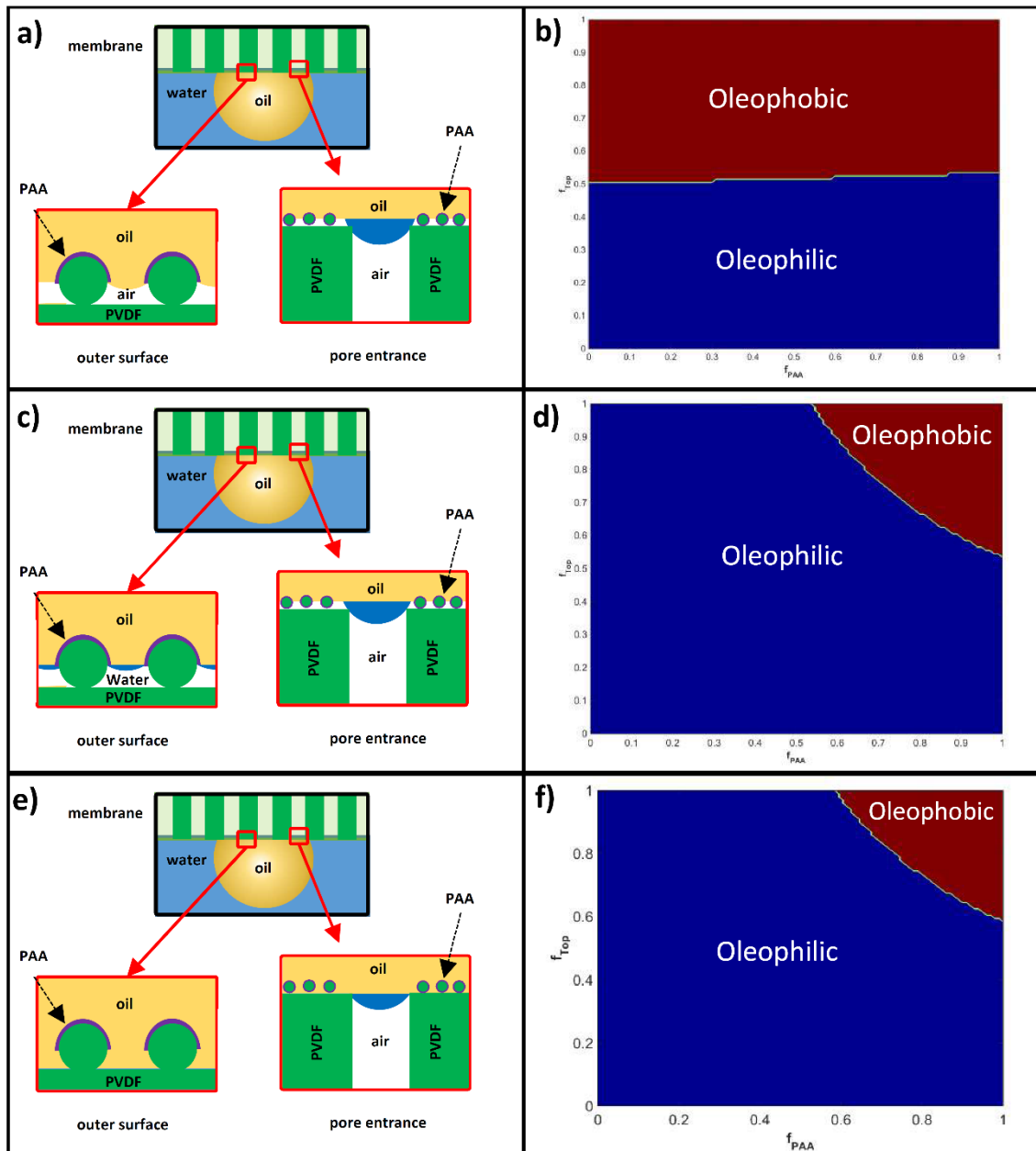


**Figure 6.4:** The schematic presentation of the underwater oil contact angle of PVDF-PAA membrane and the wettability phase diagrams/plots of  $\cos \theta_{o,total}$  as a function of  $f_{top}$  and  $f_{PAA}$  according to **Model 1-Scenarios 4** (a and b), **5** (c and d), and **6** (e and f). The region coloured in red shows the combinations of  $f_{top}$  and  $f_{PAA}$  with  $\theta_{o,total} > 90^\circ$ , while the blue region show the combinations leading to  $\theta_{o,total} \leq 90^\circ$ .

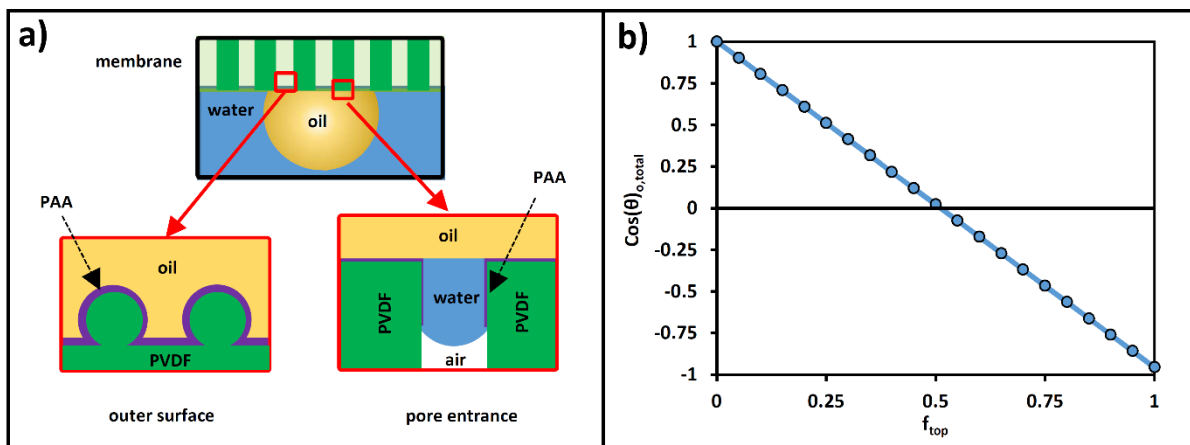


**Figure 6.5:** The schematic presentation of the underwater oil contact angle of PVDF-PAA membrane according to **Model 2** (a). The plot of  $\cos \theta_{o,total}$  as a function of  $f_{top}$  for **Model 2** as presented in Table 6.1 (b). The surface becomes underwater oleophobic with  $\theta_{o,total} \geq 90^\circ$  at  $f_{top} \geq 0.5$ .

In accordance with **Model 1**, as suggested by the SEM results obtained in **Chapter 5** (**Figure 5.4**), the PAA grafting has mainly taken place on the top of the surface asperities in the PVDF-PAA membrane. In addition, as suggested by the underwater oil adhesion experiments (**Figure 5.7**), this membrane has a high underwater oil contact angle in all of the tested conditions in **Section 5.3**. Therefore, the theoretical analysis presented above is consistent with our experimental observations. However, the modelling approach employed above is overly simplified and does not consider other effects such as the hydration and expansion of the PAA chains/brushes, electrostatic interactions between the PAA molecules and the oil-water interface, multicomponent surface energies, and the Laplace pressure differences between the capillary pores and the membrane top surface. In addition, the effects of salinity response of the PAA molecules as well as the effect of salinity on the surface tension of water is neglected in the above discussions. For instance, the relationships for the  $\cos \theta_{o,total}$  of **Model 1** predict that the membrane can transition from underwater oleophilic to oleophobic depending on whether there is trapped water inside the roughness features on the top surface, or near the pore entrances. As observed in **Section 5.3**, at low salinities (Milli-Q water and 0.001 M NaCl), the oil droplets suddenly attached the membrane upon retraction, and later continued to penetrate the membrane. The increase in the surface tension of water due to the increase in the salinity can lead to a shallower level of liquid penetration into the roughness features on the top surface of the membrane as well as the pores. This can lead to a switch in the underwater oleophobicity of the membrane according to the above analyses. This change can roughly be analogized by a change from **Scenarios 2** to **1** or from **Scenarios 5** to **3**. The snapshots taken from the "contact" stage of the oil droplet with the membrane surface under Milli-Q water and under 0.001 M NaCl show a high contact angle for PVDF-PAA (**Figure 5.7**) despite the droplet being pulled onto the

membrane. Therefore, these observations imply that other factors should be investigated further to better understand the underwater oleophobicity and its relevance to oil wetting in MD.

Another limitation of the proposed model, especially for real wastewaters, is the need for obtaining the individual contact angle values of the liquid medium as well as those of the oil droplets on the grafted and pristine sections of the membrane. These data are usually difficult to measure experimentally, and can only be calculated to a limited extent using theoretical values for the pure compounds. This could pose a serious challenge in real oily wastewaters which often contain complex combinations of different compounds.

Finally, in practical applications, some of the proposed scenarios can take place simultaneously on one membrane (on different regions of the membrane surface), leading to inconsistent wetting behaviour. In addition, wetting transitions can occur between these scenarios which makes the analysis even more complex.

Overall, despite its limitations and shortcomings of the proposed simplified models, they can be used as new steps toward understanding the more complex mechanisms in the oil contamination of membranes, by providing preliminary advice as to what surface properties might be favourable for underwater oleophobicity.

## 1.5 Conclusions

In this chapter, two models were proposed for the structure of the as-developed PVDF-PAA membrane in order to understand its wetting properties in the context of oily saline water. In **Model 1**, it was assumed that the PAA brushes were only grafted on the top regions of the surface roughness features of the membrane, while in **Model 2**, the PAA chains were assumed to cover the entire top surface of the membrane as well as a portion of the internal surface of the pores. The calculations of the in-air water contact angle of the proposed models showed that **Model 1** is better aligned with the experimental results obtained for this membrane in **Chapter 5**. The underwater oil contact angle of the proposed models was calculated using a combination of simplifying assumptions under six scenarios for **Model 1** and one scenario for **Model 2**, and the resulting underwater oleophobicity phase diagrams were plotted as a function of  $f_{top}$  and  $f_{PAA}$ . It was found that apart from the interfaces that the oil droplets form with the PAA patches, the interfaces formed between oil and one of the three phases consisting of air, bare (untreated portion) PVDF, or water can significantly affect the underwater oleophobicity of the PVDF-PAA membrane. Among the investigated scenarios, the scenario with oil-air interfaces (**Model 1-Scenario 1**) showed underwater oleophobicity over the entire range of  $f_{top}$  and  $f_{PAA}$ . However, for other scenarios, depending on whether the oil droplet contacted water or bare PVDF, the underwater oleophobicity was limited to a region in the oleophobicity phase diagrams. Comparison of these findings with the experimental data of the underwater adhesion results in

**Chapter 5** showed that despite the general agreement between the two, other factors should also be considered for a deeper understanding of these surfaces such as the hydration and expansion of the PAA brushes, and electrostatic interactions between the PAA molecules and the oil-water interface, which deserve a further study. Nevertheless, the proposed models can potentially be used as a qualitative tool in explaining and understanding the behavior of Janus membranes and in designing new oil-resistant membranes.

# Chapter 7 Analysing the wetting behaviour in membrane distillation of oily waters in real-time by *in-situ* electrochemical impedance spectroscopy (EIS)

---

## 7.1 Introduction

Researchers have successfully developed materials that allow MD to treat oily waters, but the underlying beneficial mechanisms need to be better understood. Accordingly, the aim of this chapter is to analyse the oil wetting in MD membranes using real-time *in-situ* EIS measurements. In this chapter, the time-resolved full frequency sweep electrochemical impedance spectroscopy (EIS) measurements (detailed in **Chapter 3**) will be discussed to study the oil wetting behaviour of two MD membranes: a commercial hydrophobic PVDF (mean pore size = 0.2  $\mu\text{m}$ ), and the PVDF-PAA membrane developed using **Approach 2** (described and characterized in **Chapters 3, 5, and 6**).

Due to the complexity of the equivalent circuits in MD, a deterministic analysis of wetting and fouling in MD is a challenging task. Thus, here a new approach is proposed to tackle the problem from a different angle, i.e., obtaining valuable information from the system by observing the changes in the obtained EIS data and comparing them to theoretical circuit models.

The current chapter aims at performing a holistic analysis of the EIS results by observing the evolution of frequency response of the model MD systems under three different scenarios (*i.e.*, with pristine PVDF membrane with feed containing salt only; and respective pristine and modified PVDF membranes with a feed containing salt and oil) over the course of twenty-hour experiments. Accordingly, first, the results of the visual observation on the MD and *in-situ* EIS measurements will be discussed in **Section 7.2** for the three tested systems, namely, PVDF-salt, PVDF-salt-oil, and PVDF-PAA-salt-oil systems. Next, the equivalent circuit for the system will be developed in **Section 7.3**. Finally, the EIS data obtained on PVDF-salt-oil, and PVDF-PAA-salt-oil systems will be fitted by the developed equivalent circuits in **Section 7.4** to analyse the changes in the system parameters and their correlation to the changes observed during MD of these systems.

## 7.2 Visual observation of the real-time *in-situ* EIS measurements

Visual observation is an effective holistic analysis method that focuses on the general features of the obtained EIS data. Depending on the quality of the observed data in different frequencies, visual observation is an important first step before applying data reduction methods, as it can

reveal information about the changes in various features of the system over time. In order to better understand the EIS data, and their relevance to MD, a side-by-side comparison of the MD and EIS results is shown in **Figure 7.1a-f**. As can be observed in **Figure 7.1a**, the flux of the pristine PVDF is relatively constant throughout the MD of 0.1M NaCl solution (namely the PVDF-salt system). Concurrently, the Bode plots ( $|Z|$  vs.  $f$ ) in **Figure 7.1d** show no change from the beginning to the end of the MD experiments. It is important to note the noisy nature of the data at  $f < 100$  Hz, which might be related to the high impedance of the system (i.e. the components that are between the electrodes shown in **Figure 3.5** in **Chapter 3**) and the inability of the instrument in resolving the parasitic noise caused by the low current signal passing through the system. The observed noise at low-frequencies will be discussed in more detail in **Section 7.3**. The second column in **Figure 7.1** presents the MD (**Figure 7.1b**) and Bode plots (**Figure 7.1e**) at different times for the PVDF-salt-oil system. As can be observed from the MD data, the permeate flux gradually drops from 16 to 5.7 kg/(m<sup>2</sup>.h) in the first 6 h of the experiment. In addition, it can be observed from the MD results that the permeate EC is almost constant at 1.7  $\mu$ S/cm from the beginning of the experiment until  $t=5$  h, gradually increasing afterward and reaching 61  $\mu$ S/cm at the end of the experiment. The observed increase in the permeate EC suggests the occurrence of a breakthrough of the feed solution across the membrane into the permeate solution, which is a sign of membrane wetting. These changes manifest themselves in the EIS results as an overall reduction in the value of the impedance modulus ( $|Z|$ ) over time. An interesting feature of the EIS Bode graph for this system (**Figure 7.1e**) is the significant reduction of  $|Z|$  at low-frequency regions as compared to that in the high-frequency ranges. The changes in the impedance at the low-frequency region of the  $|Z|$  plots imply the occurrence of changes in the ion transport and diffusive properties of the system, while changes in the high-frequency region are related to the ohmic and charge transfer properties of the system. In addition, a downturn can be observed in the Bode plots of the PVDF-salt-oil system over time with the greatest step occurring between  $t=5$  h and  $t=6$  h, concomitant with the onset of liquid breakthrough across the membrane, suggesting that the decrease in permeate electrical resistance might contribute to the large decrease in  $|Z|$  in the low- $f$  region. Compared to the low- $f$  end of the Bode plots, the value of  $|Z|$  at higher  $f$  changes less significantly, suggesting that the ohmic and capacitive properties of the system are affected less significantly during MD. These properties are related to the electrical double layers (EDLs) formed in the interfaces of solid-liquid (i.e., electrode-feed/permeate solutions, membrane-feed/permeate solutions), liquid-liquid (i.e., oil-water), gas-liquid (i.e., between air bubbles and feed/permeate solutions, and air-water interfaces between the feed/permeate solutions and the dry portion of the membrane pores). The ohmic impedance can be attributed to the electrical resistance of the feed and permeate solutions as well as the membrane impedance. The noise observed in the PVDF-salt system was also observed in the

PVDF-salt-oil system, but diminished upon the onset of wetting after 5 hours. This may be due to the reduction in impedance, which lessens the potential for noise to interfere with the signal.

**Figures 7.1c** and **f** present the MD data and EIS Bode plots for the PVDF-PAA-salt-oil system. As can be observed from the MD data, the permeate flux and EC remained constant during the tested period of 20 h. This suggests the absence of a liquid breakthrough across the membrane, confirming the effect of the PAA surface modification to prevent wetting. The decrease in permeate EC observed for the PVDF-salt system (**Figure 7.1a**) was not observed here, instead, the EC increased slightly, which was attributed to the very low starting EC of the Milli-Q water used in this test ( $\sim 2 \mu S/cm$ ), indicating that predominantly distilled water permeated the membrane and a very salt high rejection ( $\sim 99.98\%$  based on the EC values assuming a constant feed EC value of  $10 mS/cm$ ) obtained over the entire run. The Bode plots of the PVDF-PAA-oil system at different times (**Figure 7.1f**) show a slight downturn in the low- $f$  region and a relatively less pronounced change in the high- $f$  region. The changes in the low- $f$  region for the PVDF-PAA-salt-oil system are more significant as compared to the changes in the same region of the PVDF-salt system. However, these changes are less significant in PVDF-PAA-salt-oil system as compared to that of the PVDF-salt-oil system. These observations indicate interesting effects in each scenario, and warrants further analysis.

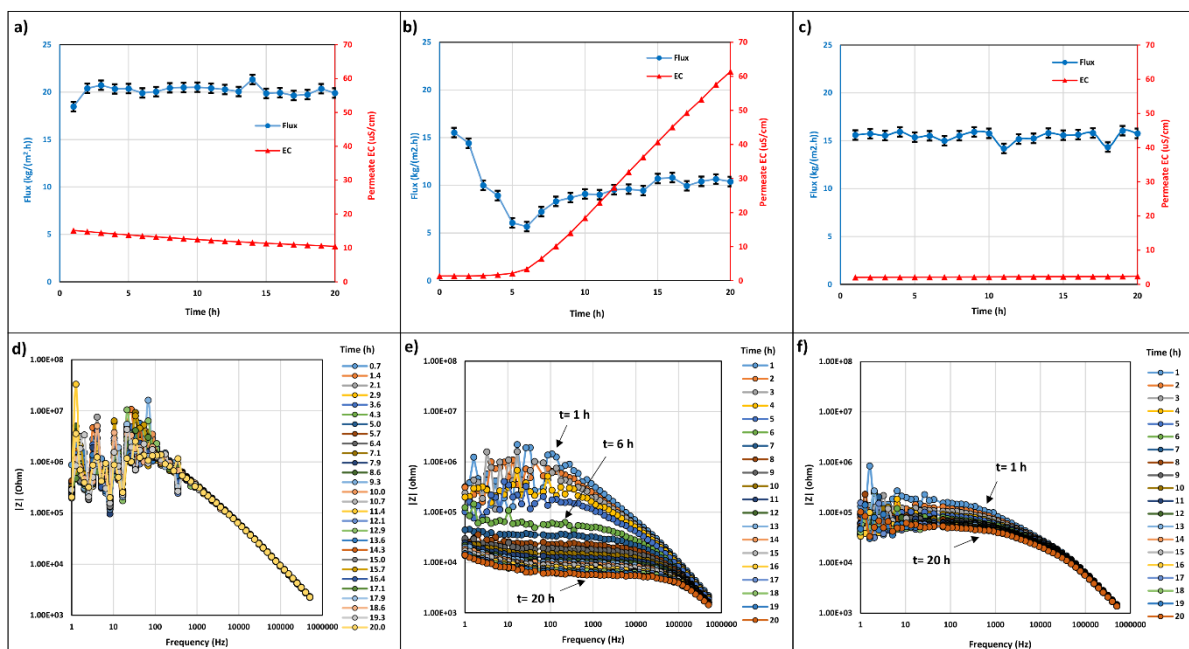


**Figure 7.1.** MD results and corresponding real-time Bode plots (impedance modulus ( $|Z|$ ) vs. different frequencies) at different times for the three tested systems: PVDF-salt: a) and d); PVDF-salt-oil b) and e); PVDF-PAA-salt-oil c) and f). Feed and permeate inlet temperatures were constant at  $60^{\circ}C$  and  $20^{\circ}C$ , and

the crossflow velocity of both feed and permeate was 3.13 m/min. The oily dispersion contained 0.1 % (v/v) dodecane and 0.1 M NaCl in water. The saline solution contained 0.1 M NaCl in water.

For a better observation of the changes in the impedance of the studied systems during MD, the values of  $|Z|$  at 7 selected frequencies ranging from 1 Hz to 500 kHz are shown as a function of time for each system in **Figure 7.2a-c**. In addition, the “normalized  $|Z|$ ” corresponding to each graph is calculated by dividing  $|Z|$  at each time to the value of  $|Z|$  at  $t=1$  h (shown in **Figures 7.2d-f** and **Figure B1a-c** in **Appendix B**). As can be observed in **Figures 7.2a** and **d**, the value of  $|Z|$  for the PVDF-salt system remains almost constant throughout the experiment at all of the selected frequencies. Both the  $|Z|$  and “normalized  $|Z|$ ” vs. time plots for the PVDF-salt-oil system (**Figures 7.2b, 7.2e, and B1b** in **Appendix B**) show a decline in impedance at all of the sampled frequencies over time. Similar to what was observed in the Bode plots, the decline in the impedance is more significant at low frequencies as compared to the high frequencies. At  $f=1.0$  Hz, 10 Hz, 1.1 kHz, and 9.3 kHz, the value of  $|Z|$  decreases by 1-3 orders of magnitude; while for  $f=120$  kHz and 500 kHz, this decrease is less than one order of magnitude. Similar to what was discussed in the analysis of Bode plots (**Figure 7.1d-f**), the difference in the decline in  $|Z|$  among different frequencies could be attributed to the changes of the system associated with diffusive and ion transport properties of the PVDF-salt-oil system (possibly due to oil wetting). As can be seen in the presented graphs (**Figures 7.2b** and **e**), an increase in  $|Z|$  at 10 Hz is observed from  $t=0$  to  $t=3$  h, followed by a decrease at  $t>3$  h. This extremum might be related to the adhesion of the oil droplets onto the membrane, and onset of the liquid breakthrough process. However, more evidence is needed to confirm this hypothesis.

The  $|Z|$  and “normalized  $|Z|$ ” plots for the PVDF-PAA-salt-oil system (**Figures 7.2c** and **f**) show a reduction in impedance at low to mid frequencies (1.0 Hz, 10 Hz, 110 Hz, and 1.1 kHz); while the decrease at higher frequencies (9.3 kHz, 120 kHz and 500 kHz) is less significant. Considering the fact that the permeate EC measured using the EC meter did not change during MD, the observed decline in the impedance of this system could be attributed to the changes in EDL properties in the feed side possibly caused by the oil droplets adjacent to the membrane and/or electrode surface. To understand the underlying mechanism of such phenomenon, additional information is needed on the adhesion of the oil droplets on the membrane and electrode surfaces as well as the EDL properties in the oil-water interfaces. Such information is not available in the current study but highlights another direction for applying EIS to better understand behaviour of membranes in MD and could be subject of a future work.

The comparison of the  $|Z|$  and “normalized  $|Z|$ ” plots of the PVDF-salt-oil (**Figures 7.2b** and **e**) and PVDF-PAA-salt-oil (**Figures 7.2c** and **f**) systems can be utilized to identify the attributes of the low- $f$  and high- $f$  regions in the presence of a wetting substance (oil) when wetting did, or did



not, occur. At the low- $f$  region, the observed impedance for the PVDF-salt-oil system shows a decline by about two orders of magnitude, while the impedance of the low- $f$  region in PVDF-PAA-salt-oil decreases less than one order of magnitude. Considering that no significant EC rise was observed in the PVDF-PAA-salt-oil system the decrease in  $|Z|$  of this system would mean that the observed changes were not related to wetting, or that wetting also had taken place in this system, but the rate of EC rise has been too slow to show any effect in the permeate EC, which was measured in the permeate container and was affected by the vapour flux through the membrane. At the high- $f$  range, the change in the properties of both systems are insignificant and cannot be used to distinguish between a wetting and nonwetting scenario. Although it is usual practice to select a frequency at the mid- to high- $f$  range as a probing frequency for example 10 kHz to 1 MHz [19, 75], our results show that such frequency might not conclusively help identify wetting in an MD system.

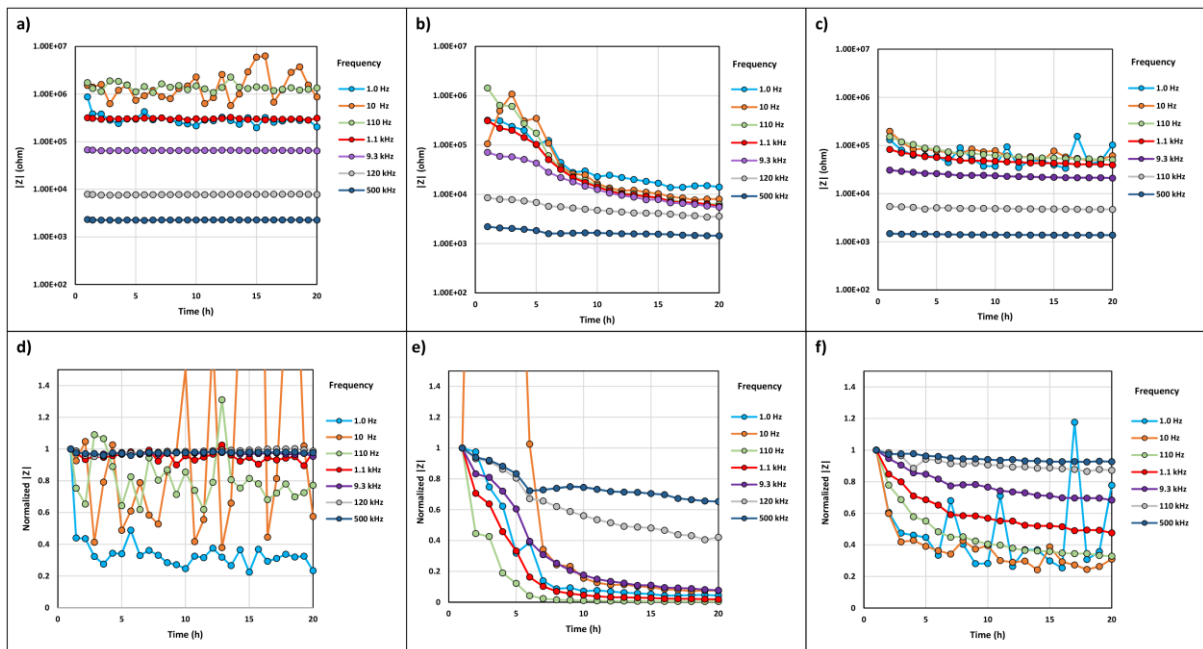


**Figure 7.2:** The impedance modulus ( $|Z|$ ) (top row) and the normalized impedance modulus ( $|Z|/|Z_1|$ ) (where  $|Z_1|$  is the value of impedance at  $t=0$  h (bottom row)) at different frequencies vs. time for PVDF-salt: a) and d); PVDF-salt-oil: b) and e); PVDF-PAA-salt-oil: c) and f). Feed and permeate inlet temperatures were constant at  $60^\circ\text{C}$  and  $20^\circ\text{C}$ , and the crossflow velocity of both feed and permeate was  $3.13$  m/min. The oily dispersion contained  $0.1\%$  (v/v) dodecane and  $0.1$  M NaCl in water. The saline solution contained  $0.1$  M NaCl in water.

The Nyquist plots for the performed tests are presented in **Figure 7.3a-f** in different magnifications on the positive section ( $Z' > 0$  and  $-Z'' > 0$ ) of each of the respective plots. In addition, the full view of the plots can be observed in **Figure B2a-c** in **Appendix B**.

As can be observed in **Figure 7.3a** and **B2a** (in **Appendix B**), many data points in the Nyquist plots of the PVDF-salt system are scattered and/or fall within the negative sections of the axes ( $Z' < 0$  and/or  $-Z'' < 0$ ). A well-defined curve made up of the data points, decreasing in frequency from the origin, can be observed in the magnified view of the Nyquist plots for this system (**Figure 7.3d**). As the points move away from the origin (decreasing frequency order), the data become more scattered to a point that no coherent trend can be observed (**Figure 7.3a**). The elapsed time has no visible effect on the graphs of this system. The scatter in the data at lowest frequencies, and the presence of data points within the negative regions of the axes suggest the presence of a high level of parasitic noise, possibly due to the low measured current (within the minimum measured range of 100 nA).

The Nyquist plots of PVDF-salt-oil system are shown in **Figures 7.3b, 7.3e, and B2b** (in **Appendix B**). It can be observed in the overall plot (**Figure B2b** in **Appendix B**), this system also contains many data points in the negative region of the  $Z'$  and  $-Z''$  axes. However, the number of data with negative values seem to be smaller than that for the PVDF-salt system, suggesting a lower level of noise in the data. The magnified view of the Nyquist plots for the PVDF-salt-oil system presented in **Figure 7.3b**, similar to the PVDF-salt system, shows a coherent trend starting from the origin (in decreasing frequency order) progressively becoming more scattered only for the first 5 hours. A downturn in the plots develops gradually from  $t=1$  h to  $t=5$ , then from  $t=6$  h the plot begins touching the  $Z'$  axis forming a semi-circle (**Figure 7.3e**). On the later stages of the process, a diffusive tail starts forming and the plots take the appearance of a typical Randle's circuit [229]. With time, the semi-circle section of the plots become smaller in diameter and their inflection point shifts to the left (toward lower  $Z'$ ). Each semi-circle in the Nyquist plots is usually associated with at least one time constant corresponding to a resistor and a capacitor in parallel with each other (a Maxwell-Wagner element). A decrease in the diameter of the semi-circle is then attributed to the reduction in the resistivity of the resistance component of the Maxwell-Wagner element describing the system [230]. Multiple components of our studied system can act as Maxwell-Wagner elements, including, the membrane, and the electric double layers in the liquid-solid interfaces between the electrodes (or membrane) and the feed (or permeate) solutions [182]. The potential physical meaning of these patterns in the EIS data will be discussed later with equivalent circuit analysis.

The Nyquist plots obtained for the PVDF-PAA-salt-oil system are presented in **Figures 7.3c, 7.3f, and B2c** (**Appendix B**). As can be observed, the initial stages of the experiment resemble that of the PVDF-salt and PVDF-salt-oil systems including the effects of noise (**Figure B2c** in **Appendix B**). Over time, the low- $f$  end of the plots (points furthest in order from the origin) go through a downturn (**Figure 7.3c**) gradually reaching a state at which two connected semi-circles can be observed. The shrinkage in the radius of the semi-circles is not enough to show a well-defined

junction point between them. The observation of two semi-circles in the Nyquist plots suggests the presence of at least two time constants (Maxwell-Wagner elements) in the system. Based on the available information about the system, it is not possible to identify the underlying phenomena responsible for creating such effect [182]. Similar to the PVDF-oil-salt system, this element can be associated with the membrane and/or the EDLs on different interfaces of the system [182].

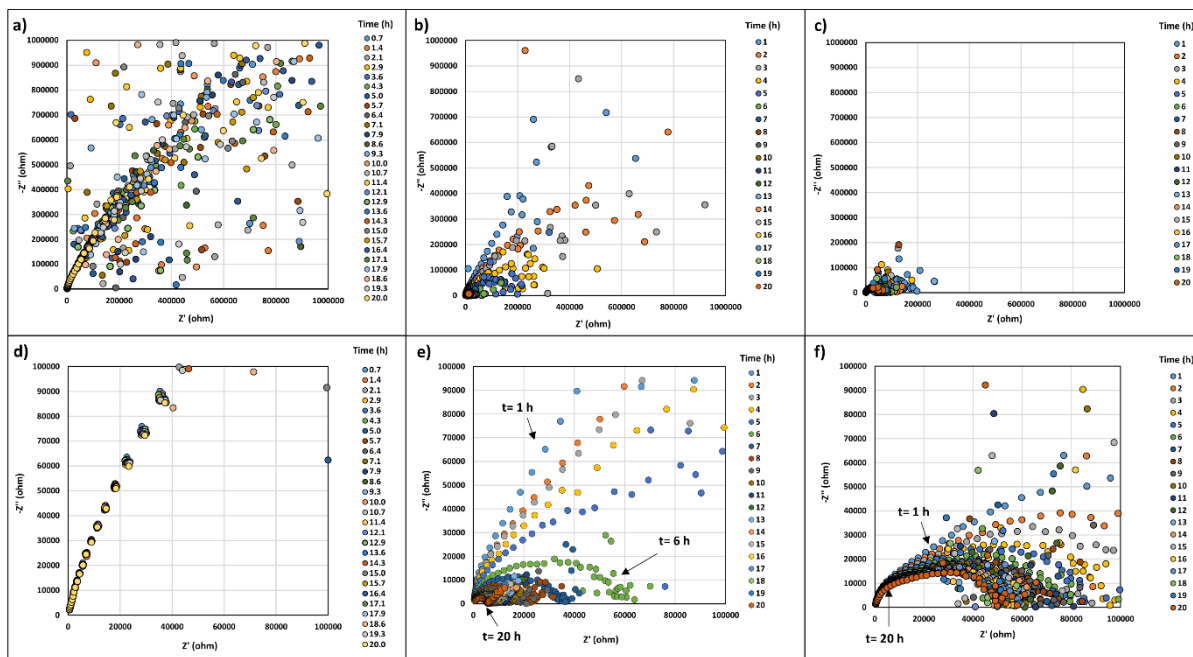
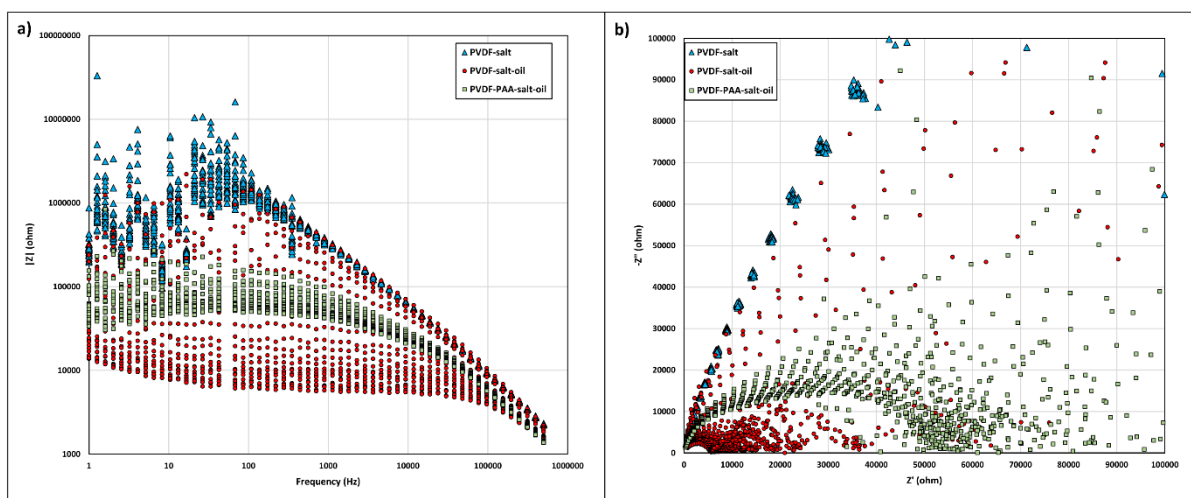


**Figure 7.3:** The positive section of the Nyquist plots at different times for PVDF-salt: a) and d); PVDF-salt-oil: b) and e); PVDF-PAA-salt-oil: and c) and e). Top row shows the plots up to  $Z' = -Z'' = 10^6 \Omega$ , and the bottom row shows the magnified view of the plots up to  $Z' = -Z'' = 10^5 \Omega$ . Feed and permeate inlet temperatures were constant at  $60^\circ\text{C}$  and  $20^\circ\text{C}$ , and the crossflow velocity of both feed and permeate was  $3.13 \text{ m/min}$ . The oily dispersion contained  $0.1 \%$  (v/v) dodecane and  $0.1 \text{ M}$  NaCl in water. The saline solution contained  $0.1 \text{ M}$  NaCl in water.

For a better comparison across the different test conditions, the Bode and Nyquist plots for all of the performed MD tests are plotted in **Figures 7.4a** and **b**, respectively. It can be observed that at the initial stages of the MD process, the Bode and Nyquist plots of the PVDF-salt-oil system are similar to those of the PVDF-salt system in terms of both the values and the shape of the graphs. Over time, the Bode plots of the PVDF-salt-oil system deviate from those of the PVDF-salt plots by going through a large downturn, and their corresponding Nyquist plots exhibit a downturn followed by a change in the shape of the graphs from a large arch to a “semi-circle plus a straight line” toward the later stages of the process.

It can also be observed that the Bode plot of the PVDF-PAA-salt-oil system at  $t=1 \text{ h}$  resembles the Bode plot of the PVDF-salt-oil system at  $t=5 \text{ h}$ . Over time, the Bode plots of the PVDF-PAA-salt-oil system go through a downturn, with the final plot (at  $t=20$ ) situated just above the plot of

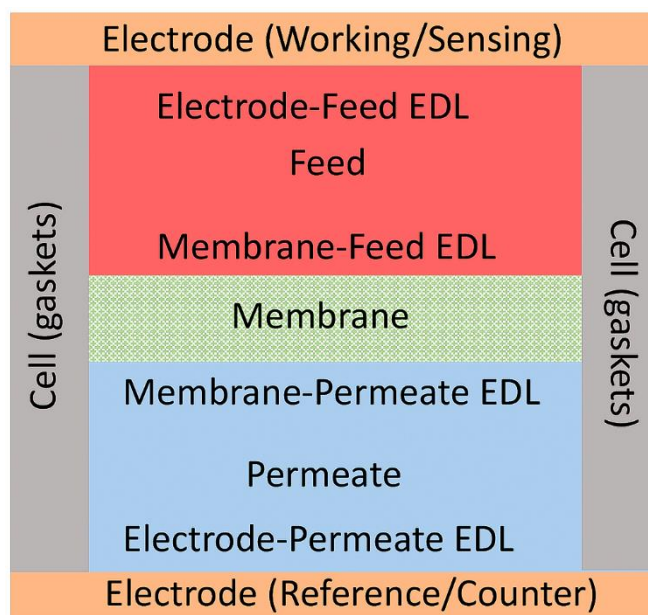
PVDF-salt-oil system at  $t=6$  h. The Nyquist plots of the PVDF-PAA-salt system also go through a downturn forming dual semicircles, but do not go beyond this stage during the 20 h of the experiment, while the Nyquist plots of the PVDF-salt-oil system go through this stage roughly between  $t=5$  h and  $t=10$  h transforming into a single semi-circle with a diffusive tail (a Randle's-circuit-type response [229]). This period of time coincides with the onset of the breakthrough from the feed solution to the permeate solution detected by the EC meter for this system (**Figure 7.1b**), which shows a possible correlation between the transformation of the Nyquist plots and the occurrence of the liquid breakthrough. This correlation is more difficult to notice in the Bode plots, since the shape of these plots is similar across the PVDF-salt-oil and PVDF-PAA-salt-oil systems. In terms of magnitude, the Bode plots of the former system go through a larger decrease in  $|Z|$  over the course of the experiment (20 h) as compared to the latter. In addition, a significant drop in  $|Z|$  occurs in the former system between  $t=5$  h and  $t=6$  h (coinciding with the onset of the breakthrough) enveloping the entire Bode plots of the latter between  $t=1$  h and  $t=20$  h. The physical meaning of the observed changes in the Bode and Nyquist plots for the studied systems and their relationship with the occurrence of wetting will be investigated through equivalent circuit analysis in **Section 7.4**.



**Figure 7.4:** Cross comparison of the Bode (a), and Nyquist (b) plots of the studied systems over the entire course of MD (20 h).

### 7.3 Analysis of static EIS measurements and development of equivalent circuits

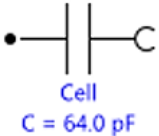
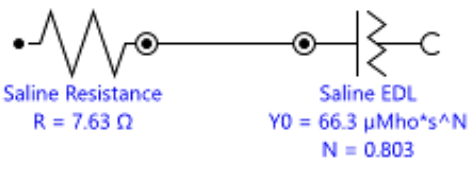
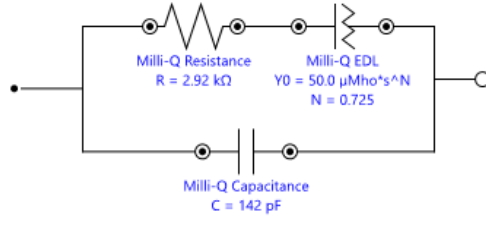
An equivalent circuit model was developed for the MD systems under study to analyse the real-time MD-EIS results. A simplified demonstration of the different physical elements of the system is presented in **Figure 7.5** showing four EDLs, two liquid media, a membrane and the rubber gaskets depicted in **Figure 3.5** in **Chapter 3**. Each component was simulated by their corresponding circuit elements based on the static EIS tests on the MD cell alone (no pumps or tubing).



**Figure 7.5:** Schematic presentation of the physical elements involved in the measured electrical properties of the system for EIS equivalent circuit analysis.

The impedance response of the gaskets (not proportionally shown in **Figure 7.5** was modelled by a single capacitor in the equivalent circuit models and was assumed to be constant for all of the static EIS and dynamic MD-EIS tests. The equivalent circuit models of the gaskets and the remaining active components of the cell were analysed and summarised in **Table 7.1**. The detailed analysis and EIS curve fittings can be found in **Appendix B** as indicated in the notes in **Table 7.1**. For the final combined equivalent circuit model, the membrane is modelled using a Maxwell-Wagner element (a resistor in parallel with a capacitor) and the entire cell was considered with all elements developed for the previous components. For developing the full equivalent circuit, the static EIS tests were performed to simulate the conditions of MD under the nonwetted and wetted scenarios, where both involved the feed compartment filled with 0.1M NaCl solution and the permeate compartment filled with Milli-Q water. In the wetted scenario, the membrane was deliberately wetted by dispensing 2-3 droplets of oil (dodecane) directly onto the membrane before the module was assembled and the feed and permeate compartments were filled. The EIS data fitting was performed using the initial guesses obtained from the calculated individual compartments, but was only successful for the wetted system. For the purposes of this study, the values of the parameters obtained for the wetted case were chosen as the initial guesses for curve fittings on the real-time data for both the PVDF-salt-oil and PVDF-PAA-salt-oil systems.

**Table 7-1:** Summary of the modelled circuit components for each model element based on static testing including the proposed combined circuit. The static tests were performed at room temperature without MD.

Model component	Equivalent circuit and element values	Notes
The cell (the gaskets)	 <p style="text-align: center;">Cell C = 64.0 pF</p>	<ul style="list-style-type: none"> <li>• Dry empty cell</li> <li>• Simulated as a capacitor</li> <li>• Fitting in <b>Figure B3</b></li> </ul>
The feed compartment*	 <p style="text-align: center;">Saline Resistance R = 7.63 Ω</p> <p style="text-align: center;">Saline EDL Y0 = 66.3 μMho*s<sup>N</sup> N = 0.803</p>	<ul style="list-style-type: none"> <li>• Feed solution: 0.1M NaCl</li> <li>• Resistor and constant phase element (CPE) for solvent and EDL impedances.</li> <li>• Fitting in <b>Figure B4</b></li> </ul>
The permeate compartment*	 <p style="text-align: center;">Milli-Q Resistance R = 2.92 kΩ</p> <p style="text-align: center;">Milli-Q EDL Y0 = 50.0 μMho*s<sup>N</sup> N = 0.725</p> <p style="text-align: center;">Milli-Q Capacitance C = 142 pF</p>	<ul style="list-style-type: none"> <li>• Milli-Q water only</li> <li>• New capacitor introduced into compartment due to high solution resistance</li> <li>• Fitting in <b>Figure B5</b></li> </ul>

<p>The combined system including the membrane</p>		<ul style="list-style-type: none"> <li>• Model only successful with wetted membrane</li> <li>• Fitting in <b>Figure B6</b></li> </ul>
---	--	---

\*The initial guesses for the permeate and feed properties in the was obtained by performing EIS on each of the saline solution and the Milli-Q water separately in the cell without the membrane. Therefore, for data fitting each of the equivalent circuits shown in this table were in parallel with the cell capacitance as shown in **Figures B4** and **B5**.

#### 7.4 Changes in the physical properties of the system during MD measured by real-time EIS.

The data obtained from the real-time MD-EIS tests for PVDF-salt-oil and PVDF-PAA-salt-oil systems were fitted using the combined equivalent circuit proposed in **Table 7.1**. The curve fitting was performed by keeping the feed resistance and CPE parameters constant (apart from the cell capacitance) across all tests. For PVDF-PAA-salt-oil system, the curve fittings were performed on the data obtained over the interval of 5 hours. For the PVDF-salt-oil system, in order to better analyse the system near the breakthrough point of wetting, the curve fitting for the first 10 h of the experiment was performed in one-hour intervals; while for the data after  $t=10$  h, it was only performed at  $t=15$  h and  $t=20$  h. It was also found that the PVDF-salt-oil system circuit proposed in **Table 7.1** could not be successfully fitted to the data after  $t=7$  h, possibly due to the occurrence of wetting, which makes the capacitance element of the permeate redundant. Therefore, to perform the curve fitting on the data after  $t=7$  h, the equivalent circuit was simplified to only contain one resistor-CPE pair to represent the combined properties of all EDLs and solutions involved in the system. The simplified equivalent circuit is shown in **Figure 7.6**. Nevertheless, the data at  $t=8$  and 9 h could not be fitted using either of the original or modified equivalent circuit models. This could be due to the fast rate of the transitions taking place during this time range (from  $t=7$  h to  $t=10$  h).



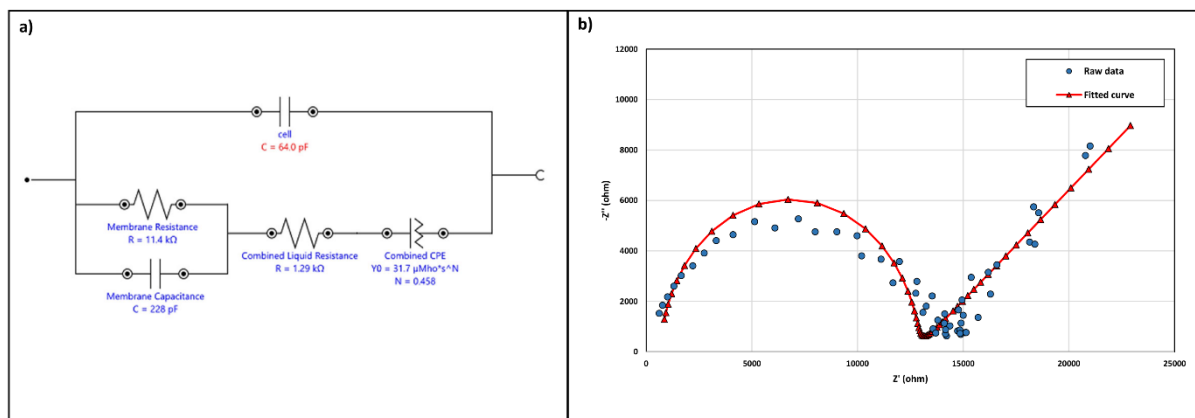


**Figure 7.6:** The equivalent circuit a), and curve fitting results b), on the PVDF-salt-oil system at  $t=10$  h after wetting occurred.

The curve fitting was also attempted on the PVDF-salt systems, but no successful fit was obtained using the combined equivalent circuit model presented in **Table 7.1**. This might be due to the large impedance of the unwetted membrane, the interference from the environment, or the limitations of the fitting algorithm in fitting the parameters with large differences in magnitude.

The values obtained for the membrane resistance and capacitance of the PVDF-salt-oil and PVDF-PAA-salt-oil systems are shown in **Figures 7.7a** and **c**, respectively. The obtained values for membrane resistance and capacitance include the physical properties (i.e., resistivity and dielectric permittivity, respectively) as well as the geometrical aspects (i.e., thickness and effective projected surface area for both resistance and capacitance) of the membrane. The value of the membrane resistance for the PVDF-PAA-salt-oil system decreased from 67.4 k $\Omega$  at  $t=1$  h, to 29.9 k $\Omega$  at  $t=20$  h (**Figure 7.7a**). This decrease might be due the diffusion of solutes from the feed solution (e.g., NaCl leakage via an “imperfect” membrane, or oil transfer by hydrophobic diffusion [231, 232]) through the membrane. The capacitance of the membrane in the PVDF-PAA-salt-oil system remains almost constant throughout the 20 h of the MD process (**Figure 7.7c**).

The resistance of the membrane in the PVDF-salt-oil system goes through a maximum (more accurately, a damped oscillatory behaviour) in the early stages of the experiment followed by a decrease that stabilises at  $t=7-8$  h and a slight decrease until  $t=20$  h (**Figure 7.7a**). The high average membrane resistance prior to the breakthrough (wetting) could possibly be related to the intact membrane and potentially the adhesion of the oil droplets to the membrane surface, which subsequently leads to the breakthrough of the feed liquid through the membrane observed by EC rise starting around 5 hours (**Figure 7.1b**). For the PVDF-salt-oil system, during the initial stages of MD, the membrane capacitance fluctuates within the range of 1 nF to 10 nF (**Figure 7.7c**).



This fluctuation could be related to the noise discussed earlier associated with higher initial impedances.

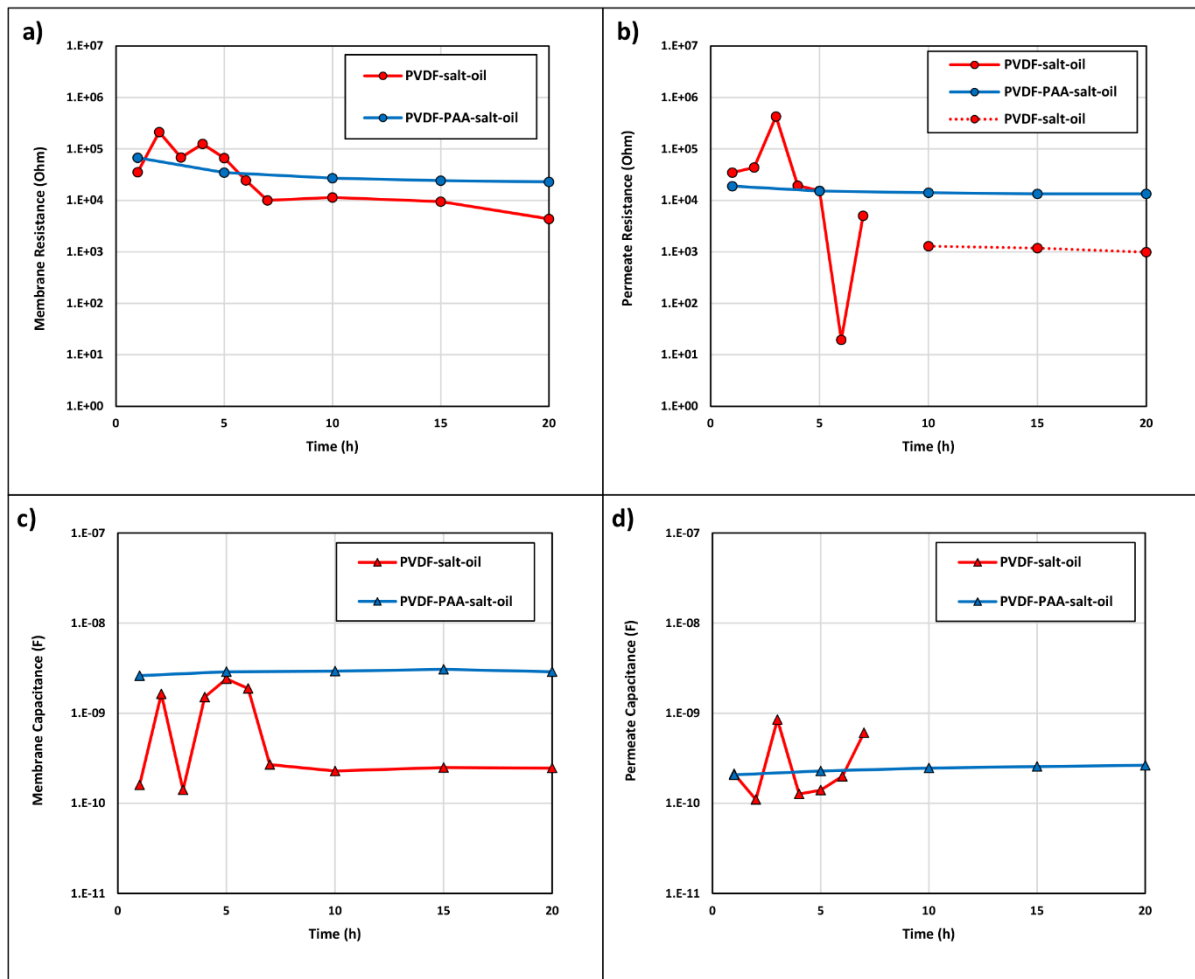


**Figure 7.7:** Membrane resistance (a, and capacitance b); and permeate resistance (c, and capacitance d), obtained from model fitting on PVDF-salt-oil and PVDF-PAA-salt-oil systems. The permeate resistance for the PVDF-salt-oil system is shown in dotted lines for  $t > 7$  h to highlight the fact that this value is obtained for the modified equivalent circuit and may include contributions from both permeate and feed solutions. The corresponding permeate capacitance was not present in the modified circuit model and the data are absent for this parameter after  $t=7$  h.

To further understand the changes in different parameters of the system, the resistance and the capacitance of the permeate obtained from the curve fitting are graphed in **Figures 7.7b** and **d**, respectively. The resistance of the permeate in the PVDF-PAA-salt-oil system only slightly decreases with time, which is in agreement with the fact that no change in the permeate EC in the permeate container was observed (**Figure 7.1c**). In addition, the capacitance of the permeate increases slightly with time for this system. The observed changes for this system could be the result of either a minor leakage through the membrane (i.e., transfer of oil), or numerical errors

in curve fitting. The changes are however very minor, and hence considered in alignment with the experimental EC results.

As shown in **Figure 7.7b**, the resistance of the permeate for the PVDF-salt-oil system exhibits fluctuations over time, going through a maximum at  $t=3$  h and a local minimum at  $t=6$  h. Otherwise, until  $t=9$  h for the PVDF-salt-oil system, the values of the permeate resistance are close to those obtained for the PVDF-PAA-salt-oil system. After  $t=9$  h, the system no longer follows the behaviour expected based on the equivalent circuit presented in **Table 7.1**, and as mentioned above, it was modelled using a modified equivalent circuit (**Figure 7.6**). Comparing the values obtained for the resistance of the combined solutions after  $t=9$  h and that of the permeate solution prior to  $t=9$  h, for the PVDF-salt-oil system, it can be observed that the resistance of the combined solution is lower than the permeate resistance suggesting the possibility of membrane wetting. In the opposite case where the liquids are not mixed, the total resistance of the permeate and feed solution in series would be equal to or higher than the permeate resistance, because the resistivity of two resistors in series are additive. The readings from EC meter are also in agreement with these observations, as a rise in permeate EC is observed after  $t=9$  h. Overall, a side-by-side comparison between the membrane- and permeate-resistance (**Figures 7.7a and b**), and between the membrane- and the permeate- capacitance (**Figures 7.7a and b**) shows that the changes in the properties of the membrane and the permeate solution happened almost at the same time for the PVDF-salt-oil system, while in the PVDF-PAA-salt-oil system, the mild changes in the membrane resistance has not led to any noticeable change in the permeate properties. Therefore, it is possible to correlate the results of the fitted parameters to the occurrence of wetting in the studied systems independent from the EC results, and by observing the permeate properties; while establishing this correlation was not possible based on solely analysing the impedance modulus values at high or low frequencies over time.

Overall, by comparing the fitting results for the PVDF-PAA-salt system, it can be observed that the membrane and permeate resistance and capacitance may not have a large contribution to the changes observed in the Nyquist and Bode plots. This is an interesting effect that might be related to the EDL properties reflected in the values of the CPE parameters, which could be worth further investigations in future research.

## 7.5 Conclusions

To understand the wetting behaviour of membrane distillation (MD) membranes during the treatment of oily water, this work entailed a dedicated study using time-resolved full-frequency sweep electrochemical impedance spectroscopy (EIS). The findings of this research were supported by comparing the observations of two MD membranes, one was a pristine hydrophobic

PVDF that wetted during MD operation; and its modified version with grafted PAA that did not show signs of wetting over 20 h of MD. The main conclusions are summarized as:

- MD was analysed using EIS to explore wetting behaviour in oily waters with hydrophobic, and PAA coated chemistry membranes;
- Visual analysis of the EIS data showed clear trends in behaviour associated with membrane wetting events for hydrophobic PVDF;
- Results were contrary to previous work where single frequency analysis could be correlated to specific MD behaviour, being wetting in this studied case. Effects occurred at low frequencies, but considering noise and complexity of the observed EIS patterns, equivalent circuit analysis was proposed as a more appropriate means to correlate to MD performance effects;
- Static testing allowed the development of equivalent circuits for key MD module components. However, for the membrane equivalent circuit, only a pre-wetted membrane was able to provide appropriate fitting to EIS results;
- The equivalent circuit was revised to consider major changes in model sensitivity pre- and post-wetting events;
- Both the PVDF and the PVDF-PAA membranes showed a reduction in the impedance modulus  $|Z|$  at high frequencies. However, only the PVDF samples showed changes in flux and an increase in the permeate EC. This implies that the occurrence of wetting cannot be unambiguously determined by simply monitoring the impedance modulus at high- $f$  range and the membrane properties should be extracted through equivalent circuit analysis using models developed for the very setup under study. Membrane resistance was found to follow MD wetting events only for when oily waters were included in solution. Membrane capacitance was unchanged over the test duration. The equivalent circuit could not be fit to the NaCl solution only (no oil) MD test; and
- Permeate resistance and capacitance followed MD behaviour in terms of expected performances and permeate EC measurements. The permeate resistance showed a drop and the capacitance showed an increase near the onset of wetting in the PVDF-salt-oil system, while it showed no noticeable changes in the PVDF-salt-oil system.
- While the equivalent circuit analysis of the EIS data employed in the current study is independent of the type of the feed solution, it is limited by the uncertainty in multi-parameter numerical model fitting.

Overall, this work has shown how EIS needs careful consideration in its data handling to interpret results that are appropriately assigned to MD performance events such as wetting. Future work can explore specific effects within a complex EIS system to further uncover the behaviour linked to MD performance and new membrane chemistries conveniently in real-time.

# Chapter 8 Conclusions and future directions

---

## 8.1 Summary of the current research

Through this PhD study, a salinity responsive MD membrane was successfully developed by grafting a negatively-charged polyelectrolyte (PAA) onto the surface of a commercial hydrophobic membrane (PVDF; mean pore size = 0.2  $\mu\text{m}$ ) via a novel oxygen tolerant UV-assisted atom transfer radical polymerization (ATRP) method. The aim was not only on the development of adequate membranes for overcoming oil-fouling and wetting issues that are detrimental in MD applications, but also on the in-depth understanding as to what membrane properties contributed to anti-oil-adhesion and anti-oil-wetting properties of the membrane. The specific conclusions of the current research can be summarized as below:

- 1) **Surface science describing fouling of MD membranes:** According to the analysis of the surface science literature performed in **Chapter 2** of the current thesis, surface interactions can play a major role in colloidal adhesion in MD membranes. It was highlighted in this analysis that the MD membranes have a composite interface consisting of topographical and chemical heterogeneities that need to be considered in the studies of colloidal adhesion that are practically realised as ‘fouling’. This composite interface is made up of a solid-liquid portion that forms between the membrane solid surface and the feed water, and an air liquid portion that forms between the feed water and the trapped air pockets in the roughness features of the membrane as well as in the pore entrances. For the region of the solid-liquid interfaces that are in a direct contact with water, an increase in the size of roughness features can contribute to an increase in particle attachment at high salinities. However, it also decreases the likelihood of irreversible particle attachment. In addition, local favourable attachment conditions can be created by the opposite charges on the membrane in form of patches that can attract colloidal particles. This means that the total charge of the membrane might not be a reliable factor in predicting tendency of the membrane in resisting the adhesion of a particular colloid. It was also highlighted that the membrane surface should be considered as a whole for a better understanding of colloidal adhesion in MD membranes. This is because the presence of air-water interfaces can act as attractive patches for hydrophobic compounds subsequently leading to the entrapment of colloidal particles in these interfaces and blockage of the pores.
- 2) **Demonstration of a new readily-scalable oxygen tolerant ATRP:** Oxygen tolerant UV-assisted ATRP was found to be viable method for grafting PAA onto a commercial PVDF under open atmosphere and for preparing a salinity responsive membrane (PVDF-PAA) for MD (**Chapters 4 and 5**). Successful grafting of PAA was verified by the ATR-FTIR

spectroscopy as evidenced by the peaks related to the asymmetric stretching of  $\text{-COO}^-$  (at  $1580\text{ cm}^{-1}$ ), COOH stretching (at  $1680\text{ cm}^{-1}$ ), and  $\text{-OH}$  stretching (at  $3000\text{-}3500\text{ cm}^{-1}$ ). In addition, SEM-EDX analyses showing a high atomic concentration of oxygen on the top of surface roughness features implying the higher concentration of PAA molecules in these regions. This further aligned with the employed surface treatment method that was performed without pre-wetting of the membrane in the first stage of creating the grafting sites on the membrane surface (the alkaline treatment). In addition, in-air water contact angle measurements showed a drop in the water contact angle from  $134 \pm 2^\circ$  to  $110 \pm 3^\circ$  due to the presence of the hydrophilic PAA brushes. The streaming potential analysis showed streaming potential analyses showed an increase in the negative surface zeta potential of the PVDF-PAA membrane (ca.  $-44\text{ mV}$ ) as compared to the PVDF membrane (ca.  $-22\text{ mV}$ ) due to the presence of the negatively charged PAA brushes.

- 3) **Salinity responsive PAA grafted MD membranes showed oil adhesion resistance:** The underwater oil adhesion tests performed on the prepared PVDF-PAA membranes showed evidence of the response of the PAA brushes to salinity (**Chapters 5 and 7**). It was found that in the absence of NaCl, oil was able to adhere to the PVDF-PAA membrane and penetrate the membrane over time. However, with the addition of NaCl to the test solution with a concentration of as low as  $0.01\text{ M}$ , the PVDF-PAA membrane became underwater-superoleophobic. This change could be attributed to the expansion of the PAA chains in response to increase in salinity. However, the underwater superoleophobic behaviour of the PVDF-PAA membrane persisted under high NaCl concentrations ( $3\text{ M NaCl}$ ), which implied that the decrease in brush thickness in salted brush regime did not significantly decrease the underwater oleophobicity of this surface. Conversely, the PVDF membrane was wetted by oil regardless of the salinity of the test medium.
  
- 4) **A model to describe underwater oleophobicity of PVDF-PAA membranes in the context Janus membranes:** According to the proposed model in **Chapter 6**, the PAA molecules are assumed to be located on the top region of the roughness features of the membrane that are in direct contact with water during MD. This membrane exhibits underwater oleophobicity under various scenarios, especially in the case where there is minimal trapped water within the roughness features and the pore entrances after the oil droplet is placed in contact with the membrane. Therefore, it was found that the underwater oleophobicity of this type of surface originates from the combined effect of the hydrophilic patches (PAA brushes) and the air pockets trapped within the surface roughness features and inside the pores. In addition to this case, other scenarios were investigated within the framework of this model, and it was found that underwater oleophobicity depends on the surface fraction of the hydrophilic

patches (the PAA brushes) on the top surface of the membrane as well as the total surface fraction of the top surface of the membrane.

- 5) **Effective MD operation with PVDF-PAA membrane in oily solutions:** The PVDF-PAA membrane showed superior performance in MD of a model dispersed oily saline solution ((0.1% (v/v) dodecane+0.1 M NaCl) for 20 h with a stable flux (16-17 kg/(m<sup>2</sup>.h)) and no significant permeate EC rise (**Chapters 5 and 7**). However, the PVDF membrane was wetted and fouled by oil with its flux dropping from ca. 12.5 kg/(m<sup>2</sup>.h) to 2.6 kg/(m<sup>2</sup>.h) during the first 5 h of the MD experiment. The permeate EC for this membrane significantly increased throughout the experiment (by almost 40 folds). The resistance of the PVDF-PAA membranes can be attributed to the hydration and negative surface of the PAA chains as well as the location of the PAA-grafted patches on the membrane surfaces.
  
- 6) **Extension of EIS knowledge for explaining MD membrane behaviour and anti-wetting mechanisms:** Oil wetting was also analysed in **Chapter 7** of the current study by real-time in-situ electrochemical impedance spectroscopy (EIS) employing a wide frequency sweep (1 Hz to 500 kHz). Holistic analysis of the EIS results showed significant differences between the behaviour of PVDF and PVDF-PAA membranes against dispersed oily solutions. In the Bode graphs, a large drop in impedance (by 1-2 orders of magnitude) was observed at the low- and mid-frequency (<10 kHz) end of the graphs with time for the PVDF membrane, while the drop in impedance was not significant for the PVDF-PAA membrane under similar conditions. The equivalent circuit analysis of the EIS results showed that the membrane resistance and capacitance might not have a significant contribution to the total impedance. Instead, the impedance was influenced more by the electrical double-layer (EDL) properties of both the feed and the permeate solutions, as well as the resistance and the capacitance of the permeate solution.

## 8.2 Future directions:

Further research areas can be explored based on the results of this study. A few examples of these works are proposed below:

1. **Modelling of the surface interactions in MD employing (X)DLVO theory:** Understanding the effects of surface interactions in colloidal adhesion to the MD membranes can lead to the design of better adhesion-resistant membranes. However, in the analyses performed in the current thesis, it was identified that the effect of surface interaction in MD has not been well understood. Therefore, future studies on this topic could include modelling of the surface interactions in MD membranes using (X)DLVO theory by considering the complex interfaces of the MD membranes and accounting for

the effects of surface topography and chemistry. These studies can shed light on the underlying mechanisms of surface interactions as well as the contribution of each portion of the interfaces in determining the adhesion of the colloidal particles onto the membranes. In addition, these studies may require an accurate measurement of the surface properties of the rough membranes which is a serious challenge due to the complex effects the roughness on the measured values. Therefore, further research is needed to develop and optimize facile methods that can accurately measure the surface properties of such surfaces.

2. **Harnessing the full potential of oxygen-tolerant UV-ATRP:** Current thesis showcased a specific combination of a polyelectrolyte grafted onto a membrane. However, considering the versatility of the ATRP reaction systems in working with a wide variety of monomers [34, 159, 161], further research can explore the grafting of many other types of polymers such as zwitterionic and positively charged polyelectrolytes on various different membranes (RO, NF, UF, etc.) in developing membranes with advanced functionalities.

Another unique advantage of ATRP as a living radical polymerization is its high level of control over the molecular structure of the grafted polymers by exploiting the ‘living’ aspect of this polymerization reaction [34, 159, 161]. This feature allows for the consecutive polymerization of multiple monomers forming block copolymers with controlled structures. Block copolymer brushes can provide opportunities for more complex functionalities for membranes due to their controllable phase transitions [161]. Therefore, future studies can explore the grafting of block copolymer brushes on membrane surfaces in creating membranes with special functionalities.

A major challenge in the application of the oxygen tolerant UV-ATRP in industrial scale is the difficulties related to the initiator grafting [34]. This step is usually performed in laboratory settings using tedious reaction steps that take several hours. However, more straightforward methods need to be adopted and/or developed for initiator grafting steps to enable a successful scale-up of UV-ATRP.

In the current study, only UV light was employed for performing the ATRP reactions. However, in there are several studies that showed the successful application of visible light instead of UV [68, 233-235]. Therefore, further research can investigate the application of visible light in the ATRP of different monomers onto membrane surfaces. This can further improve the feasibility of the ATRP reactions for industrial applications by decreasing the associated production costs.

The stability and robustness of the grafted chains is another topic of concern in surface grafting reactions using UV-ATRP. Due to the low amount of grafted PAA, as well as the



specific grafting of PAA on the top of the roughness features, an accurate measurement of the grafting density was not possible in the current study. Therefore, further research is needed to develop methods that can accurately measure the grafting density of the polymer brushes on rough (and porous) membrane surfaces. This will provide an opportunity to measure the robustness of the grafted brushes.

Finally, the environmental impact and sustainability of the surface modification step can influence the applicability of the proposed method in industry. Further research is needed to investigate alternative environmentally friendly methods for surface modification of MD membranes.

- 3. Behaviour of the PVDF-PAA membranes against other colloids:** As discussed above, the PVDF-PAA membranes developed in the current study exhibited superior behaviour in the MD of a model dispersed oily water. However, the application of these membranes can further be explored in the treatment of other colloids such as proteins, emulsified oils, and milk to explore the effect of the changes in colloid surface properties on the performance of these membranes. In addition, the salt responsive behaviour of the PVDF-PAA membranes can further be explored against real oily wastewaters which often contain multiple compounds as well as mixtures of various monovalent and multivalent salts. Multivalent ions can lead to the collapse of the PAA brushes due to their bridging effect. It can be hypothesized that these ions may lead to reduced oleophobicity in the developed PVDF-PAA membranes. Finally, real wastewaters containing a broader range of contaminants such as humic acids and microorganisms can be explored to evaluate the response of the PAA brushes in complex environments.
- 4. A deeper analysis of the proposed model for the surface-grafted membranes:** Modelling of the underwater oil contact angle of the Janus membranes developed in the current study showed a general agreement between the modelling predictions and obtained results. However, the proposed modelling approach did not take into account effects such as the dynamic response of the PAA brushes to salinity and changes in the interfacial energies of the involved compounds. Further studies can include these effects in the analysis of underwater oil contact angle of similar Janus membrane surfaces to better understand the behaviour of this type of membranes against oil adhesion and intrusion. In addition, future studies can include a more rigorous validation of the proposed models and their transitions by employing specialized experimental design and appropriate numerical modelling methods.

The commercial PVDF membrane selected for the surface grafting in the current thesis was a model to showcase the wide possibilities that can be adopted for this purpose. Especially, the grafting method employed in this study can be extended to membranes with different topographies to understand the effect of topography on the oil adhesion resistance of these membranes. Further research can take advantage of the re-entrant roughness geometries of omniphobic membranes to create Janus membranes that are simultaneously resistant to dispersed oils and low-surface-tension feed liquids.

5. **Design of special electrodes for *in-situ* EIS studies of oil wetting in MD:** The *in-situ*-EIS studies performed in the current thesis suggested the possible interferences in the obtained data from the feed and permeate properties as well as noise related to the high impedance of the system. Therefore, further research can focus on the design of new electrodes and membrane cells that allow for capturing the behaviour of the system over a wide range of frequencies by minimizing the mentioned interferences. In addition, the application of complementary methods such as optical coherence tomography (OCT), and fluorescence microscopy alongside EIS can provide deeper insight on the occurrence of colloidal adhesion and wetting in MD.

# Appendices

## Appendix A: Sample derivation of underwater oleophobicity of the models proposed in Chapter 6

Here, the underwater oil contact angle derivations for “**Model 1-Scenario 1**” and **Model 2** will be discussed as examples.

Similar to the in-air contact angle of the model membranes, Cassie’s equation can be written for the underwater oil contact angle ( $\theta_{o,total}$ ) of Model 1-Scenario 1:

$$\cos \theta_{o,total} = f_{top} \cos \theta_{o,top} + f_{pore} \cos \theta_{o,air} \quad \text{Equation A.1}$$

Where  $\theta_{o,top}$  and  $\theta_{o,air}$  are the underwater oil contact angles of the top surface and the air ( $\sim 180^\circ$ , because oil does not spread in air), respectively. Further, according to Cassie’s equation for the top surface:

$$\cos \theta_{o,top} = f_{PAA} \cos \theta_{o,PAA} + f_{PVDF} \cos \theta_{o,air} \quad \text{Equation A.2}$$

In which  $\theta_{o,PAA}$ ,  $\theta_{o,air}$  are the underwater oil contact angles of a “flat and smooth PAA-grafted surface” and the oil-air interfaces. It is important to note that the oil droplet is assumed not to penetrate past the PAA-grafted region and not to contact the region with exposed PVDF (thus forming a metastable Cassie-Baxter state).

Similar to the in-air water contact angle calculations, considering  $f_{top} + f_{pore} = 1$  and  $f_{PAA} + f_{PVDF} = 1$ ,  $\cos \theta_{air} = -1$ , and by substituting **Equation A.2** into **Equation A.1**, the following can be obtained:

$$\cos \theta_{o,total} = f_{top} f_{PAA} (\cos \theta_{o,PAA} + 1) - 1 \quad \text{Equation A.3}$$

Here,  $\cos \theta_{o,PAA} \leq 0$ , therefore  $\cos \theta_{o,total} \leq 0$ .

For the underwater oil contact angle of **Model 2**:

$$\cos \theta_{o,total} = f_{top} \cos \theta_{o,top} + f_{pore} \cos \theta_{o,water} \quad \text{Equation A.4}$$

And

$$\cos \theta_{o,top} = R_f \cos \theta_{o,PAA} \quad \text{Equation A.5}$$

In addition,  $f_{top} + f_{pore} = 1$  and  $\cos \theta_{water} = 1$ , therefore:

$$\cos \theta_{o,total} = f_{top} (R_f \cos \theta_{o,PAA} - 1) + 1 \quad \text{Equation A.6}$$

## Appendix B: Supplementary information on real-time in-situ EIS studies of oil wetting in MD (Chapter 7)

B1: Dynamic EIS results on the three studied systems (PVDF-salt, PVDF-salt-oil, and PVDF-PAA-salt-oil)

Full view of the normalized  $|Z|$  plots and Nyquist plots are shown in Figure S1 and S2, respectively.

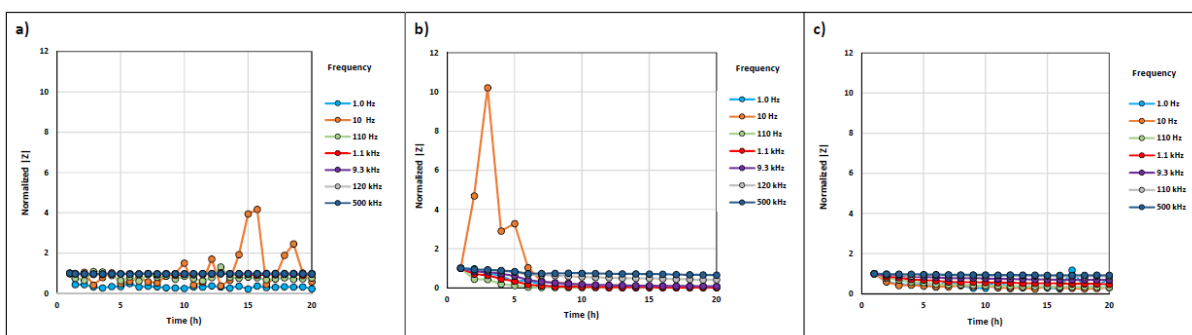


**Figure B 1.** Full view of the normalized impedance modulus ( $|Z|/|Z_1|$ ) (where  $|Z_1|$  is the value of impedance at  $t=0$  h (bottom row)) at different frequencies vs. time for PVDF-salt: a) and d); PVDF-salt-oil: b) and e); PVDF-PAA-salt-oil: c) and f). Feed and permeate inlet temperatures were constant at  $60^\circ\text{C}$  and  $20^\circ\text{C}$ , and the crossflow velocity of both feed and permeate was  $3.13$  m/min. The oily dispersion contained  $0.1\%$  (v/v) dodecane and  $0.1$  M NaCl in water. The saline solution contained  $0.1$  M NaCl in water.

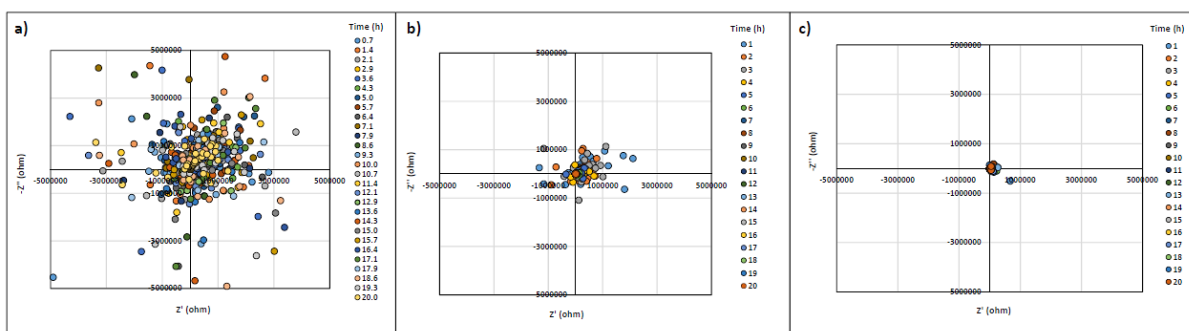


**Figure B 2:** Full view of the Nyquist plots at different times for PVDF-salt: a) and d); PVDF-salt-oil: b) and e); PVDF-PAA-salt-oil: c) and e). Feed and permeate inlet temperatures were constant at  $60^\circ\text{C}$  and  $20^\circ\text{C}$ , and the crossflow velocity of both feed and permeate was  $3.13$  m/min. The oily dispersion contained  $0.1\%$  (v/v) dodecane and  $0.1$  M NaCl in water. The saline solution contained  $0.1$  M NaCl in water.

**B2: Details on the fitting procedures for the development of the equivalent circuits employed in the in-situ EIS analyses**

The detailed analysis and fitting of the EIS data for each element in the equivalent circuit is described below.

**a. The cell:**

Dry cell tests were performed on the cell with and without the membrane without addition of any liquid to the feed and permeate compartments. The cell is simulated using a single capacitor. The equivalent circuit and the curve fitting results for the cell properties are shown in Figure S1. For the curve fitting, the  $Z''$  data from the dry cell system without the membrane was fitted using OriginPro 9.1 by a custom equation for a single capacitor ( $Z'' = -j/(wC)$ ). The curve fitting was performed on the data in the frequency range of 110 Hz to 500 kHz using Lavenberg-Marquardt nonlinear curve fitting algorithm. The capacitance value obtained for the membrane cell (64 pF) was held constant in the subsequent curve fittings performed on the system. The highest impedance that the system can register with the current setup apart from the instrument internal impedance, is the impedance of the cell which manifests itself as a capacitor in parallel with the system. The fitting results and the equivalent circuit for the cell impedance is shown in **Figure B3**.

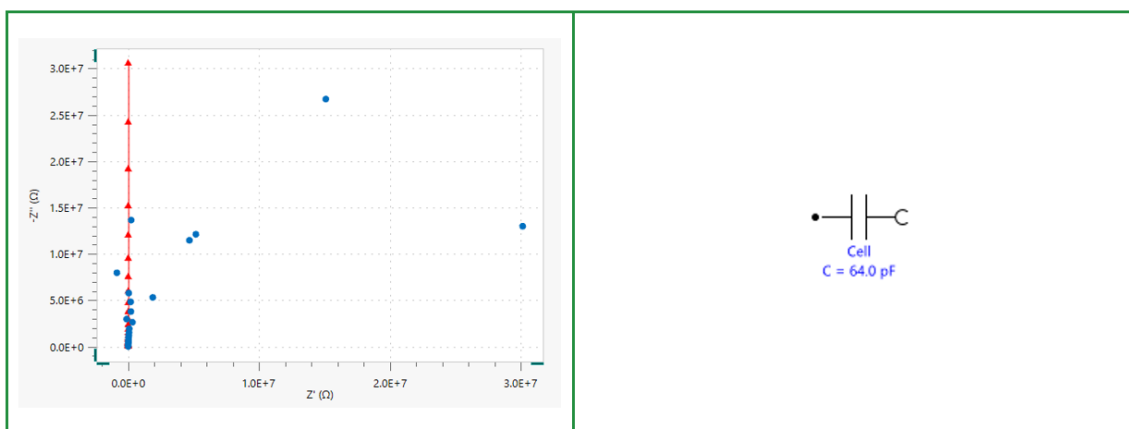


**Figure B 3:** The equivalent circuit and curve fitting results on the cell properties. In the Nyquist plots, the blue circles represent the raw data and the red triangles represent the fitted curve.

**b. The feed compartment:**

The feed liquid modelled was 0.1M NaCl solution in water, and the effect of oil droplets on electrical properties of the system are ignored for simplicity. The EIS test was performed on the module with the membrane and with the saline solution (0.1M NaCl) only. A proposed equivalent circuit for this compartment as well as the model fitting results are presented in **Figure B4**. The equivalent circuit model for the saline solution includes a resistor in series

with a constant phase element representing the solvent impedance and the impedance of the EDL of the surfaces of the electrode and the membrane in parallel with the cell capacitance. In the proposed equivalent circuit, the contribution from the EDLs of the electrode-feed and membrane feed interfaces are combined in one CPE, because the two CPE components in series are mathematically equivalent and create redundancy for the fitting algorithm. In other words, the algorithm has no way of differentiating between the two components. Therefore, when possible, it is recommended to combine mathematically equivalent circuit elements into a single circuit element that can represent the properties of its constituent elements. It is important to note that after obtaining the value for the new surrogate element, it might be possible to find the value of the constituent elements if they are measured separately or if they are assumed to have similar EDL properties.

It should be noted that in the analyses related to the EDL properties, it is assumed that the electrodes and the membrane are ideally polarizable for the purposes of our study, meaning that no electrochemical reactions take place on the solid liquid interfaces. This assumption is based on the fact that the maximum root-mean-square (RMS) amplitude of the voltage difference between the electrodes are set to 0.01 V which is lower than the oxidation/reduction potential of almost all known species present in the system. However, this does not necessarily preclude the occurrence of any electrochemical reactions in the EDLs since the gradient of the electric potential is very high with EDLs regardless of the maximum voltage difference between the electrodes. Nevertheless, to avoid the complexities related to the Faradaic reactions in the analysis of our system, the occurrence of such reactions is assumed to have negligible effects on the EIS results.

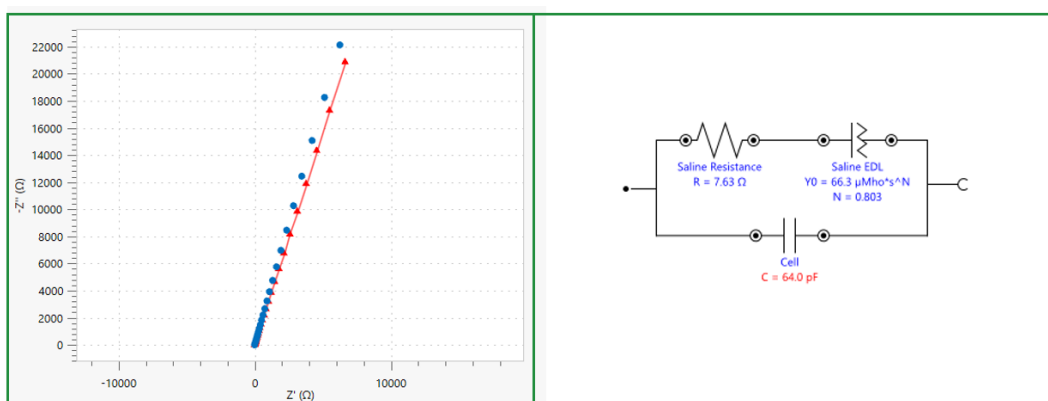


**Figure B 4:** The equivalent circuit and curve fitting results on the feed compartment properties. In the Nyquist plots, the blue circles represent the raw data and the red triangles represent the fitted curve.

**c. The permeate compartment:**

The permeate liquid is assumed to be consisted of MilliQ water only. To analyse the electrical properties of the permeate compartment the static EIS test was performed on the module filled

with MilliQ water without the membrane. The proposed equivalent circuit along with the fitting result is shown in **Figure B5**. As can be observed from this figure, a new capacitor is introduced into the equivalent circuit model of the electrodes in contact with the MilliQ water. This new capacitor accounts for the capacitance behaviour of the space between the electrodes filled with MilliQ water. This capacitor was absent in the model for the feed compartment because of the low resistance of the solution and the negligible effect of the capacitive properties of the saline solution against its resistive properties.

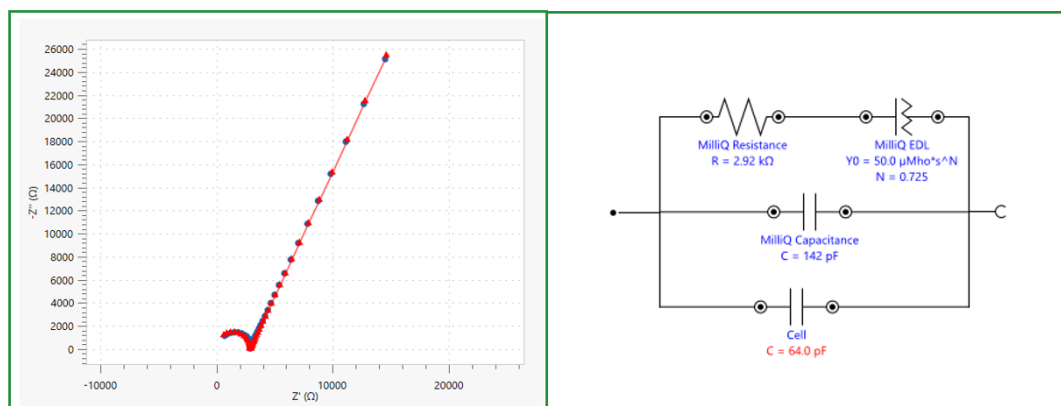


**Figure B 5:** The equivalent circuit and curve fitting results on the permeate compartment properties. In the Nyquist plots, the blue circles represent the raw data and the red triangles represent the fitted curve.

#### d. The membrane and the combined equivalent circuit model:

In this study, similar to other EIS studies in MD, the membrane is modelled using a Maxwell element (a resistor in parallel with a capacitor). To obtain an initial guess value for the membrane properties, the entire cell needs to be considered with all compartments developed in the previous subsections. For this purpose, static tests were performed to simulate the conditions of MD under two scenarios, namely, the nonwetted and wetted scenarios. In the nonwetted scenario, in presence of the intact (nonwetted) PVDF membrane, the feed compartment was filled with the 0.1M NaCl solution and the permeate compartment was filled with MilliQ water. In the wetted scenario, the membrane was wetted by dispensing 2-3 droplets of oil directly onto the membrane before the module was assembled and the feed and permeate compartments were filled with the 0.1M NaCl and MilliQ water, respectively. The EIS data fitting was performed using the initial guesses obtained from the individual compartments calculated before. However, the model fitting was only successful for the wetted system. The EIS data, and the fitting results of the final equivalent circuit for the wetted scenario are shown in **Figure B6**. For the purposes of this study, the values of the parameters obtained for the wetted case were chosen as the initial guesses for curve fittings on the real-time data for both the PVDF-salt-oil and PVDF-PAA-salt-oil systems.

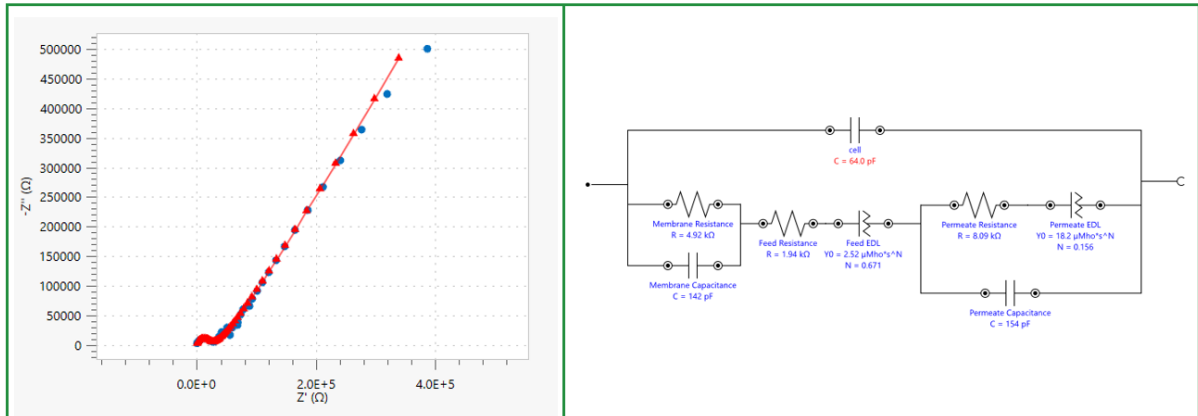


**Figure B 6:** The equivalent circuit and curve fitting results on the entire system including the membrane for the wetted scenario. In the Nyquist plots, the blue circles represent the raw data and the red triangles represent the fitted curve.



## References

---

1. Deshmukh, A., et al., *Membrane distillation at the water-energy nexus: limits, opportunities, and challenges*. Energy & Environmental Science, 2018. **11**(5): p. 1177-1196.
2. Alkhudhiri, A., N. Darwish, and N. Hilal, *Membrane distillation: a comprehensive review*. Desalination, 2012. **287**: p. 2-18.
3. Cheryan, M. and N. Rajagopalan, *Membrane processing of oily streams. Wastewater treatment and waste reduction*. Journal of membrane science, 1998. **151**(1): p. 13-28.
4. Jamaly, S., A. Giwa, and S.W. Hasan, *Recent improvements in oily wastewater treatment: Progress, challenges, and future opportunities*. Journal of Environmental Sciences, 2015. **37**: p. 15-30.
5. Boo, C., J. Lee, and M. Elimelech, *Omniphobic polyvinylidene fluoride (PVDF) membrane for desalination of shale gas produced water by membrane distillation*. Environmental science & technology, 2016. **50**(22): p. 12275-12282.
6. Wang, K., et al., *Development of a composite membrane with underwater-oleophobic fibrous surface for robust anti-oil-fouling membrane distillation*. Journal of colloid and interface science, 2019. **537**: p. 375-383.
7. Wang, Z. and S. Lin, *Membrane fouling and wetting in membrane distillation and their mitigation by novel membranes with special wettability*. Water research, 2017. **112**: p. 38-47.
8. Chew, N.G.P., S. Zhao, and R. Wang, *Recent advances in membrane development for treating surfactant-and oil-containing feed streams via membrane distillation*. Advances in colloid and interface science, 2019. **273**: p. 102022.
9. Ardeshiri, F., et al., *PDADMAC/PAA semi-IPN hydrogel-coated PVDF membrane for robust anti-wetting in membrane distillation*. Journal of Industrial and Engineering Chemistry, 2019. **74**: p. 14-25.
10. Ardeshiri, F., et al., *A hydrophilic-oleophobic chitosan/SiO<sub>2</sub> composite membrane to enhance oil fouling resistance in membrane distillation*. Korean Journal of Chemical Engineering, 2019. **36**: p. 255-264.
11. Han, L., et al., *Understanding oily wastewater treatment via membrane distillation*. Journal of Membrane Science, 2017. **539**: p. 284-294.
12. Han, L., et al., *Zwitterionic grafting of sulfobetaine methacrylate (SBMA) on hydrophobic PVDF membranes for enhanced anti-fouling and anti-wetting in the membrane distillation of oil emulsions*. Journal of Membrane Science, 2019. **588**: p. 117196.
13. Hou, D., et al., *Composite membrane with electrospun multiscale-textured surface for robust oil-fouling resistance in membrane distillation*. Journal of Membrane Science, 2018. **546**: p. 179-187.
14. Huang, Y.-X., et al., *Novel Janus membrane for membrane distillation with simultaneous fouling and wetting resistance*. Environmental science & technology, 2017. **51**(22): p. 13304-13310.
15. Sun, W., et al., *An ultrathin, porous and in-air hydrophilic/underwater oleophobic coating simultaneously increasing the flux and antifouling property of membrane for membrane distillation*. Desalination, 2018. **445**: p. 40-50.

16. Wang, K., et al., *Hydrophilic surface coating on hydrophobic PTFE membrane for robust anti-oil-fouling membrane distillation*. Applied Surface Science, 2018. **450**: p. 57-65.
17. Wang, Z., D. Hou, and S. Lin, *Composite membrane with underwater-oleophobic surface for anti-oil-fouling membrane distillation*. Environmental science & technology, 2016. **50**(7): p. 3866-3874.
18. Wang, Z., et al., *Tailoring surface charge and wetting property for robust oil-fouling mitigation in membrane distillation*. Journal of Membrane Science, 2016. **516**: p. 113-122.
19. Chen, Y., et al., *Probing pore wetting in membrane distillation using impedance: early detection and mechanism of surfactant-induced wetting*. Environmental Science & Technology Letters, 2017. **4**(11): p. 505-510.
20. Wang, Z. and S. Lin, *The impact of low-surface-energy functional groups on oil fouling resistance in membrane distillation*. Journal of Membrane Science, 2017. **527**: p. 68-77.
21. Zhu, Z., et al., *Breathable and asymmetrically superwetable Janus membrane with robust oil-fouling resistance for durable membrane distillation*. Journal of Membrane Science, 2018. **563**: p. 602-609.
22. Zuo, G. and R. Wang, *Novel membrane surface modification to enhance anti-oil fouling property for membrane distillation application*. Journal of membrane science, 2013. **447**: p. 26-35.
23. Du, X., et al., *Membrane fouling and reusability in membrane distillation of shale oil and gas produced water: Effects of membrane surface wettability*. Journal of Membrane Science, 2018. **567**: p. 199-208.
24. Lu, K.J., Y. Chen, and T.-S. Chung, *Design of omniphobic interfaces for membrane distillation—a review*. Water research, 2019. **162**: p. 64-77.
25. Afsari, M., H.K. Shon, and L.D. Tijing, *Janus membranes for membrane distillation: Recent advances and challenges*. Advances in Colloid and Interface Science, 2021. **289**: p. 102362.
26. Meng, L., et al., *Janus membranes at the water-energy nexus: A critical review*. Advances in Colloid and Interface Science, 2023: p. 102937.
27. Lu, K.J., Y. Chen, and T.-S. Chung, *Design of omniphobic interfaces for membrane distillation—A review*. Water research, 2019.
28. Chen, Y., et al., *Anti-wetting behavior of negatively charged superhydrophobic PVDF membranes in direct contact membrane distillation of emulsified wastewaters*. Journal of Membrane Science, 2017. **535**: p. 230-238.
29. Hou, D., et al., *Effect and mechanism of an anionic surfactant on membrane performance during direct contact membrane distillation*. Journal of Membrane Science, 2020. **595**.
30. Liu, C., L. Chen, and L. Zhu, *Fouling behavior of lysozyme on different membrane surfaces during the MD operation: An especial interest in the interaction energy evaluation*. Water Research, 2017. **119**: p. 33-46.
31. Wang, X., et al., *Modification of the distribution of humic acid complexations by introducing microbubbles to membrane distillation process for effective membrane fouling alleviation*. Journal of Environmental Management, 2023. **348**: p. 119171.
32. Li, C., et al., *Antiwetting and antifouling Janus membrane for desalination of saline oily wastewater by membrane distillation*. ACS applied materials & interfaces, 2019. **11**(20): p. 18456-18465.

33. Pyun, J., T. Kowalewski, and K. Matyjaszewski, *Synthesis of polymer brushes using atom transfer radical polymerization*. *Macromolecular Rapid Communications*, 2003. **24**(18): p. 1043-1059.
34. Zoppe, J.O., et al., *Surface-initiated controlled radical polymerization: state-of-the-art, opportunities, and challenges in surface and interface engineering with polymer brushes*. *Chemical reviews*, 2017. **117**(3): p. 1105-1318.
35. Bera, A., et al., *Stimuli responsive and low fouling ultrafiltration membranes from blends of polyvinylidene fluoride and designed library of amphiphilic poly (methyl methacrylate) containing copolymers*. *Journal of Membrane Science*, 2015. **481**: p. 137-147.
36. Fu, Y., et al., *pH-induced switchable superwettability of efficient antibacterial fabrics for durable selective oil/water separation*. *ACS applied materials & interfaces*, 2017. **9**(35): p. 30161-30170.
37. Han, Z., et al., *Toward robust pH-responsive and anti-fouling composite membranes via one-pot in-situ cross-linked copolymerization*. *Desalination*, 2014. **349**: p. 80-93.
38. Xu, R., et al., *Preparation of pH-responsive asymmetric polysulfone ultrafiltration membranes with enhanced anti-fouling properties and performance by incorporating poly (2-ethyl-2-oxazoline) additive*. *RSC advances*, 2018. **8**(72): p. 41270-41279.
39. Zhao, X., et al., *pH-responsive and fouling-release properties of PES ultrafiltration membranes modified by multi-functional block-like copolymers*. *Journal of membrane science*, 2011. **382**(1-2): p. 222-230.
40. Meng, J., et al., *A novel salt-responsive TFC RO membrane having superior antifouling and easy-cleaning properties*. *Journal of Membrane Science*, 2014. **461**: p. 123-129.
41. You, M., et al., *Fouling resistance and cleaning efficiency of stimuli-responsive reverse osmosis (RO) membranes*. *Polymer*, 2016. **103**: p. 457-467.
42. Vanangamudi, A., et al., *Thermo-responsive nanofibrous composite membranes for efficient self-cleaning of protein foulants*. *Journal of membrane science*, 2019. **574**: p. 309-317.
43. Xiang, Y., et al., *Efficient separation of O/W and W/O micro-emulsion by thermally responsive superantwetting PVDF membrane*. *Reactive and Functional Polymers*, 2015. **97**: p. 86-95.
44. Yu, S., et al., *Surface modification of thin-film composite polyamide reverse osmosis membranes with thermo-responsive polymer (TRP) for improved fouling resistance and cleaning efficiency*. *Separation and purification technology*, 2011. **76**(3): p. 283-291.
45. Yuan, X., et al., *Thermo-responsive PVDF/PSMA composite membranes with micro/nanoscale hierarchical structures for oil/water emulsion separation*. *Colloids and Surfaces A: Physicochemical and Engineering Aspects*, 2017. **516**: p. 305-316.
46. Li, J.-J., Y.-N. Zhou, and Z.-H. Luo, *Polymeric materials with switchable superwettability for controllable oil/water separation: A comprehensive review*. *Progress in Polymer Science*, 2018. **87**: p. 1-33.
47. Liu, F. and M.W. Urban, *Recent advances and challenges in designing stimuli-responsive polymers*. *Progress in polymer science*, 2010. **35**(1-2): p. 3-23.
48. Stuart, M.A.C., et al., *Emerging applications of stimuli-responsive polymer materials*. *Nature materials*, 2010. **9**(2): p. 101-113.

49. Ramanan, S.N., et al., *Self-cleaning membranes for water purification by co-deposition of photo-mobile 4, 4'-azodianiline and bio-adhesive polydopamine*. Journal of Membrane Science, 2018. **554**: p. 164-174.
50. Ju, J., et al., *Preparation and characterization of pH-sensitive and antifouling poly (vinylidene fluoride) microfiltration membranes blended with poly (methyl methacrylate-2-hydroxyethyl methacrylate-acrylic acid)*. Journal of colloid and interface science, 2014. **434**: p. 175-180.
51. Zou, W., et al., *Poly (methyl methacrylate–acrylic acid–vinyl pyrrolidone) terpolymer modified polyethersulfone hollow fiber membrane with pH sensitivity and protein antifouling property*. Journal of Membrane Science, 2010. **358**(1-2): p. 76-84.
52. de Leon, A. and R.C. Advincula, *Reversible superhydrophilicity and superhydrophobicity on a lotus-leaf pattern*. ACS applied materials & interfaces, 2014. **6**(24): p. 22666-22672.
53. Cheng, B., et al., *Development of smart poly (vinylidene fluoride)-graft-poly (acrylic acid) tree-like nanofiber membrane for pH-responsive oil/water separation*. Journal of membrane science, 2017. **534**: p. 1-8.
54. Yong, J., et al., *Photoinduced switchable underwater superoleophobicity–superoleophilicity on laser modified titanium surfaces*. Journal of Materials Chemistry A, 2015. **3**(20): p. 10703-10709.
55. Liu, J., et al., *Bioinspired graphene membrane with temperature tunable channels for water gating and molecular separation*. Nature communications, 2017. **8**(1): p. 1-9.
56. Di Luca, G., et al., *Aliquots of MIL-140 and Graphene in Smart PNIPAM Mixed Hydrogels: A Nanoenvironment for a More Eco-Friendly Treatment of NaCl and Humic Acid Mixtures by Membrane Distillation*. Membranes, 2023. **13**(4): p. 437.
57. Li, J., et al., *High performance membrane distillation membranes with thermo-responsive self-cleaning capacities*. Desalination, 2023. **555**: p. 116544.
58. Lim, W., et al., *Responsive switchable wettability membrane prepared via hydrogel coating and its performance recovery evaluation via membrane distillation*. Journal of Environmental Chemical Engineering, 2023. **11**(2): p. 109505.
59. Lyly, L., et al., *Development of membrane distillation by dosing SiO<sub>2</sub>-PNIPAM with thermal cleaning properties via surface energy actuation*. Journal of Membrane Science, 2021. **636**: p. 119193.
60. Lyly, L., et al., *Desalinating microalgal-rich water via thermoresponsive membrane distillation*. Journal of Environmental Chemical Engineering, 2021. **9**(5): p. 105897.
61. Salehi, S.M., et al., *Membrane distillation by novel hydrogel composite membranes*. Journal of membrane science, 2016. **504**: p. 220-229.
62. Zheng, L., et al., *Making waves: Magneto-responsive membranes with special and switchable wettability: new opportunities for membrane distillation*. Water Research, 2024. **249**: p. 120939.
63. Zhao, C., et al., *Polymeric pH-sensitive membranes—A review*. Progress in Polymer Science, 2011. **36**(11): p. 1499-1520.
64. Willott, J.D., et al., *Physicochemical behaviour of cationic polyelectrolyte brushes*. Progress in polymer science, 2017. **64**: p. 52-75.

65. Zhang, J., R. Kou, and G. Liu, *Effect of salt concentration on the pH responses of strong and weak polyelectrolyte brushes*. *Langmuir*, 2017. **33**(27): p. 6838-6845.
66. Yan, W., et al., *Surface-initiated photoinduced ATRP: Mechanism, oxygen tolerance, and temporal control during the synthesis of polymer brushes*. *Macromolecules*, 2020. **53**(8): p. 2801-2810.
67. Andersen, C., et al., *Antimicrobial PDMS Surfaces Prepared through Fast and Oxygen-Tolerant SI-SARA-ATRP, Using Na<sub>2</sub>SO<sub>3</sub> as a Reducing Agent*. *ACS omega*, 2021. **6**(22): p. 14551-14558.
68. Szczepaniak, G., et al., *Making ATRP more practical: oxygen tolerance*. *Accounts of Chemical Research*, 2021. **54**(7): p. 1779-1790.
69. Ahmed, F.E., N. Hilal, and R. Hashaikeh, *Electrically conductive membranes for in situ fouling detection in membrane distillation using impedance spectroscopy*. *Journal of Membrane Science*, 2018. **556**: p. 66-72.
70. Deka, B.J., et al., *A conductive hydrophobic polyaniline sandwiched polyvinylidene fluoride membrane for early detection of surfactant-induced wetting in membrane distillation using impedance*. *ACS Applied Polymer Materials*, 2021. **3**(2): p. 679-690.
71. Deka, B.J., et al., *Electrical impedance spectroscopy for non-destructive detection of wetting, fouling and scaling in membrane distillation*. *Journal of Water Process Engineering*, 2023. **53**: p. 103608.
72. Han, M., et al., *Membrane Distillation Hybrid Peroxydisulfate Activation toward Mitigating the Membrane Wetting by Sodium Dodecyl Sulfate*. *Membranes*, 2022. **12**(2): p. 164.
73. Li, C., et al., *Elucidating the trade-off between membrane wetting resistance and water vapor flux in membrane distillation*. *Environmental Science & Technology*, 2020. **54**(16): p. 10333-10341.
74. Wang, Z., et al., *Mechanism of pore wetting in membrane distillation with alcohol vs. surfactant*. *Journal of Membrane Science*, 2018. **559**: p. 183-195.
75. Wong, P.W., et al., *Noninvasive real-time monitoring of wetting progression in membrane distillation using impedance spectroscopy*. *Environmental Science & Technology*, 2021. **56**(1): p. 535-545.
76. Kralchevsky, P., et al., *Handbook of surface and colloid chemistry*. Birdi, KS, Ed, 1997.
77. Bormashenko, E., *Progress in understanding wetting transitions on rough surfaces*. *Advances in colloid and interface science*, 2015. **222**: p. 92-103.
78. Chang, H., et al., *A critical review of membrane wettability in membrane distillation from the perspective of interfacial interactions*. *Environmental science & technology*, 2020. **55**(3): p. 1395-1418.
79. Butt, H., K. Graf, and M. Kappl, *Physics and Chemistry of Interfaces*, WILEYVCH GmbH & Co. KGaA: Weinheim, 2003.
80. Israelachvili, J.N., *Intermolecular and surface forces*. 2011: Academic press.
81. Cai, X., et al., *Quantification of interfacial interactions between a rough sludge floc and membrane surface in a membrane bioreactor*. *Journal of colloid and interface science*, 2017. **490**: p. 710-718.
82. Zhao, L., et al., *Influences of acid–base property of membrane on interfacial interactions related with membrane fouling in a membrane bioreactor based on thermodynamic assessment*. *Bioresource technology*, 2016. **214**: p. 355-362.

83. Tang, C.Y., T. Chong, and A.G. Fane, *Colloidal interactions and fouling of NF and RO membranes: a review*. Advances in colloid and interface science, 2011. **164**(1-2): p. 126-143.
84. Parsons, D.F. and B.W. Ninham, *Surface charge reversal and hydration forces explained by ionic dispersion forces and surface hydration*. Colloids and Surfaces A: Physicochemical and Engineering Aspects, 2011. **383**(1-3): p. 2-9.
85. Grasso\*, D., et al., *A review of non-DLVO interactions in environmental colloidal systems*. Reviews in Environmental Science and Biotechnology, 2002. **1**: p. 17-38.
86. Thormann, E., *Surface forces between rough and topographically structured interfaces*. Current Opinion in Colloid and Interface Science, 2016. **26**: p. 9-16.
87. Ben-Naim, A.Y., *Hydrophobic interactions*. 2012: Springer Science & Business Media.
88. Blokzijl, W. and J.B. Engberts, *Hydrophobic effects. Opinions and facts*. Angewandte Chemie International Edition in English, 1993. **32**(11): p. 1545-1579.
89. Ducker, W.A. and D. Mastropietro, *Forces between extended hydrophobic solids: Is there a long-range hydrophobic force?* Current opinion in colloid & interface science, 2016. **22**: p. 51-58.
90. Kronberg, B., *The hydrophobic effect*. Current Opinion in Colloid & Interface Science, 2016. **22**: p. 14-22.
91. Meyer, E.E., K.J. Rosenberg, and J. Israelachvili, *Recent progress in understanding hydrophobic interactions*. Proceedings of the National Academy of Sciences, 2006. **103**(43): p. 15739-15746.
92. Southall, N.T., K.A. Dill, and A. Haymet, *A view of the hydrophobic effect*. 2002, ACS Publications. p. 521-533.
93. Ninham, B.W., T.T. Duignan, and D.F. Parsons, *Approaches to hydration, old and new: Insights through Hofmeister effects*. Current opinion in colloid & interface science, 2011. **16**(6): p. 612-617.
94. Lin, W. and J. Klein, *Control of surface forces through hydrated boundary layers*. Current opinion in colloid & interface science, 2019. **44**: p. 94-106.
95. Govinna, N., et al., *Electrospun fiber membranes from blends of poly(vinylidene fluoride) with fouling-resistant zwitterionic copolymers*. Polymer International, 2019. **68**(2): p. 231-239.
96. Kamaz, M., et al., *Surface modification of PVDF membranes for treating produced waters by direct contact membrane distillation*. International Journal of Environmental Research and Public Health, 2019. **16**(5).
97. Li, C., et al., *Antiwetting and Antifouling Janus Membrane for Desalination of Saline Oily Wastewater by Membrane Distillation*. ACS Applied Materials and Interfaces, 2019. **11**(20): p. 18456-18465.
98. Liu, C., C. Xiao, and Y. Huang, *Novel polyion complex films from chitosan and quarternized poly(4-vinyl-N-carboxymethylpyridine) containing zwitterion structure units*. Journal of Applied Polymer Science, 2007. **106**(5): p. 3070-3076.
99. Ozcan, S., et al., *Hydrophobic Antifouling Electrospun Mats from Zwitterionic Amphiphilic Copolymers*. ACS Applied Materials and Interfaces, 2018. **10**(21): p. 18300-18309.
100. Wang, J., et al., *3-[[3-(Triethoxysilyl)-propyl] amino] propane-1-sulfonic acid zwitterion grafted polyvinylidene fluoride antifouling membranes for*

- concentrating greywater in direct contact membrane distillation*. Desalination, 2019. **455**: p. 71-78.
101. Van Oss, C., *Acid–base interfacial interactions in aqueous media*. Colloids and Surfaces A: Physicochemical and Engineering Aspects, 1993. **78**: p. 1-49.
102. Ninham, B.W., *On progress in forces since the DLVO theory*. Advances in colloid and interface science, 1999. **83**(1-3): p. 1-17.
103. Hong, H., et al., *Membrane fouling in a membrane bioreactor: a novel method for membrane surface morphology construction and its application in interaction energy assessment*. Journal of Membrane Science, 2016. **516**: p. 135-143.
104. Lei, Q., et al., *Tuning anti-adhesion ability of membrane for a membrane bioreactor by thermodynamic analysis*. Bioresource Technology, 2016. **216**: p. 691-698.
105. Li, R., et al., *Effects of surface morphology on alginate adhesion: molecular insights into membrane fouling based on XDLVO and DFT analysis*. Chemosphere, 2019. **233**: p. 373-380.
106. Teng, J., et al., *Novel insights into membrane fouling in a membrane bioreactor: Elucidating interfacial interactions with real membrane surface*. Chemosphere, 2018. **210**: p. 769-778.
107. Zhao, L., et al., *Novel indicators for thermodynamic prediction of interfacial interactions related with adhesive fouling in a membrane bioreactor*. Journal of colloid and interface science, 2017. **487**: p. 320-329.
108. Feng, B., et al., *AFM measurements of Hofmeister effects on clay mineral particle interaction forces*. Applied Clay Science, 2020. **186**.
109. Gregory, K.P., et al., *Understanding specific ion effects and the Hofmeister series*. Physical Chemistry Chemical Physics, 2022. **24**(21): p. 12682-12718.
110. Jungwirth, P. and D.J. Tobias, *Specific ion effects at the air/water interface*. Chemical reviews, 2006. **106**(4): p. 1259-1281.
111. Kunz, W., *Specific ion effects in colloidal and biological systems*. Current Opinion in Colloid & Interface Science, 2010. **15**(1-2): p. 34-39.
112. Marcus, Y., *Effect of ions on the structure of water: structure making and breaking*. Chemical reviews, 2009. **109**(3): p. 1346-1370.
113. Parmar, A.S. and M. Muschol, *Hydration and hydrodynamic interactions of lysozyme: effects of chaotropic versus kosmotropic ions*. Biophysical journal, 2009. **97**(2): p. 590-598.
114. Russo, D., *The impact of kosmotropes and chaotropes on bulk and hydration shell water dynamics in a model peptide solution*. Chemical Physics, 2008. **345**(2-3): p. 200-211.
115. Salis, A. and B.W. Ninham, *Models and mechanisms of Hofmeister effects in electrolyte solutions, and colloid and protein systems revisited*. Chemical Society Reviews, 2014. **43**(21): p. 7358-7377.
116. Adamczyk, Z. and P. Weroński, *Application of the DLVO theory for particle deposition problems*. Advances in colloid and interface science, 1999. **83**(1-3): p. 137-226.
117. Henry, C., J.-P. Minier, and G. Lefèvre, *Towards a description of particulate fouling: From single particle deposition to clogging*. Advances in colloid and interface science, 2012. **185**: p. 34-76.
118. Ahmed, F.E., B.S. Lalia, and R. Hashaiekh, *A review on electrospinning for membrane fabrication: challenges and applications*. Desalination, 2015. **356**: p. 15-30.

119. Liao, Y., et al., *Progress in electrospun polymeric nanofibrous membranes for water treatment: Fabrication, modification and applications*. Progress in Polymer Science, 2018. **77**: p. 69-94.
120. Liao, Y., R. Wang, and A.G. Fane, *Engineering superhydrophobic surface on poly (vinylidene fluoride) nanofiber membranes for direct contact membrane distillation*. Journal of membrane science, 2013. **440**: p. 77-87.
121. Liao, Y., R. Wang, and A.G. Fane, *Fabrication of bioinspired composite nanofiber membranes with robust superhydrophobicity for direct contact membrane distillation*. Environmental science & technology, 2014. **48**(11): p. 6335-6341.
122. Martines, E., et al., *DLVO interaction energy between a sphere and a nano-patterned plate*. Colloids and Surfaces A: Physicochemical and Engineering Aspects, 2008. **318**(1-3): p. 45-52.
123. Henry, C., et al., *Numerical study on the deposition rate of hematite particle on polypropylene walls: Role of surface roughness*. Langmuir, 2011. **27**(8): p. 4603-4612.
124. Duffadar, R.D. and J.M. Davis, *Interaction of micrometer-scale particles with nanotextured surfaces in shear flow*. Journal of Colloid and Interface Science, 2007. **308**(1): p. 20-29.
125. Hoek, E.M.V., S. Bhattacharjee, and M. Elimelech, *Effect of membrane surface roughness on colloid-membrane DLVO interactions*. Langmuir, 2003. **19**(11): p. 4836-4847.
126. Shen, C., et al., *Theoretical and experimental investigation of detachment of colloids from rough collector surfaces*. Colloids and Surfaces A: Physicochemical and Engineering Aspects, 2012. **410**: p. 98-110.
127. Kemps, J.A.L. and S. Bhattacharjee, *Interactions between a solid spherical particle and a chemically heterogeneous planar substrate*. Langmuir, 2005. **21**(25): p. 11710-11721.
128. Wang, H., et al., *Interactions between nanoparticles and fractal surfaces*. Water Research, 2019. **151**: p. 296-309.
129. Shen, C., et al., *Application of DLVO energy map to evaluate interactions between spherical colloids and rough surfaces*. Langmuir, 2012. **28**(41): p. 14681-14692.
130. Liu, L., et al., *Understanding the fouling/scaling resistance of superhydrophobic/omniphobic membranes in membrane distillation*. Desalination, 2021. **499**: p. 114864.
131. Chew, N.G.P., S. Zhao, and R. Wang, *Recent advances in membrane development for treating surfactant- and oil-containing feed streams via membrane distillation*. Advances in Colloid and Interface Science, 2019. **273**.
132. Feng, S., et al., *Effects of fractal roughness of membrane surfaces on interfacial interactions associated with membrane fouling in a membrane bioreactor*. Bioresource technology, 2017. **244**: p. 560-568.
133. Jin, C., et al., *Non-linear, non-monotonic effect of nano-scale roughness on particle deposition in absence of an energy barrier: Experiments and modeling*. Scientific Reports, 2015. **5**.
134. Kemps, J.A. and S. Bhattacharjee, *Particle tracking model for colloid transport near planar surfaces covered with spherical asperities*. Langmuir, 2009. **25**(12): p. 6887-6897.



135. Raveendran, P. and A. Amirtharajah, *Role of short-range forces in particle detachment during filter backwashing*. Journal of environmental engineering, 1995. **121**(12): p. 860-868.
136. Shen, C., et al., *Coupled factors influencing detachment of nano- and micro-sized particles from primary minima*. Journal of Contaminant Hydrology, 2012. **134-135**: p. 1-11.
137. Li, H.N., J. Yang, and Z.K. Xu, *Asymmetric surface engineering for Janus membranes*. Advanced Materials Interfaces, 2020. **7**(7): p. 1902064.
138. Santore, M.M. and N. Kozlova, *Micrometer scale adhesion on nanometer-scale patchy surfaces: adhesion rates, adhesion thresholds, and curvature-based selectivity*. Langmuir, 2007. **23**(9): p. 4782-4791.
139. Kozlova, N. and M.M. Santore, *Manipulation of micrometer-scale adhesion by tuning nanometer-scale surface features*. Langmuir, 2006. **22**(3): p. 1135-1142.
140. Elimelech, M., J.Y. Chen, and Z.A. Kuznar, *Particle deposition onto solid surfaces with micropatterned charge heterogeneity: The “hydrodynamic bump” effect*. Langmuir, 2003. **19**(17): p. 6594-6597.
141. Nazemifard, N., J.H. Masliyah, and S. Bhattacharjee, *Particle deposition onto charge heterogeneous surfaces: convection– diffusion– migration model*. Langmuir, 2006. **22**(24): p. 9879-9893.
142. Kalasin, S. and M. Santore, *Hydrodynamic crossover in dynamic microparticle adhesion on surfaces of controlled nanoscale heterogeneity*. Langmuir, 2008. **24**(9): p. 4435-4438.
143. Rizwan, T. and S. Bhattacharjee, *Particle deposition onto charge-heterogeneous substrates*. Langmuir, 2009. **25**(9): p. 4907-4918.
144. Duffadar, R.D. and J.M. Davis, *Dynamic adhesion behavior of micrometer-scale particles flowing over patchy surfaces with nanoscale electrostatic heterogeneity*. Journal of Colloid and Interface Science, 2008. **326**(1): p. 18-27.
145. Bendersky, M. and J.M. Davis, *DLVO interaction of colloidal particles with topographically and chemically heterogeneous surfaces*. Journal of Colloid and Interface Science, 2011. **353**(1): p. 87-97.
146. Bendersky, M., M.M. Santore, and J.M. Davis, *Statistically-based DLVO approach to the dynamic interaction of colloidal microparticles with topographically and chemically heterogeneous collectors*. Journal of Colloid and Interface Science, 2015. **449**: p. 443-451.
147. Hejazi, V. and M. Nosonovsky, *Wetting transitions in two-, three-, and four-phase systems*. Langmuir, 2012. **28**(4): p. 2173-2180.
148. Jung, Y.C. and B. Bhushan, *Wetting behavior of water and oil droplets in three-phase interfaces for hydrophobicity/philicity and oleophobicity/philicity*. Langmuir, 2009. **25**(24): p. 14165-14173.
149. Nosonovsky, M. and B. Bhushan, *Why re-entrant surface topography is needed for robust oleophobicity*. Philosophical Transactions of the Royal Society A: Mathematical, Physical and Engineering Sciences, 2016. **374**(2073): p. 20160185.
150. Dunderdale, G.J., C. Urata, and A. Hozumi, *An underwater superoleophobic surface that can be activated/deactivated via external triggers*. Langmuir, 2014. **30**(44): p. 13438-13446.
151. Currie, E., et al., *Polyacrylic acid brushes: surface pressure and salt-induced swelling*. Langmuir, 2000. **16**(22): p. 8324-8333.
152. Kobayashi, M., et al., *Wettability and antifouling behavior on the surfaces of superhydrophilic polymer brushes*. Langmuir, 2012. **28**(18): p. 7212-7222.

153. Tan, K.Y., et al., *Nonfouling capture–release substrates based on polymer brushes for separation of water-dispersed oil droplets*. ACS Applied Materials & Interfaces, 2012. **4**(12): p. 6403-6409.
154. Daniel, D., et al., *Origin of Underwater Oil-Repellence in Polyelectrolyte Brush Surfaces*. Advanced Materials Interfaces, 2021. **8**(2): p. 2001203.
155. Gajda, M. and M. Ulbricht, *Capillary pore membranes with grafted diblock copolymers showing reversibly changing ultrafiltration properties with independent response to ions and temperature*. Journal of Membrane Science, 2016. **514**: p. 510-517.
156. Louder, S.J., et al., *Fouling-resistant membranes with tunable pore size fabricated using cross-linkable copolymers with high zwitterion content*. Journal of Membrane Science Letters, 2022. **2**(1): p. 100019.
157. Ding, J., et al., *Surface modification of nanofiltration membranes with zwitterions to enhance antifouling properties during brackish water treatment: A new concept of a “buffer layer”*. Journal of Membrane Science, 2021. **637**: p. 119651.
158. Zhang, X., et al., *Surface functionalization of TFC FO membranes with zwitterionic polymers: Improvement of antifouling and salt-responsive cleaning properties*. Journal of Membrane Science, 2017. **544**: p. 368-377.
159. Ran, J., et al., *Atom transfer radical polymerization (ATRP): A versatile and forceful tool for functional membranes*. Progress in Polymer Science, 2014. **39**(1): p. 124-144.
160. Xu, X., et al., *Structure and functionality of polyelectrolyte brushes: a surface force perspective*. Chemistry–An Asian Journal, 2018. **13**(22): p. 3411-3436.
161. Olivier, A., et al., *Surface-initiated controlled polymerization as a convenient method for designing functional polymer brushes: From self-assembled monolayers to patterned surfaces*. Progress in polymer science, 2012. **37**(1): p. 157-181.
162. Kang, H., W. Jeong, and D. Hong, *Antifouling surface coating using droplet-based SI-ARGET ATRP of carboxybetaine under open-air conditions*. Langmuir, 2019. **35**(24): p. 7744-7750.
163. Yan, J., et al., *Ultraviolet light-induced surface-initiated atom-transfer radical polymerization*. ACS Macro Letters, 2013. **2**(7): p. 592-596.
164. Bauer, A., et al., *In-situ monitoring and quantification of fouling development in membrane distillation by means of optical coherence tomography*. Journal of membrane science, 2019. **577**: p. 145-152.
165. Fortunato, L., et al., *Fouling development in direct contact membrane distillation: Non-invasive monitoring and destructive analysis*. Water research, 2018. **132**: p. 34-41.
166. Guo, J., et al., *Fouling behavior of negatively charged PVDF membrane in membrane distillation for removal of antibiotics from wastewater*. Journal of membrane science, 2018. **551**: p. 12-19.
167. Shao, S., et al., *Unraveling the kinetics and mechanism of surfactant-induced wetting in membrane distillation: an in situ observation with optical coherence tomography*. Environmental Science & Technology, 2021. **56**(1): p. 556-563.
168. Cen, J., et al., *Fouling of reverse osmosis membranes by cane molasses fermentation wastewater: detection by electrical impedance spectroscopy techniques*. Desalination and Water Treatment, 2013. **51**(4-6): p. 969-975.
169. Cen, J., et al., *Real time fouling monitoring with Electrical Impedance Spectroscopy*. Journal of Membrane Science, 2015. **484**: p. 133-139.

170. Chilcott, T., et al. *In situ characterization of fouling in reverse osmosis membranes using electrical impedance spectroscopy*. in *Journal of Physics: Conference Series*. 2013. IOP Publishing.
171. Chilcott, T.C., *Origin of resonant electrical impedances in membranes induced by osmosis: Analytical solutions of the AC Nernst–Planck, Poisson and continuity equations as functions of water velocity*. *Journal of membrane science*, 2013. **438**: p. 65-76.
172. Chilcott, T.C., A. Antony, and G. Leslie, *In situ electrical impedance characterization of fouling by calcium agents in reverse osmosis membrane systems using Maxwell Wagner and hydrodynamic models*. *Desalination*, 2017. **403**: p. 64-79.
173. Detrich, K.T. and N.C. Goulbourne. *Sensor development for in situ detection of concentration polarization and fouling of reverse osmosis membranes*. in *Sensors and Smart Structures Technologies for Civil, Mechanical, and Aerospace Systems 2009*. 2009. SPIE.
174. Drazevic, E., et al., *Enhanced partitioning and transport of phenolic micropollutants within polyamide composite membranes*. *Environmental science & technology*, 2012. **46**(6): p. 3377-3383.
175. Ho, J.S., et al., *In-situ monitoring of biofouling on reverse osmosis membranes: Detection and mechanistic study using electrical impedance spectroscopy*. *Journal of Membrane Science*, 2016. **518**: p. 229-242.
176. Ho, J.S., et al., *A threshold flux phenomenon for colloidal fouling in reverse osmosis characterized by transmembrane pressure and electrical impedance spectroscopy*. *Journal of Membrane Science*, 2016. **500**: p. 55-65.
177. Ho, J.S., et al., *Monitoring fouling behavior of reverse osmosis membranes using electrical impedance spectroscopy: A field trial study*. *Desalination*, 2017. **407**: p. 75-84.
178. Hu, Z., et al., *Real-time monitoring of scale formation in reverse osmosis using electrical impedance spectroscopy*. *Journal of membrane science*, 2014. **453**: p. 320-327.
179. Kavanagh, J., et al., *Fouling of reverse osmosis membranes using electrical impedance spectroscopy: measurements and simulations*. *Desalination*, 2009. **236**(1-3): p. 187-193.
180. Li, Y., et al., *Integration of an anaerobic fluidized-bed membrane bioreactor (MBR) with zeolite adsorption and reverse osmosis (RO) for municipal wastewater reclamation: comparison with an anoxic-aerobic MBR coupled with RO*. *Chemosphere*, 2020. **245**: p. 125569.
181. Sim, L., et al., *Detection of reverse osmosis membrane fouling with silica, bovine serum albumin and their mixture using in-situ electrical impedance spectroscopy*. *Journal of membrane science*, 2013. **443**: p. 45-53.
182. Sim, L.N., et al., *Quantitative determination of the electrical properties of RO membranes during fouling and cleaning processes using electrical impedance spectroscopy*. *Desalination*, 2016. **379**: p. 126-136.
183. Hao, W., et al., *Dielectric measurements of fouling of nanofiltration membranes by sparingly soluble salts*. *Journal of Membrane Science*, 2016. **497**: p. 339-347.
184. Montalvillo, M., et al., *Charge and dielectric characterization of nanofiltration membranes by impedance spectroscopy*. *Journal of Membrane Science*, 2014. **454**: p. 163-173.

185. Romero, V., et al., *Changes in morphology and ionic transport induced by ALD SiO<sub>2</sub> coating of nanoporous alumina membranes*. ACS Applied Materials & Interfaces, 2013. **5**(9): p. 3556-3564.
186. Xu, Y., et al., *Electrochemical impedance spectroscopy analysis of sulfonated polyethersulfone nanofiltration membrane*. Desalination, 2011. **271**(1-3): p. 29-33.
187. Bannwarth, S., et al., *Characterization of hollow fiber membranes by impedance spectroscopy*. Journal of membrane science, 2015. **473**: p. 318-326.
188. Bannwarth, S., et al., *On-line monitoring of cake layer structure during fouling on porous membranes by in situ electrical impedance analysis*. Journal of Membrane Science, 2016. **503**: p. 188-198.
189. Chilcott, T., et al., *Electrical impedance spectroscopy characterisation of conducting membranes: I. Theory*. Journal of Membrane Science, 2002. **195**(2): p. 153-167.
190. DuToit, M., E. Ngaboyamahina, and M. Wiesner, *Pairing electrochemical impedance spectroscopy with conducting membranes for the in situ characterization of membrane fouling*. Journal of Membrane Science, 2021. **618**: p. 118680.
191. Gaedt, L., et al., *Electrical impedance spectroscopy characterisation of conducting membranes: II. Experimental*. Journal of Membrane Science, 2002. **195**(2): p. 169-180.
192. Gao, F., et al., *Role of ionic strength on protein fouling during ultrafiltration by synchronized UV-vis spectroscopy and electrochemical impedance spectroscopy*. Journal of Membrane Science, 2018. **563**: p. 592-601.
193. Genceli, E.A., et al., *Effects of carboxylated multi-walled carbon nanotubes having different outer diameters on hollow fiber ultrafiltration membrane fabrication and characterization by electrochemical impedance spectroscopy*. Polymer Bulletin, 2018. **75**: p. 2431-2457.
194. Jing, Y. and B.P. Chaplin, *Electrochemical impedance spectroscopy study of membrane fouling characterization at a conductive sub-stoichiometric TiO<sub>2</sub> reactive electrochemical membrane: Transmission line model development*. Journal of Membrane Science, 2016. **511**: p. 238-249.
195. Palencia, M., et al., *Polyelectrolyte adsorption study on polyethersulfone membrane during polymer-enhanced ultrafiltration by electrochemical impedance spectroscopy*. Polymer bulletin, 2010. **65**: p. 145-156.
196. Tang, J., et al., *Characterizing synergistic effect of coagulant aid and membrane fouling during coagulation-ultrafiltration via in-situ Raman spectroscopy and electrochemical impedance spectroscopy*. Water Research, 2020. **172**: p. 115477.
197. Tian, J., et al., *In-situ monitoring of oil emulsion fouling in ultrafiltration via electrical impedance spectroscopy (EIS): Influence of surfactant*. Journal of Membrane Science, 2020. **616**: p. 118527.
198. Yang, Y., et al., *Novel functionalized nano-TiO<sub>2</sub> loading electrocatalytic membrane for oily wastewater treatment*. Environmental science & technology, 2012. **46**(12): p. 6815-6821.
199. Zhang, N., M.A. Halali, and C.-F. de Lannoy, *Detection of fouling on electrically conductive membranes by electrical impedance spectroscopy*. Separation and Purification Technology, 2020. **242**: p. 116823.

200. Cristian, P., et al., *Removal of zinc ions from model wastewater system using bicopolymer membranes with fumed silica*. Journal of Water Process Engineering, 2015. **8**: p. 1-10.
201. Li, Y., et al., *Anion exchange nanocomposite membranes modified with graphene oxide and polydopamine: interfacial structure and antifouling applications*. ACS Applied Nano Materials, 2020. **3**(1): p. 588-596.
202. Park, J.-S., et al., *Characterization of BSA-fouling of ion-exchange membrane systems using a subtraction technique for lumped data*. Journal of Membrane Science, 2005. **246**(2): p. 137-144.
203. Park, J.-S., et al., *An approach to fouling characterization of an ion-exchange membrane using current–voltage relation and electrical impedance spectroscopy*. Journal of Colloid and Interface Science, 2006. **294**(1): p. 129-138.
204. Zhang, L., et al., *Characterization of fouling and concentration polarization in ion exchange membrane by in-situ electrochemical impedance spectroscopy*. Journal of Membrane Science, 2020. **594**: p. 117443.
205. Zhao, Z., et al., *Electrochemical impedance spectroscopy and surface properties characterization of anion exchange membrane fouled by sodium dodecyl sulfate*. Journal of Membrane Science, 2017. **530**: p. 220-231.
206. Zhao, Z., et al., *Property characterization and mechanism analysis on organic fouling of structurally different anion exchange membranes in electrodialysis*. Desalination, 2018. **428**: p. 199-206.
207. Mohammadi Ghaleni, M., et al., *Fabrication of Janus membranes for desalination of oil-contaminated saline water*. ACS applied materials & interfaces, 2018. **10**(51): p. 44871-44879.
208. Fan, D., et al., *Self-healing and tough GO-supported hydrogels prepared via surface-initiated ATRP and photocatalytic modification*. New Journal of Chemistry, 2019. **43**(7): p. 3099-3110.
209. Audouin, F., et al., *Protein immobilization onto poly (acrylic acid) functional macroporous polyHIPE obtained by surface-initiated ARGET ATRP*. Biomacromolecules, 2012. **13**(11): p. 3787-3794.
210. Çelebi, B., et al., *A new stationary phase for hydrophilic interaction chromatography: polyacrylate-based hydrophilic, monosized-porous beads with zwitterionic molecular brushes*. Chromatographia, 2014. **77**(21-22): p. 1511-1520.
211. Alvarez-Gayosso, C., et al., *Preparation and microstructure of cobalt (III) poly (acrylate) hybrid materials*. Int. J. Basic Appl. Sci, 2015. **4**: p. 255-263.
212. Clochard, M.-C., et al., *Tailoring bulk and surface grafting of poly (acrylic acid) in electron-irradiated PVDF*. Polymer, 2004. **45**(26): p. 8683-8694.
213. Song, L., C. Dong, and J. Li, *Application of the PAA-PVDF microfiltration composite membrane for municipal wastewater advanced treatment*. Toxicological & Environmental Chemistry, 2007. **89**(2): p. 223-232.
214. Lego, B., W. Skene, and S. Giasson, *Swelling study of responsive polyelectrolyte brushes grafted from mica substrates: effect of pH, salt, and grafting density*. Macromolecules, 2010. **43**(9): p. 4384-4393.
215. Borozenko, O., et al., *Organophosphonic acids as viable linkers for the covalent attachment of polyelectrolyte brushes on silica and mica surfaces*. Polymer Chemistry, 2014. **5**(19): p. 5740-5750.
216. Asenath Smith, E. and W. Chen, *How to prevent the loss of surface functionality derived from aminosilanes*. Langmuir, 2008. **24**(21): p. 12405-12409.

217. Borozenko, O., W. Skene, and S. Giasson. *Direct Polymerization of Polyacrylic Acid on Mica Substrates using ATRP—A Preliminary Study*. in *Macromolecular Symposia*. 2010. Wiley Online Library.
218. Wassilkowska, A., et al., *An analysis of the elemental composition of micro-samples using EDS technique*. *Czasopismo Techniczne*, 2014. **2014**(Chemia Zeszyt 1-Ch (18) 2014): p. 133-148.
219. Drechsler, A., et al., *Interaction forces between micro-sized silica particles and weak polyelectrolyte brushes at varying pH and salt concentration*. *Langmuir*, 2010. **26**(9): p. 6400-6410.
220. Dunlop, I.E., et al., *Structure and collapse of a surface-grown strong polyelectrolyte brush on sapphire*. *Langmuir*, 2012. **28**(6): p. 3187-3193.
221. Jin, H., et al., *Experimental study of the salinity-specific adhesion force between oil drop and underwater superoleophobic polyelectrolyte surfaces*. *ACS Applied Polymer Materials*, 2019. **1**(10): p. 2582-2589.
222. Cheng, Y., et al., *Zwitterionic Polymer-Grafted Superhydrophilic and Superoleophobic Silk Fabrics for Anti-Oil Applications*. *Macromolecular Rapid Communications*, 2020. **41**(21): p. 2000162.
223. Liao, M., G. Cheng, and J. Zhou, *Underwater superoleophobicity of pseudozwitterionic SAMs: effects of chain length and ionic strength*. *The Journal of Physical Chemistry C*, 2017. **121**(32): p. 17390-17401.
224. Yang, J., et al., *Salt-responsive zwitterionic polymer brushes with tunable friction and antifouling properties*. *Langmuir*, 2015. **31**(33): p. 9125-9133.
225. Milne, A. and A. Amirfazli, *The Cassie equation: How it is meant to be used*. *Advances in colloid and interface science*, 2012. **170**(1-2): p. 48-55.
226. Chiao, Y.-H., et al., *High-performance polyacrylic acid-grafted PVDF nanofiltration membrane with good antifouling property for the textile industry*. *Polymers*, 2020. **12**(11): p. 2443.
227. Zhang, R., et al., *The Tethered fibrillar hydrogels brushes for underwater antifouling*. *Advanced Materials Interfaces*, 2017. **4**(7): p. 1601039.
228. Darmanin, T. and F. Guittard, *Superhydrophobic and superoleophobic properties in nature*. *Materials today*, 2015. **18**(5): p. 273-285.
229. Azzaroni, O. and C. Gervasi, *Characterization of responsive polymer brushes at solid/liquid interfaces by electrochemical impedance spectroscopy*. *Functional Polymer Films: 2 Volume Set*, 2011: p. 809-830.
230. Lazanas, A.C. and M.I. Prodromidis, *Electrochemical Impedance Spectroscopy— A Tutorial*. *ACS Measurement Science Au*, 2023.
231. Amaya-Vías, D., et al., *Diffusion behavior of humic acid during desalination with air gap and water gap membrane distillation*. *Water research*, 2019. **158**: p. 182-192.
232. Muster-Slawitsch, B., et al., *Membrane distillation for concentration of protein-rich waste water from meat processing*. *Journal of Water Process Engineering*, 2021. **44**: p. 102285.
233. Guan, Z. and B. Smart, *A remarkable visible light effect on atom-transfer radical polymerization*. *Macromolecules*, 2000. **33**(18): p. 6904-6906.
234. Yang, Q., J. Lalevée, and J. Poly, *Development of a robust photocatalyzed ATRP mechanism exhibiting good tolerance to oxygen and inhibitors*. *Macromolecules*, 2016. **49**(20): p. 7653-7666.
235. Zhang, T., et al., *ATRP with a light switch: photoinduced ATRP using a household fluorescent lamp*. *Polymer Chemistry*, 2014. **5**(16): p. 4790-4796.

